UNIVERSITÁ DEGLI STUDI DI PAVIA

Dottorato in Scienze Chimiche e Farmaceutiche e
dell'Innovazione Industriale
(XXXV ciclo)

Coordinatore: Chiar.mo Prof. Giorgio Colombo

Development of Semiconducting Materials for Photoelectrochemical Cells

Tesi di Dottorato di:
Lidia Romani

Tutor: Prof. Lorenzo Malavasi

Co-Tutor: Dr. Maurizio Notaro (RSE S.p.A.)

ANNO ACCADEMICO 2021 - 2022

Contents

Abstract

Photochemistry is a branch of chemistry that has been developed ever since the 19th century, which exploits light instead of heat as a source of energy to initiate some reactions in milder conditions. As a part of photochemistry, photocatalysis has also been discovered at the beginning of the 20th century, however it did not receive much attention up till the 70s, after the discovery of the versatility of titanium dioxide and with the stimulus of a difficult economic situation, that first posed the problem of a future scarcity of oil. From then on, an increasing attention was placed on the field, with the number of yearly published papers that grew exponentially.

As a development of photochemistry, when a heterogeneous photocatalyst is paired with an electrochemical apparatus the practice of photo-electrocatalysis arises. Compared with simple photocatalysis, this approach offers the advantage of separating the reduction and oxidation sites preventing the issues of product crossover. The photo-electrocatalytic approach is quite versatile and is mainly applied in the fields of organic synthesis, pollutants degradation, carbon dioxide reduction and water splitting.

Photogenerated hydrogen is among the most promising green energy carriers; the most common technology for this aim couples a photovoltaic cell and an electrolyzer in order to carry out water electrolysis, however there are also other kinds of photogeneration methods. Among the other production approaches, there is the one of the photonic systems, that employ two photoelectrodes that act both as light absorbers and as catalysts; these systems are less efficient, compared with other photogeneration methods, however they are also more environmentally friendly, that is their main merit.

The main component of these photonic systems are the photoelec-

trodes, that can be made of many different materials; in literature, the constituents of the photoanodes are mainly metallic oxides, chalcogenides or halogens, while for the photocathodes they are titanium dioxide, metal chalcogenides or carbon nitride.

In this work we investigated the potentials of a new kind of photocatalysts for hydrogen evolution in aqueous environment; these are heterogeneous materials, composed by carbon nitride and metal halide perovskites and/or perovskite derivatives, the main characteristics of which are the possibility of including most of the elements of the periodic table and also many organic cations in their composition, and the ability of tuning their optical and electronical properties with the variation of their exact composition.

In particular, the project was divided in three parts: during the first period, the materials employed for the hydrogen evolution catalysis were synthesised and characterized in their powder form starting from the pure components, continuing with the heterogeneous catalysts; during the second period, the building of the photo-electrodes was started, for the cathodic electrodes some of the previously characterized composite materials were employed, while for the anodic ones bismuth vanadate-based materials, widely described in literature, were briefly optimized; during the third period, two of the individually characterized electrodes were selected and used together to close some complete photo-electrochemical cells, that were also employed to investigate different kinds of electrolytes.

The characterization of the samples made use of different techniques, aimed at determining both their inherent properties and their behaviour in working conditions; specifically, the crystal structures and optical properties of the materials were determined through X-Ray Diffraction (XRD) and UV-Vis absorption spectroscopy; the water stability and hydrogen photo-production abilities of the powdered cathodic photo-catalysts were probed through, respectively, the examination of samples that were dispersed in water for a prolonged time and photocatalytic tests on the powdered catalysts dispersed in an aqueous solution; other kinds of characterizations were performed only on some samples, when they were deemed necessary. In addition, in order to widen the characterization of these materials, the powders were used to also catalyse some organic reactions and pollutant degradations.

On the other hand, for the photo-electrodes, the characterization mainly consisted in Open Circuit Voltage (OCV) readings, used to discover the potential naturally reached by the materials, Cyclic Voltammetry (CV), that showed the working potential of the materials, and Chronoamperometric (CRA) measures, that simulated the real working conditions.

Lastly, for the complete cells, not only the working conditions were simulated through CRA measures, but different electrolytes were also used in order to develop a basic understanding of what kind of environment could be more suitable for the materials.

Chapter 1

Introduction

The aim of this PhD work has been the development of semiconducting materials capable of catalysing redox reactions, with a particular focus on the water splitting reaction, that involves both the reduction and the oxidation of water, and the synthesis of molecular hydrogen and oxygen.

1.1 The Hydrogen Issue

Given the widely known issues of climatic change due to CO_2 emission, associated with the large consumption of conventional fossil fuels, research has been focusing on the development of innovative technologies able to produce large quantities of hydrogen to employ as ecologic fuel. This significant amount of "green hydrogen" must necessarily be produced by processes with low emissions of climate-altering gases, and through the use of energy from renewable sources.

For this reason, a method different from steam reforming, that is currently the most widespread process for hydrogen synthesis must be employed. Ideally, this new method could be represented by water electrolysis, which involves two semi-reactions:

$$\text{reduction:}\quad 2\ H^+_{(aq)} \ +\ 2\ e^- \xrightarrow{\qquad} H_{2(g)}$$

$$\text{oxidation:}\quad 2\ H_2O_{(liq)} \xrightarrow{\qquad} O_{2(g)} \ +\ 4\ H^+_{(aq)} \ +\ 4\ e^-$$

Both semi-reactions are catalysed by noble metals, but due to their high cost, their extensive and widespread use for large hydrogen productions would be very expensive.

Therefore, researchers are focused on the development of non-noble metal catalysts that provide a high production-yield.

The heterogeneous-photocatalysis process can be carried out in two ways:

suspension-photocatalysis, the catalyst is used in form of powder, directly suspended in water;

photo-electrocatalysis the catalyst is supported onto an electrode, immersed in a water-based electrolyte;

in particular, since suspension-photocatalysis only provides very low reaction yields, the main focus is set on photo-electrocatalytic systems.

The Reaction Mechanism

The same photocatalytic water splitting process can be carried out in various media, both acidic, neutral, or alkaline, however the reaction medium has an influence on the reaction mechanism.[1]

Hydrogen Evolution Semi-Reaction

The reduction semi-reaction takes place on the cathode surface, and it has been extensively characterized in the case of various transition metals photocatalysts.

This process is divided in two steps, as shown in Figure 1.1:

- at first, the hydrogen source is electrochemically adsorbed onto the electrode, through the *Volmer Reaction*

  in acidic media:

  $$H^+ + M + e^- \xrightarrow{\qquad} MH_{ads}$$

  in alkaline or neutral media:

  $$H_2O + M + e^- \xrightarrow{\qquad} MH_{ads} + OH^-$$

- afterwards, the hydrogen molecule is electrochemically desorbed, through the *Heyrovsky Reaction*

  in acidic media:

  $$MH_{ads} + H^+ + e^- \xrightarrow{\qquad} M + H_2$$

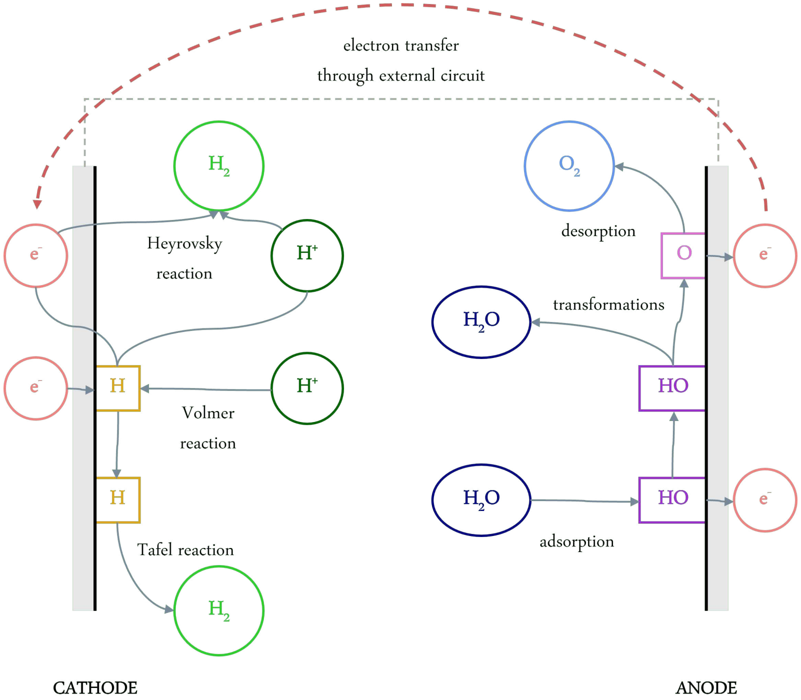

Figure 1.1. Schematic representation of the electrochemical water splitting reaction mechanism.

in alkaline or neutral media:

$$\mathrm{MH_{ads} + H_2O + e^- \longrightarrow M + OH^- + H_2}$$

however, if the concentration of adsorbed hydrogen is very high, the electrochemical desorption is replaced by a chemical desorption, through the *Tafel Reaction*

$$\mathrm{2\,MH_{ads} \longrightarrow 2\,M + H_2}$$

Oxygen Evolution Semi-Reaction

The oxidation semi-reaction takes place on the anode surface, and it was characterized in the case of various metal oxides. From these studies it emerged that the specific mechanism is strictly connected to the surface structure of the catalyst, however a generic mechanism has been identified (Figure 1.1), in which:

- at first, the oxygen source is electrochemically adsorbed onto the electrode

$$\mathrm{M + H_2O \longrightarrow MOH + H^+ + e^-}$$

- afterwards the adsorbed specie undergoes some transformations

$$\mathrm{MOH \longrightarrow MO + H^+ + e^-}$$
or
$$\mathrm{2\,MOH \longrightarrow MO + M + H_2O}$$

- and lastly the oxygen molecule is desorbed

$$\mathrm{MO + H_2O \longrightarrow M + 2\,H^+ + 2\,e^- + O_2}$$
or
$$\mathrm{2\,MO \longrightarrow 2\,M + O_2}$$

1.2 The Characteristics of a Photocatalyst

For the selection of the photocatalyst a few factors need to be taken into consideration:[2]

- it needs to absorb the solar radiation in the most efficiently possible way; therefore, it needs to absorb the visible light;
- its valence and conduction bands need to be properly aligned with the electrochemical potential of the reaction it has to catalyse (in the case of water splitting, the conduction band must be more negative than $0\,V$ and the valence band must be more positive than $1.23\,V$, referred to the *Normal Hydrogen Electrode*);
- it needs to provide a suitable reaction kinetics;
- it needs to be stable in aqueous solution, under intense illumination for a long period of time.

In addition to these basic characteristics, the factors that limit the efficiency of the process also need to be considered. These factors are mainly embodied by the recombination of the charge carriers, which is the process that competes with the reaction and is often much quicker than this. Therefore:

- it must provide efficient transport and transfer of the charge carriers.

Lastly, it needs to be noted that even though the thermodynamic potentials of the reduction and oxidation of water are respectively $0V$ and $-1.23V$, regardless of the reaction environment, due to kinetic hurdles, there is no electrochemical reaction that takes place at the expected voltage.

The kinetic restrictions can be of three kinds:

Activation Overpotential: it is an intrinsic characteristic of the material; it can only be decreased by employing a different catalyst.

Concentration Overpotential: it arises with the beginning of the reaction, due to the sudden drop of the concentration of the reactants near the electrode-solution interface. It can be decreased by stirring the reaction solution.

Ohmic Drop: it is connected to the internal resistances of the electrode and the electrolytic solution, and to the contact resistance of the electrode-solution interface.

For the reduction semi-reaction, the main contribution is the activation overpotential, while for the oxidation semi-reaction all the contributions are relevant.

There is no single material that meets all these requirements; however, it is possible to tune the materials' characteristics in order to optimize the width and the position of their energy gap so as to improve the charge transfer.

How Do Photoelectrodes Work

In principle, the photoelectrodes work because a thermodynamically favoured charge transfer is established between the electrode and the reactive species contained in the electrolytic solution. Then, a one-step catalysis may take place if the catalyst is a semiconducting material the energy gap of which contains the electrochemical potentials of both semi-reactions, of reduction and oxidation.[3]

However, materials that satisfy this condition tend to have very large energy gaps, that limit their light-harvesting efficiency.

The other option is the adoption of a two-step catalysis. In this case, two semiconductors are employed, the energy gaps of which only contain the reaction potential of one semi-reaction, they are connected in series and each semi-reaction takes place on the surface of the corresponding electrode.

To improve the photocatalytic performances of the materials, usually each photoelectrode is made of more than one material, in order to form heterojunctions that allow charge transfer between their components:[2]

Semiconductor-Semiconductor Junction: usually p and n semiconductors are used, because at the interface that separates the two materials an electric field is produced, and this allows the diffusion and separation of the charge carriers;

Semiconductor-Metal Junction: in this case the metal particles act as traps for the electrons photogenerated in the semiconductor;

Semiconductor-Carbon Junction: this case is very similar to the one that employs metallic particles, with the difference that an electronically conductive form of carbon is employed (such as carbon nanotubes or graphene);

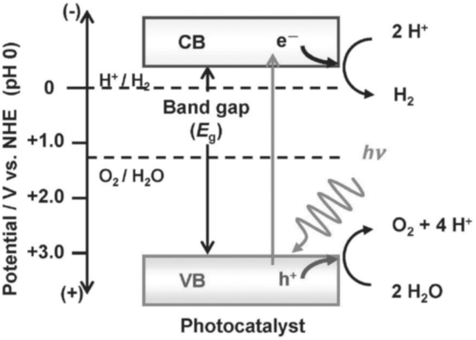

(a)

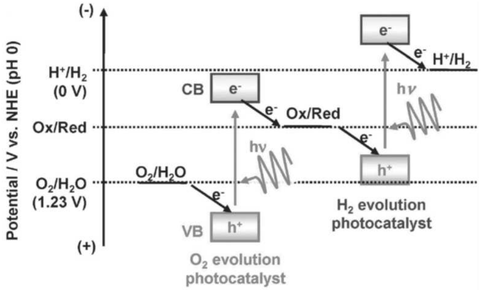

(b)

Figure 1.2. Energy diagrams of photocatalytic water splitting based on: a) one-step excitation, and b) two-step excitation. Reprinted with permission from ref.[3] Copyright 2014 Chemical Society Reviews.

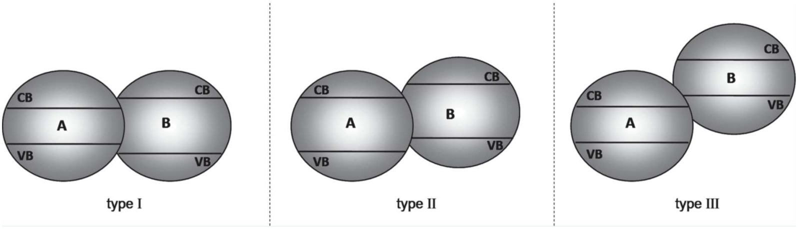

Figure 1.3. Different types of semiconductor heterojunctions. Reprinted with permission from ref.[4] Copyright 2014 Advanced Functional Materials.

Multicomponent Junction: in order to maximise the charge separation effect, various kinds of materials are combined, however in this case no general charge transfer mechanism can be provided.

When speaking about semiconductor-semiconductor junctions, three kinds of junctions can be made:[4]

Type I: in this case, the energy gap of one of the two materials is wider than the other and contains both its valence and conduction band edges. This means that both electrons and holes accumulate on the material with wider energy gap;

Type II: in this case, both the valence and conduction band edges of one of the materials are lower than those of the other. This means that charge transfer takes place between the two semiconductors (this is also the most widespread architecture);

Type III: in this case also, charge separation occurs, however the band positions of the two semiconductors are so far apart that such arrangement is also called a *broken-gap situation*.

These kinds of architectures are often conceived in order to associate materials with wide and narrow energy gaps, so as to increase the range of absorption of the solar spectrum, and they are also referred to as "Internal Biased Systems".[5]

Ideally, the optimal condition would be a system that works efficiently without any kind of external energy contribution, and this is a *Zero Bias System*.[5]

Since, as was already stated, there is no material capable of actually working in this way, *Biased Systems* are employed; in these cases, an additional voltage is provided in order to decrease the recombination of electrons and holes, and the additional voltage can be *External* or *Internal*:[5]

Electrical Bias: the additional voltage is given via a potentiometer, so it is essentially powered by the normal electrical grid;

Chemical Bias: in this case the reaction takes place in two separate half-cells that are constantly kept at two different values of pH, and the different electrolytes in which the electrodes are immersed provide the additional voltage.
However, the acids and bases need to be constantly fed to the reactor, because they are consumed;

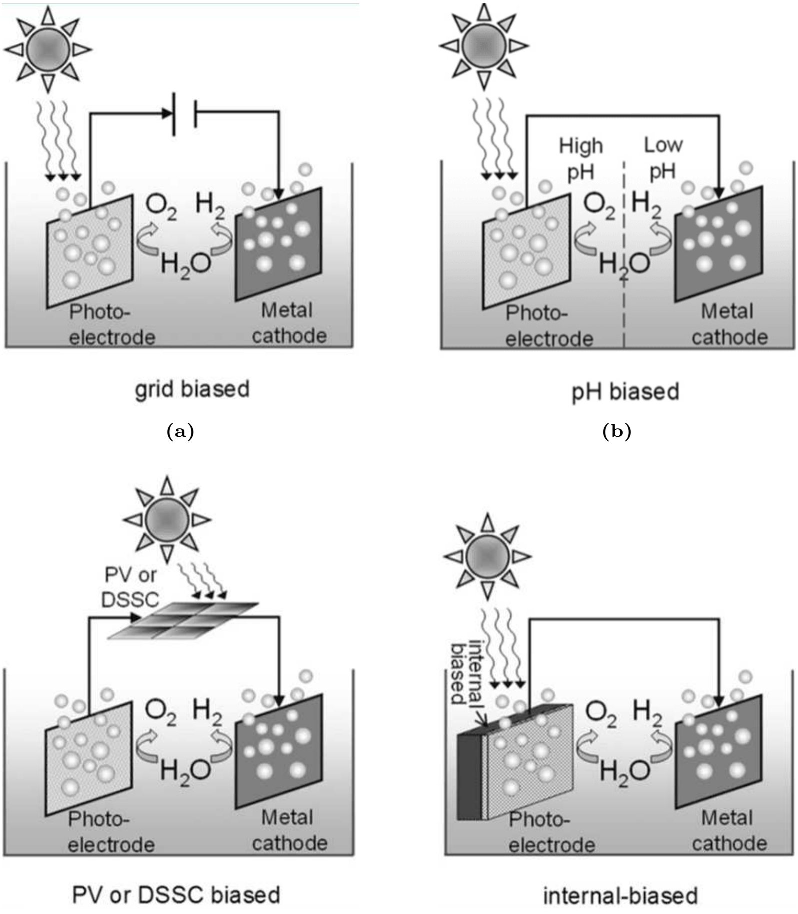

(a) (b) (c) (d)

Figure 1.4. The different methods of biasing for PEC water splitting. Reprinted with permission from ref.[5] Copyright 2010 International Journal of Hydrogen Energy.

Photovoltaic Bias: the concept is similar to the *electrical bias*, however in this case the additional voltage is provided by a photovoltaic cell directly connected to the photo-electrochemical cell;

Internal Bias: this is the case previously discussed, in which at least two semiconductors with narrow energy gaps are used to form heterojunctions, and the sum of their energy gaps needs to be sufficiently large to contain both the oxidation and reduction potentials.

When designing a photo-electrochemical system, one can also associate both an *internal bias* and an *external bias*; for example by using a *photovoltaic bias* one could move towards the development of green-energy-technologies.

1.3 State of the Art Photo-electrocatalytic Materials

Anodic Materials

The first materials that were employed for the photo-electrocatalysis of water splitting were binary oxides:

- the oxides of d^0 metals all have low energy valence bands, that make them particularly stable towards the oxidation half-reaction; however, they also have wide energy gaps that prevent an efficient light-absorption;[6]
- the oxides of d^n metals ($0 < n < 10$) have narrower energy gaps and good stability; however they are not efficient in the separation of the charge carriers, and provide only a brief lifetime of the separated electron-hole pair;[6]
- the oxides of d^{10} metals also show narrower energy gaps, however they have a problem of stability and cannot be employed without being covered by a protective layer, otherwise the auto-corrosion is favoured against water oxidation.[6]

The consequent step of experimentation naturally consisted in the study of mixed oxides, containing at least two metals, in the attempt to combine the qualities of the respective binary oxides.

Among the most popular mixed oxides:[6]

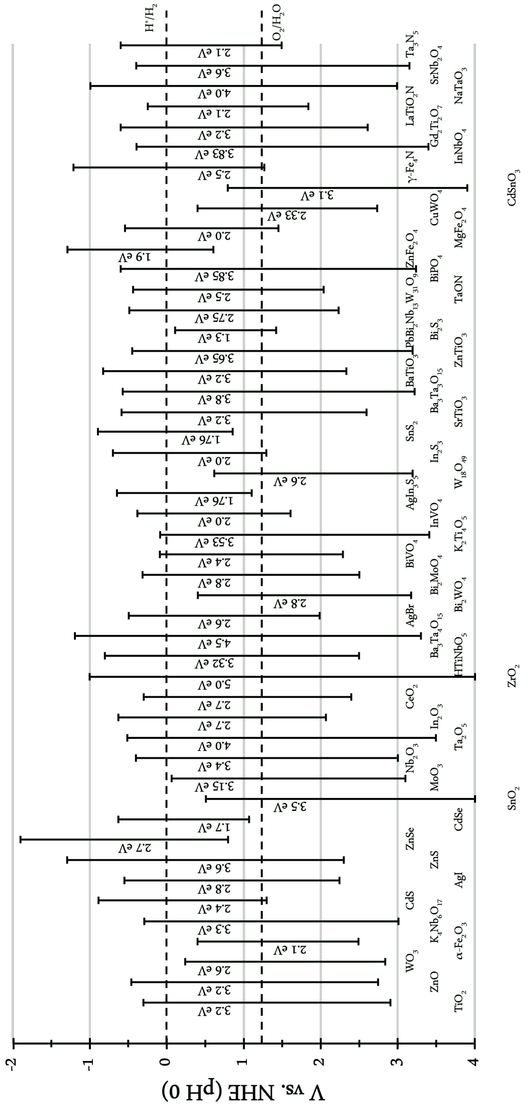

Figure 1.5. Band gaps and band positions of some semiconductors. Adapted with permission from ref.[4] Copyright 2014 Advanced Functional Materials.

- $BiVO_4$ is the most studied, even though its energy gap is relatively large it is direct (unlike the energy gap of other materials that are narrower but indirect and result in inefficient charge transport);
- Ferric spinels (MFe_2O_4, where $M = Zn^{2+}$, Mg^{2+}, Ca^{2+}) show a tuneable energy gap, that is function of the cation;
- Copper-based mixed oxides are fairly stable and provide good charge mobility, however they often show low efficiencies.

Another class of materials, akin to the previous ones, is the one of oxynitrides, in which part of the oxygen is substituted by nitrogen that contributes to the decrease of the energy gap.[6]

However, this class of materials has a relevant shortcoming regarding the stability in working conditions. As a matter of fact, even though the position of the energy gap is suitable for the catalysis of water oxidation the materials are thermodynamically unstable in these conditions.[6]

During this PhD more focus was placed on the development of the cathodic material, while for the anodic material already developed $BiVO_4$-based materials where employed.

Cathodic Materials

Concerning the catalysts for water reduction, a first class of materials is made of phosphor-containing species (namely phosphides and phosphates).

However, even though these kinds of materials are very active as water reduction catalysts, this is only true in alkaline environment.

A second class of materials is that of metallic chalcogens, with a particular attention to sulphides and selenides, that have energy gaps narrower than the already-discussed oxides:

- copper sulphides and selenides have high molar attenuation coefficients and good charge transport properties;
- some simple sulphides and selenides show stability issues; however, these can be made up for with layers of protective materials.

Among other types of materials:

- $III - V$ semiconductors were already proven as efficient absorbents and they were employed in the field of photovoltaics; however, their strong water instability would require the usage of very effective protective layers;[6]
- some carbon-species with good electronic-conduction properties have been assessed; however they are also unstable in water, with the exception of polymeric carbon nitride structures.

Graphitic Carbon Nitride

Among the different forms of carbon nitride, the most studied is C_3N_4, that is known since the first half of '800 and exists in five different polymorphs: $\alpha - C_3N_4$, $\beta - C_3N_4$, graphitic-C_3N_4, cubic-C_3N_4 and pseudo-cubic-C_3N_4.[7] In particular, g-C_3N_4 has a 2D structure that reminds of graphite, from which it differs because some of the carbon atoms are substituted with nitrogen.

The structure of g-C_3N_4 is made of 1,3,5-triazine rings, connected through nitrogen atoms that form a system of coordinated π bonds. Since its structure is made only of carbon-nitrogen covalent bonds, C_3N_4 is very stable, not only in neutral conditions but also in acidic and basic media.

Additionally, the band structure of C_3N_4 makes it a semiconductor that can absorb the visible light and act as a photocatalyst for redox reactions, oxidizing the molecules adsorbed on nitrogen sites and reducing those on carbon-sites;[7] and the conjugated system, also, provides some specific characteristics:

- electrical, that allow it to catalyse many organic reactions;
- nucleophilic, that allow it to catalyse reactions involving CO_2;
- electrostatic, that allow it to form hydrogen bonds;

these characteristics make g-C_3N_4 a very versatile catalyst.

As a semiconductor, g-C_3N_4 absorbs the radiation with an energy of $2.7\,eV$, that promotes the electrons from the valence band to the conduction band, creating the charge carriers.

Electrons and holes are very reactive species (with oxidizing and reducing activities) which can: recombine, remain trapped on metastable sites, or react with electron acceptors/donors that were previously adsorbed on the material's surface. Recombination is decreased by efficient charge separation and fast charge transport, that ensure enough lifetime for the charges to reach the active sites; however, the efficiency as a catalyst also varies, depending on the reaction involved.

The surface characteristics of g-C_3N_4 allow a good charge separation, despite this it is not an efficient photocatalyst on its own because of a few other aspects:[7]

- low quantum efficiency, owing to fast charge recombination;
- limited usage of the solar spectrum, since the peak of absorbance is in the range of blue light;
- low specific surface area and lack of porosity;
- grain boundary effect, that hinders the transfer of electrons through the grain interfaces to the surface.

To make up for these drawbacks, many studies worked on the optimisation of C_3N_4 by tuning: its microstructure, the concentration of the active sites, and the absorbance of solar radiation.

In particular, besides the synthesis of microstructure- and porosity-controlled materials, doping with non-metallic elements and formation of heterojunctions with noble metals or metal oxides were employed: doping changes the electronic structure of C_3N_4, increasing the absorbance of solar radiation; while heterojunctions are always used for separating the charges.

In case of C_3N_4-noble metal heterojunctions, the metal is often photoactive, since it is usually employed in nanometric form, and always acts as electronic trap due to a Fermi Level lower than C_3N_4. For C_3N_4-semiconductor heterojunctions, instead, different mechanisms of charge transfer may be involved, depending on the relative positions of the bands of the two materials:

sensibilisation: only C_3N_4 is photoactive, and the co-catalyst is only used to accumulate the charges;

double migration: both materials are photoactive, and electrons and holes migrate respectively to the material with lower conduction band and higher valence band;

Z-scheme recombination: both materials are photoactive, and the electrons in the lower conduction band recombine with the holes in the higher valence band.

During this PhD focus was placed on the optimization of the photocatalytic properties of C_3N_4 via the formation of heterojunctions with other semiconductors.

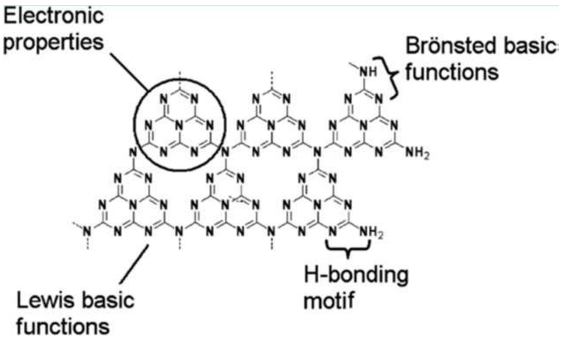

Figure 1.6. Structure of g-C_3N_4 and its functionalities as a catalyst. Reprinted with permission from ref.[8] Copyright 2008 Journal of Materials Chemistry.

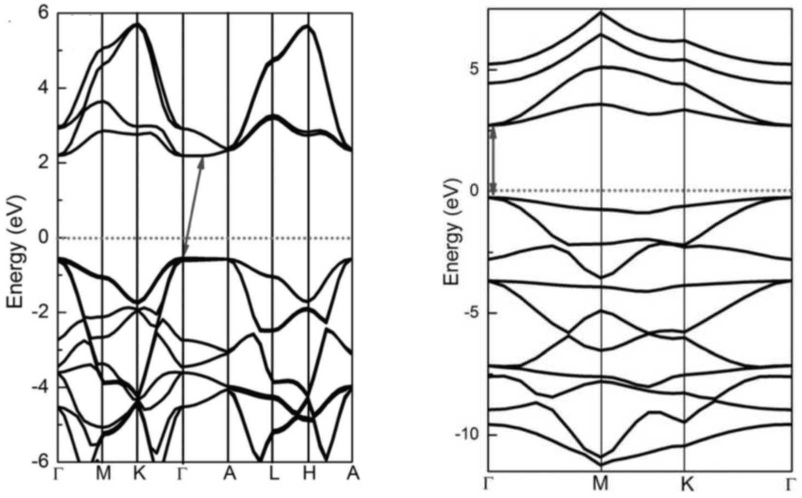

(a)

(b)

Figure 1.7. Band structure of a) bulk g-C_3N_4 and b) monolayer g-C_3N_4. Reprinted with permission from ref.[9] Copyright 2016 Physical Chemistry Chemical Physics.

1.4 Perovskites

Perovskites are a class of materials that has been attracting increasing attention in many fields of science and engineering, ever since the 1950s.

The term refers to materials with crystal structure similar to that of the $CaTiO_3$ mineral, that is the actual perovskite, and can represent not only synthetic materials but also many naturally existing minerals, for example the silicate phases that are believed to be the most abundant solid phase in the earth lower mantle.[10]

These materials have a general formula ABX_3, where A and B represent cations, A being larger than B, and X represents the anion; their structure is constituted by BX_6 octahedra, in between of which the A cations are placed, in the ideal form they are disposed in a cubic arrangement, while, in the less symmetric forms, some deviations are present, but the octahedra are always present.[10]

On the other hand, the functional characteristics of these materials are influenced by many factors, such as: cationic and/or anionic defects, the stoichiometry of the material, doping, and even the synthetic method.

The uniqueness of these kind of materials is given by their tailorability; in fact most of the elements of the periodic table can occupy either the A or B site (or both), and the same site can also be filled by a combination of elements, or vacancies;[10] and a variety of anions can also occupy the X site, as is depicted in Figure 1.8, and perovskites can be classified according to the nature of their anion:[10]

Inorganic Oxide Perovskites, these are among the most common perovskites, they can be intrinsic or doped, and their crystal structure (which often deviates from the cubic one) can change as a function of the temperature and pressure and cause a change in the material's properties;

Halide Perovskites, this is the other common class of perovskites, along with the oxide one; they are divided in alkali halides and organo-metal halides.

Among these, alkali fluorides exhibit antiferromagnetic properties, while both alkali and organometal chlorides, bromides

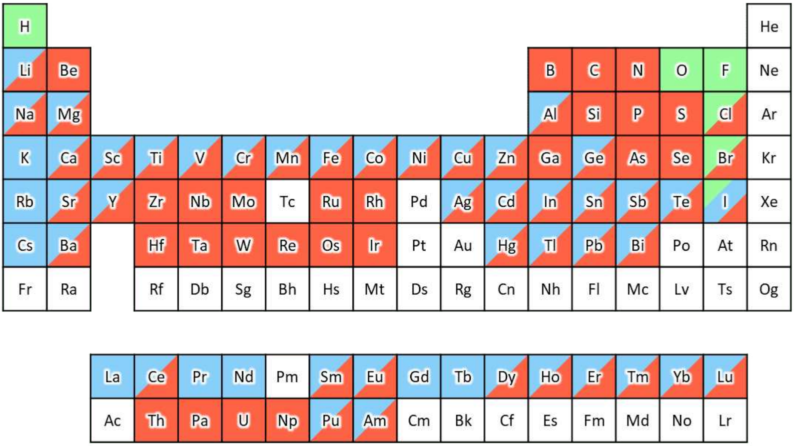

Figure 1.8. Periodic table representing the possible A-site (in blue) and B-site (in red) cations, and X-site (in green) anions in the perovskite structured materials. Adapted with permission from ref.[10] Copyright 2020 CRC Press.

and iodides manifest superior optical properties. However, most of these materials contain Pb as B-cation, the toxicity of which gave rise to the recent breakthrough of the ”lead-free environmentally friendly halide perovskites”;

Hydride Perovskites, they are rare, and they form when the hydrides of A and B are heated under high pressure of H_2. Since the process is reversible, they are studied as hydrogen storage materials;

Perovskite Hydroxides, these are also among the less common materials, they have the structure of double perovskites, rather than simple ones, and display peculiar optical and electronic properties.

Perovskites can also be classified according to their structure, that are quite varied;[10] however this flexibility of the structure, and the sudden attention that was given to these materials over the last couple decades, caused a general misunderstanding and misuse of the denomination of ”perovskite”.[11]

As was mentioned at the beginning, the perovskite crystal structure is made of a 3D network of corner-sharing BX_6 octahedra, surrounded by the A cations. The aristotype perovskite crystallises in the $Pm\bar{3}m$ space group, however the vast majority of the perovskites crystallize in a phase with reduced symmetry due to some deviations in the structure,[11] as is depicted in Figure 1.9a:

Distorted Perovskites, they contain tilted octahedra, that result in a tetragonal or orthorhombic structure, due to the difference in the dimensions between the A, B and X ions, as determined by the Goldschmidt Tolerance Factor;

A-Site Vacant Perovskites, the A cation is completely replaced by vacancies, and the stoichiometry of the perovskite is thus changed to BX_3;

Ordered Perovskites, in this case, the B cations are replaced either by a combination of etherovalent cations (that are placed at specific crystallographic sites, they are also called ”Double Perovskites”), or by a single metal in two different oxidation states, or by a combination of vacancies and etherovalent cations (the proportion of which is determined by the oxidation state of the cation, they are also called ”Vacancy Ordered Perovskites”)

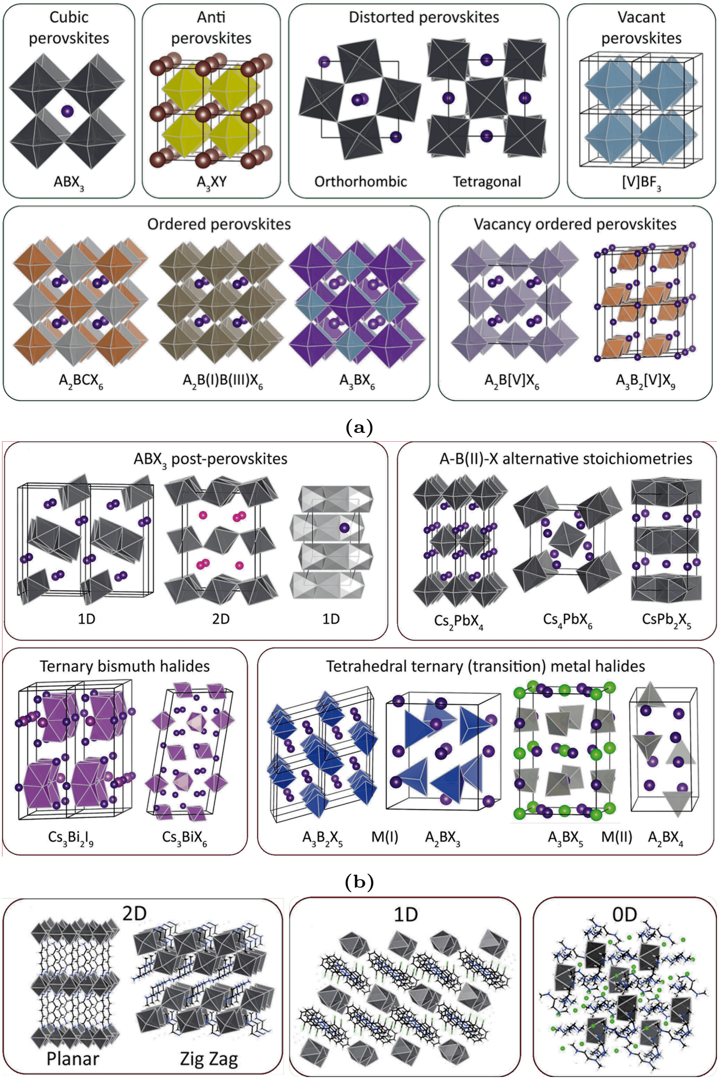

(a)

(b)

(c)

Figure 1.9. Overview of a) different halide perovskites, b) ternary metal halides not crystallizing in a perovskite structure and c) layered and hybrid organic-inorganic metal halides. Adapted with permission from ref.[11] Copyright 2020 ACS Energy Letters.

Inverse Perovskites, they contain A cations with higher oxidation states than the B cations; this happens when the A cations are very large, and the B ones are very small;

Anti-Perovskites, in this case, the A and B sites are occupied by anions (respectively monovalent and divalent), and the X site is occupied by a monovalent cation.

Other more relevant variations bring about the collapse of the perovskite structure, and such structures can thus only be referred to as "Perovskite-Derivatives"; however they also manifest equally promising properties, in the fields of: solid electrolytes, ferroelectrics, piezoelectrics, superconductivity, catalysis, and optoelectronics.[11] Some of these kinds of materials are represented in Figures 1.9b-1.9c, and they can be classified as:[11]

Structures with A Cation too Large or too Small, as determined by the Goldschmidt tolerance factor, such materials cannot form a perovskite as such structure is not geometrically stable; they crystallize in lattices with either 1D or 2D edge-sharing octahedra, or 1D face-sharing octahedra;

Structures with B Cation much Smaller than the X Anion, as determined by the Octahedral Factor (used to determine the stability of the octahedral symmetry), such combinations generally prefer a tetrahedral coordination, rather than an octahedral one;

Post-Perovskites, they are materials that cannot crystallize with a perovskite lattice under ambient conditions, however they do so at high temperature or pressure;

A_4BX_6 Materials, they are often referred to as "0D Perovskites", however they cannot be considered so, as in this case the atoms have an octahedral coordination, but they are not in the crystallographic site typical of a perovskite;

AB_2X_5 Materials, they are sometimes referred to as "2D Perovskites", however they do not even contain the BX_6 octahedra.

Another type of materials are the Layered Materials, they are often referred to as "Layered Perovskites" or "2D Perovskites", however they are made of only one or a few 2D layers of BX_6 octahedra (instead of the canonical 3D network) separated by a layer of cations or of a material with a different structure (this mainly depends on the nature of the material as oxides and alkyl or organo-metal halides have very different characteristics); as such the belonging of these kind materials to the perovskite class is debatable.

In any case, they can also be further classified as "Ruddlesden-Popper Phases", "Dion-Jacobson Phases", "Aurivillius Phases" and "$A_nB_nO_{3n+2}$-Layered Structures" based on the actual type of separating layer.[10]

Due to their optical properties, during this PhD focus was placed on the study of halide perovskites and halide perovskite-derived phases.

Metal Halide Perovskites and their Derivatives in Photocatalysis

In this paragraph, some extracts of the review "Solar-Driven Hydrogen Generation by Metal Halide Perovskites: Materials, Approaches, and Mechanistic View",[12] that was published during this PhD, will be reported with minimal adaptation.

In very recent times, Metal Halide Perovskites (MHPs) have attracted a significant interest for their possible use in various photocatalytic applications.[13–16] The suitability of MHPs in relevant solar-driven reactions comes essentially from their highly tuneable and narrow band gap, long carrier lifetimes, and high mobilities, together with a good defect tolerance. The band alignment of various MHPs, together with traditional photocatalysts, relative to the potentials of common redox half-reactions, is shown in Figure 1.10, indicating the thermodynamic suitability of these materials to effectively run reduction reactions and even oxidation reaction, for MHPs with higher bang gap values.

In addition to the thermodynamic suitability, MHPs also possess good charge carrier dynamic properties resulting in low excitation binding energies, efficient charge carrier generation, and long-lived excited states.

Among the different solar-driven reactions of current interest, MHPs have been explored for their possible use in H_2 generation, CO_2 reduction, photodegradation of dyes and contaminants, and photosynthesis of organic compounds.

Focusing on H_2 generation, the first report of H_2 photogeneration appeared in 2017 when methylammonium lead iodide ($MAPbI_3$) was employed.[17] In order to overcome the water-induced instability of the perovskite, the reaction was carried out in aqueous HI solution. By controlling the I^- and H^+ concentrations, powdered $MAPbI_3$ underwent a continuous dissolution and precipitation under a dynamic equilibrium, which allowed a stable photocatalytic HI splitting.

An improvement in hydrogen photogeneration activity by MHPs in acid solutions was achieved by creating composites in analogy with the strategies employed for more traditional photocatalysts. For instance, composites of $MAPbI_3$ with reduced graphene oxide[18] or Ni_3C[19] were studied.

At the same time, other results reported the possible photocatalytic use of MHPs in water and/or organic solvents, that are of particular interest to further extend the photocatalytic applications of MHPs, being the natural environments for water splitting and possible organic photoreactions.

For instance, it was demonstrated that $DMASnI_3$ (DMA = dimethylammonium) is stable in pure water for up to $16h$ without dissolving.[20] A few other examples of hydrogen generation were achieved in organic solvents by employing nanocrystalline MHPs, such as a system composed of $CsPbBr_3$ nanocrystals and Ru@TiO_2 nanoparticles,[21] which are excellent visible light emitting materials.[22]

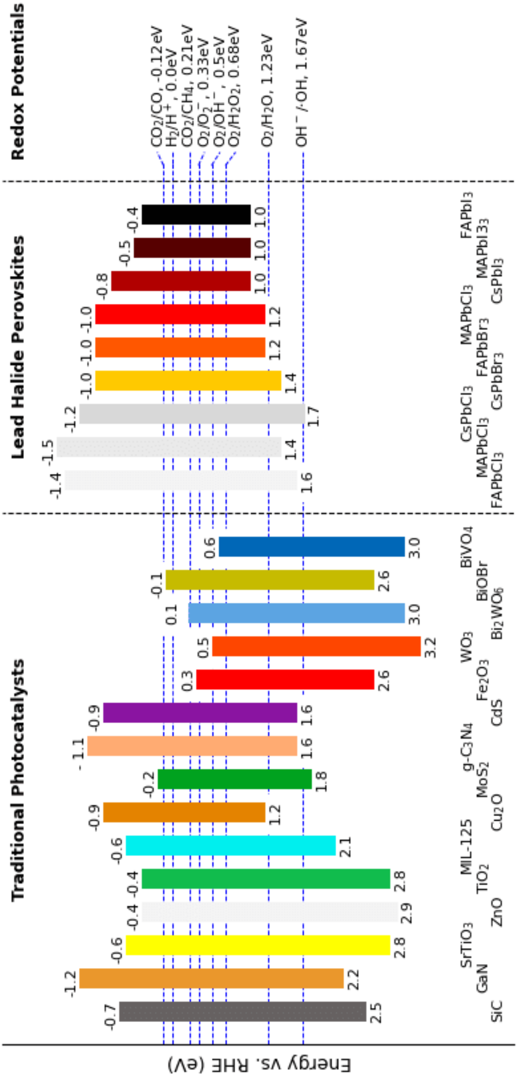

Figure 1.10. Band edge positions of conventional photocatalysts and different MHPs relative to Reversible Hydrogen Electrode (RHE). For comparison, the redox potentials of some common half-reactions are also presented. Adapted with permission from ref.[13] Copyright 2020 ACS Energy Letters.

Chapter 2

Development of the Materials

In this chapter the materials employed and the optimization of their synthesis will be described, (starting from the anodic and continuing with the cathodic ones) along with their physical characterisation; while details on the fabrication of the electrodes will be dealt with in the next chapter.

2.1 Anodic Materials

$BiVO_4$

In the scientific literature many synthetic strategies, that employ different techniques, are reported for the deposition of bismuth vanadate, $BiVO_4$, thin films:

Electrodeposition, it is among the most widespread techniques, and it involves the occurrence of some redox reactions on the surface of an electrode-substrate. In this way $BiVO_4$ is formed directly on the surface of the electrode-substrate, from its precursors that are present in the electrolytic solution and are involved in the redox reactions.
Electrodeposition is usually conducted in two ways, the first is the electrodeposition of a film of Bi_2O_3 followed by the deposition of a solution containing the vanadium precursor and

calcination;[6, 23] the second is the direct electrodeposition of $BiVO_4$;[24]

Spin Coating, is a just-as-widespread technique for the deposition of a solution of the precursors of $BiVO_4$, that are later reacted by calcination;[25, 26]

Spray Pyrolysis, is a technique that uses a solution of the precursors, that is sprayed on top of a hot substrate, in order to activate their reaction and obtain $BiVO_4$;[27]

Pulsed-Laser Deposition, is a type of Physical Vapor Deposition, that employs a pulsed laser to vaporize already-synthesized $BiVO_4$, in the form of powder, that later condenses on the surface of the substrate.[28]

During this PhD work, it was chosen to adopt a combustion synthesis (that employed a thermal reaction for the syntesis of $BiVO_4$, like spin coating and spray pyrolysis, but differed in the deposition method, as drop casting was adopted); this was optimized starting from the one reported by Qayum et al.[29]

Optimization of the Synthesis

The synthesis requires the preparation of a liquid and equimolar solution of the precursors of $BiVO_4$ (bismuth nitrate, $Bi(NO_3)_3$, and ammonium metavanadate, NH_4VO_3).

Compared to the synthesis reported by Qayum et al. a different solvent was employed to prepare the precursor-solution: a mixture of water and nitric acid was used instead of ethylene glycol, that proved to be a poor solvent for ammonium metavanadate. In this way a monophasic product was formed, as one can infer comparing the XRD patterns reported in Figure 2.1.

When fabricating the electrodes, this precursor solution is drop-casted onto the electrode substrate and thermally treated at 200 °C to trigger the combustion that brings about the formation of a solid and compact layer of $BiVO_4$; lastly, the material formed in this way is sintered in oven, at 650 °C.

When synthetizing the material in the form of powder, the precursor solution was placed inside a ceramic crucible and directly heated, and the solid product was later scrubbed from the crucible walls.

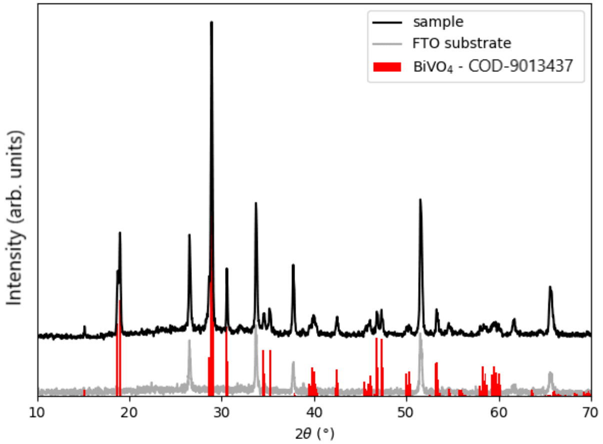

Figure 2.1. XRD pattern of a sample of a $BiVO_4$ film deposited onto an FTO crystalline substrate.

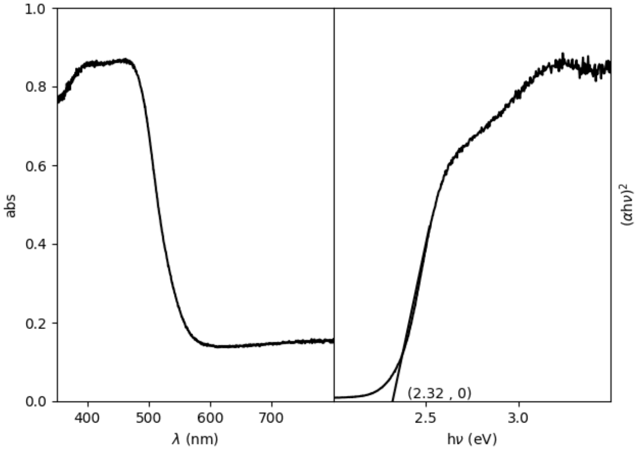

Figure 2.2. UV-Vis absorption spectrum (left) and Tauc plot (right) of the synthesized $BiVO_4$ powder.

Optical Characteristics of the Material

To determine the optical characteristics of the material, UV-Vis absorption measures were performed.

These allowed to determine that $BiVO_4$ has a threshold of adsorption between $480 - 520\,nm$, as can be seen from the absorption curve in Figure 2.2, that corresponds to an energy gap of $2.32\,eV$ (determined through the Tauc plot method, Figure 2.2).

The morphological and photo-electrochemical characteristics of the material will be discussed in the next chapter, as they are strictly related to the conditions of the film deposition.

2.2 Cathodic Materials

For the cathodic materials, development of C_3N_4 will be briefly described, while the papers published during this PhD will be reported with minimal adaptation for the description of the development of the C_3N_4/co-catalyst composite systems.

The determination of the Hydrogen Evolution Rates (HERs) of the materials was performed in collaboration with the group of Professor Profumo, of the University of Pavia, while, for the studies on the C_3N_4/co-catalyst systems, the Density Functional Theory (DFT) calculations were performed in collaboration with the group of Professor De Angelis, of the University of Perugia.

C_3N_4

During this PhD project it was chosen to develop materials based on carbon nitride, C_3N_4, in consideration of its merits more than its shortcomings:

flaws: low specific surface area, low quantum efficiency;

values: absorbance of visible light, heavy-metal-free material, easy and low-cost synthesis.

The synthesis of bulk-C_3N_4 is simple, highly reproducible, and vastly documented in literature, therefore there was no need for optimization.

It consists of a thermal polymerization under inert atmosphere; the reagent is an organic precursor that contains carbon and nitrogen atoms (usually dicyandiamide, melamine, or urea), and the process can be carried out between 450 – 650 °C.[7,30]

Characteristics of the Material

The synthesis was successful, with no need of optimization, as can be seen from the XRD pattern of the sample shown in Figure 2.3, that presents the exact characteristics of the XRD patterns reported in literature for this low-crystallinity material.[31]

The UV-Vis absorbance spectrum is represented in Figure 2.4; it allowed to determine that the material has an absorption edge between $400 - 460nm$, that correspond to an energy gap of $2.72eV$ (determined through the Tauc plot method), followed by a weaker absorption that extends until $600nm$. This means that C_3N_4 strongly absorbs the radiation near the UV-boundary, but also weakly absorbs the radiation at higher wavelength.

The Scanning Electron Microscopy (SEM) images reported in Figure 2.5 show how the material does not have a definite morphology but is composed of randomic aggregates of smaller particles, with the bigger ones that may also contain some smaller structures within them.

Development of the Material

In the more advanced stages of experimentation, modifications were made to the synthetic process, in order to increase the specific surface area of the material (Table 2.1):

thermally exfoliated C_3N_4: as was documented,[32–35] when already synthesised-C_3N_4 undergoes a thermal treatment, at ≈ 500 °C, it experiences an exfoliation process that increases its

Table 2.1. Specific surface area of the different C_3N_4 materials.

Sample	**Specific Surface Area ($m^2\,g^{-1}$)**
bulk C_3N_4	4
thermally exfoliated C_3N_4	103
Ca included C_3N_4	18

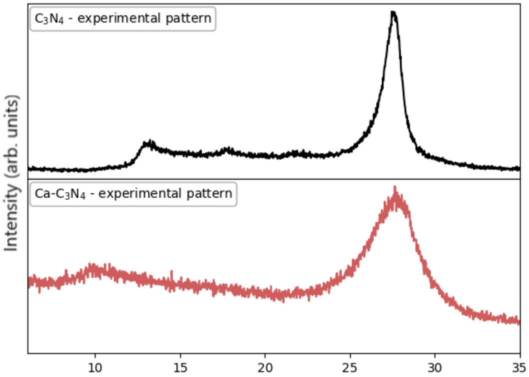

Figure 2.3. XDR patterns of the synthesized C_3N_4 and Ca included-C_3N_4 powders.

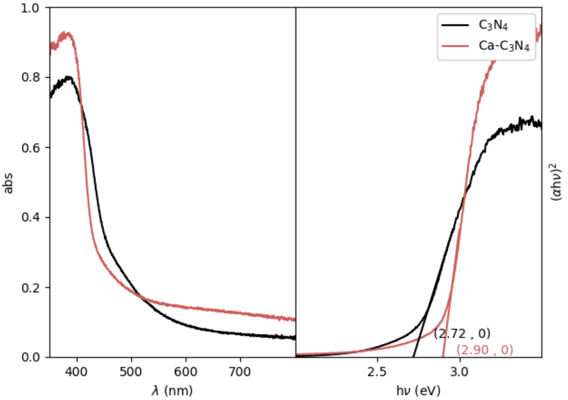

Figure 2.4. UV-Vis absorption spectrum (left) and Tauc plot (right) of the synthesized C_3N_4 and Ca included-C_3N_4 powders.

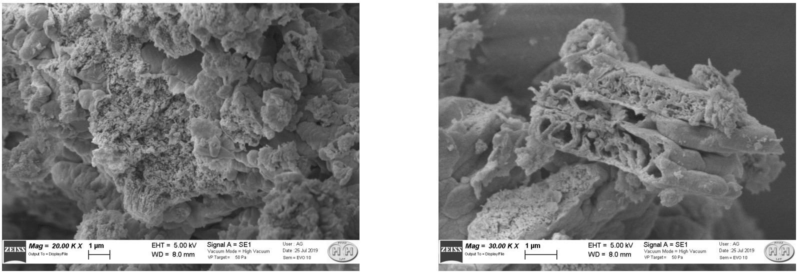

(a) (b)

Figure 2.5. SEM images of the synthesized C_3N_4 powder.

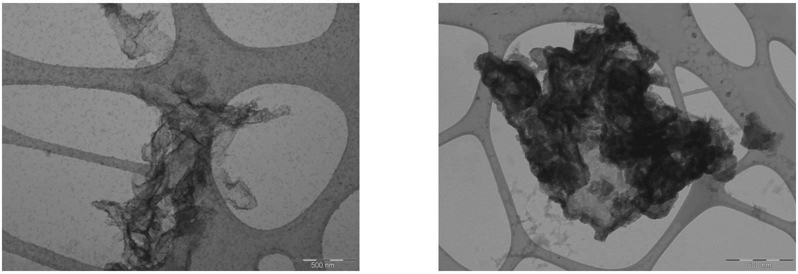

(a) (b)

Figure 2.6. TEM images of the exfoliated C_3N_4 powder.

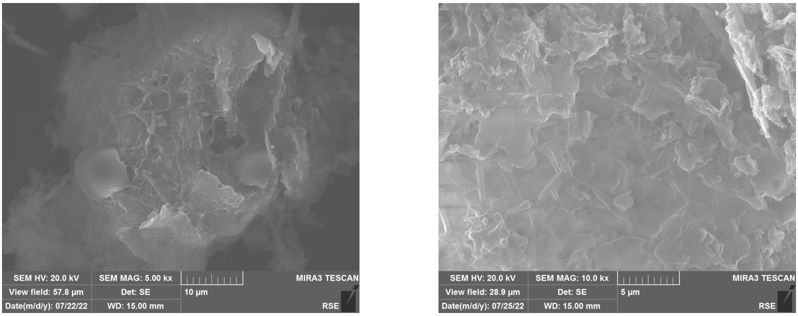

(a) (b)

Figure 2.7. SEM images of the synthesized Ca included C_3N_4 powder.

specific surface area, as witnessed by the Transmission Electron Microscopy (TEM) images in Figure 2.6;

C_3N_4 with Ca inclusions: another way to increase the specific surface area of C_3N_4 is to perform the synthesis in presence of large quantities of an inert salt, as can be seen from the SEM images in Figure 2.7. $CaCl_2$ was added in a ratio of 10 : 1 to the organic precursor and was later washed away, first with water and then with aqueous HCl to eliminate most of the inert salt leaving only a part of the included Ca ($\approx 15\%\,atomic$, quantified through Energy Dispersive X-ray Spectroscopy, EDS).

It was verified that, while the structure experienced no evident modification, the band gap of the material was slightly increased (Figures 2.3-2.4)

Functional Characteristics of the Material

All these materials, as well as the composite materials later described, were subjected to preliminary tests of hydrogen photoproduction from aqueous suspension.

For these experiments a standard procedure was adopted,[36] that involves the irradiation of a degassed suspension of the catalyst (with a concentration of $1\,g\,L^{-1}$) in an aqueous solution of a sacrificial agent (triethanolamine, TEOA, with a concentration of $10\%\frac{V}{V}$) that serves as hole-acceptor, and the addition of $3\%wt$ of Pt that helps to increase the reaction yield, and the analysed-signal.

The experiments were performed for a fixed amount of reaction time, that is $6h$. The determination of the hydrogen production was then based on a Gas Chromatographic (GC) analysis performed on the headspace of the closed reaction vessel.

The HERs are shown in Figure 2.8 and summarized in Table 3.9 and show that the presence of the catalyst greatly enhances the hydrogen photoproduction, especially in the case of the thermally exfoliated and Ca included materials.

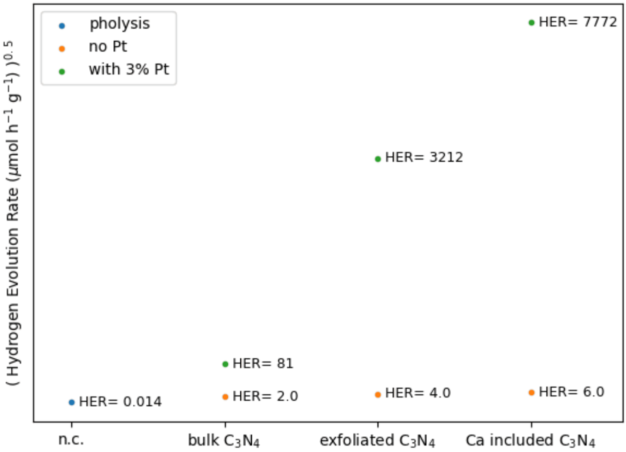

Figure 2.8. HERs of the tested C_3N_4 powders.

Table 2.2. HERs of provided by the different C_3N_4 materials suspended in 10% TEOA solution.

Sample	**HER** $(\boldsymbol{\mu mol\, h^{-1}\, g^{-1}})$	
	bare sample	$\mathbf{+\,3\%\,\boldsymbol{wt}}$ **Pt**
bulk C_3N_4	2.0	81
thermally exfoliated C_3N_4	4.0	3212
Ca included C_3N_4	6.0	7772
no catalyst	0.014 *	
* since no catalyst in present, the unit is $\mu mol\, h^{-1}$		

$DMASnBr_3$

Water-Stable $DMASnBr_3$ Lead-Free Perovskite for Effective Solar-Driven Photocatalysis[37]

Purpose

In this work we reported clear evidence of water stability in a lead-free metal halide perovskite, namely dimethylammonium tin bromide ($DMASnBr_3$), obtained by means of diffraction, optical and X-ray photoelectron spectroscopy.

Such unprecedented water stability has been applied to promote photocatalysis in aqueous medium, by devising a novel composite material by coupling $DMASnBr_3$ to C_3N_4, taking advantage from the combination of their optimal photophysical properties. The prepared composites provide an impressive HER ($> 1700\, mmol\, g^{-1}\, h^{-1}$) generated by the synergistic activity of the two composite constituents. DFT calculations provide insight into this enhancement, deriving it from the favourable alignment of interfacial energy levels of $DMASnBr_3$ and C_3N_4. The demonstration of an efficient photocatalytic activity for a composite based on lead-free metal halide perovskite in water paves the way to a new class of light-driven catalysts working in aqueous environments.

Introduction

MHPs possess unique optical properties, such as high optical absorption in the visible region, tuneable band-gap and long carrier lifetime, which have been extensively exploited in photovoltaics and optoelectronic applications.[22] More recently there has been a growing interest towards novel applications of MHPs, in particular in the field of solar-driven photocatalysis.[13] Compared to traditional metal oxide photocatalysts, MHPs possess relatively narrow band gaps, allowing the absorption of low-energy photons.[13] In addition, the electronic band structure of many perovskites places their band edges in excellent positions to perform hydrogen photogeneration and carbon dioxide photoreduction.[13] However, some of the most interesting photocatalytic reactions such as H_2O splitting, CO_2 and N_2 reduction, and dye degradation, require the use of water or alternative polar solvents, this represent a conundrum foreseeing MHPs utilization. It is well known, in fact, that MHPs are highly unstable upon moisture and water exposure, therefore those media are hardly compatible with most of the current known MHPs.[13, 38, 39] Due to these constrains, the demonstration of hydrogen photogeneration by using $MAPbI_3$ (MA^+ = methylammonium), has been only possible in dynamic equilibrium with aqueous hydrogen iodide (HI).[17, 19, 40, 41] In addition to the use of saturated halo acids, other strategies to overcome the water-instability of MHPs consider the use of low-polarity solvents and encapsulation strategies.[13] These last approaches have been used, for example, in several photocatalytic organic syntheses, such as C−C, C−N and C−O bond-formations, another very exciting field where the photophysical properties of MHPs could provide unprecedented opportunities to researches.[42] Clearly, the possibility of employing MHPs as photocatalysts and co-catalysts, in photocatalytic reactions in aqueous environment, could open an unprecedented novel field of applications, which can take advantage of their superior, as well as highly tuneable, electronic properties.

Triggered by the aforementioned opportunities, growing interest for water stable MHPs is fostering current research. Materials such as the $DMASnX_3$ (X = Br and I) family, have shown an impressive stability when immersed in water, as confirmed by the collection of the XRD patterns before and after water interaction.[20, 43] In these reports, the MHPs do not dissolve in water but they rather remain dispersed in solution, maintaining unchanged the crystal structure and the optical properties.[20, 43] The precise origin of the superior stability of these phases is not yet known, but it could be related to the relatively high hydrophobic nature of the DMA cation. Both $DMASnBr_3$ and $DMASnI_3$ systems owing to their exceptional water stability call for potential eco-friendly applications and so they have been used as photocatalyst for H_2 evolution in deionized water rather than in saturated hydroiodic acid (HI) solution, with a H_2 evolution rate of about 1 (for $DMASnBr_3$) and 0.6 (for $DMASnI_3$) $mmol\, h^{-1}\, g^{-1}$ and with good recycling properties.[20, 43]

Focusing on the photocatalytic hydrogen generation, except for the $DMASnX_3$ compositions cited above, the use of MHPs in dynamic equilibrium with aqueous halo acids does not appear to be a practical solution, as it requires the presence of high amounts of HX to avoid perovskite degradation and, in addition, the use of lead-based soluble perovskites precursors may be environmentally hazardous due to possible lead contamination.

Motivated by the above considerations, we decided to afford a more detailed study on $DMASnBr_3$ MHP exploitation in photocatalysis.[43] In order to improve the HER performance of $DMASnBr_3$, we devised a novel approach based on the synthesis of composites between the MHP and a well-known visible light photocatalyst, namely graphitic carbon nitride, C_3N_4.

C_3N_4, has become the state-of-the-art photocatalyst under visible-light, featuring a relatively narrow band gap (ca. $2.7eV$) and conduction and valence band positions suitable to run relevant oxidation and reduction processes.[44, 45] To further improve the properties of individual C_3N_4, in particular to increase charge migration and recombination time, and to extend the absorption range, significant research has been devoted to the preparation of C_3N_4 composites with metals, bimetals, semiconductors (oxides, sulphides, and the like), graphene, carbon dots, conductive polymers, sensitizers, among others, showing a promising improvement of the HER.[46, 47] Based on these reports, we performed an investigation of the possible use of the $DMASnBr_3$ perovskite as an efficient co-catalysts for carbon nitride, trying to exploit its beneficial and superior optical properties and taking advantage of preliminary evidence of water stability of this and related materials.[20, 43]

Experimental Methods and Discussion

Before addressing the use of $DMASnBr_3$ in photocatalysis, we elaborated on its physical characteristics. Figure 2.9a shows a sketch of the $DMASnBr_3$ crystal structure, characterized by distorted edge-sharing $SnBr_6$ octahedra, while Figure 2.9b reports the XRD pattern of a sample prepared by mechanochemical synthesis, starting from DMABr and $SnBr_2$ milled at $300rpm$ for $12h$, confirming the expected orthorhombic structure (*Pbca*) (Figure 2.9b), thus indicating that ball-milling is a good synthetic strategy also for Sn-based perovskites.[48, 49]

Water-stability of the perovskite has been checked by suspending it in Deionized Water (DW), followed by stirring for $4h$ and filtering. By visual inspection, suspended powders are clearly visible in the aqueous phase.

We also tested the potential leaching of Sn in water by determining, with Inductively Coupled Plasma-Optical Emission Spectroscopy (ICP-OES) analysis, the amount of tin contained in the water where

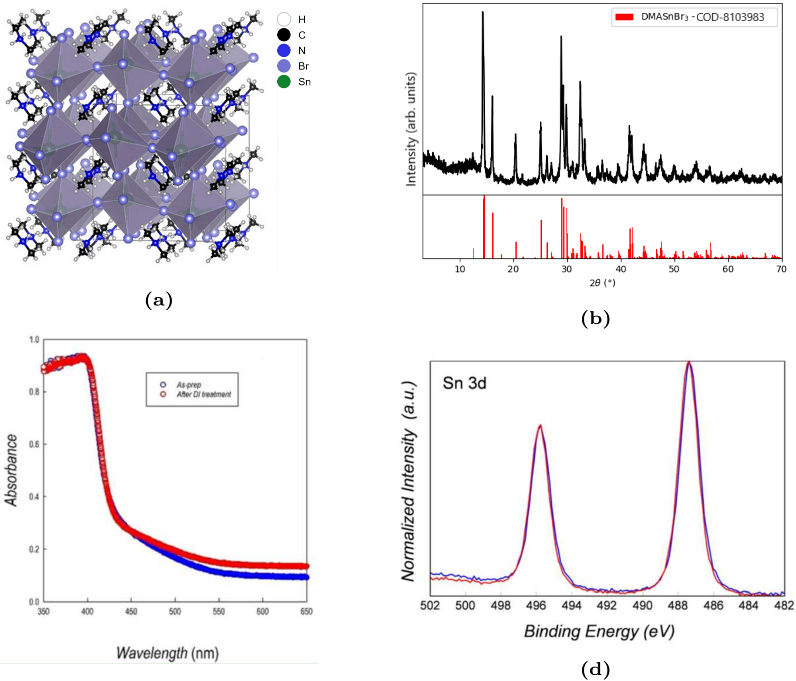

(a)

(b)

(c)

(d)

Figure 2.9. a) Schematic representation of $DMASnBr_3$ crystal structures; b) XRD pattern of the as-synthesized $DMASnBr_3$ and reference pattern; c) UV-Vis spectra of as-synthesized $DMASnBr_3$ (blue) and after recovery from aqueous solution (red); d) Sn 3*d* XPS spectra of as-synthesized $DMASnBr_3$ (blue) and after recovery from aqueous solution (red). Reprinted with permission from ref.[37] Copyright 2021 Angewandte Chemie International Edition.

the perovskite had been suspended under stirring for $4h$. The analysis demonstrates that less than 0.5% wt of the starting Sn, based on the amount of Sn in the starting suspended powder, is released from the MHP in water after this stirring time. Time-dependent release study up to $32h$, under the same experimental conditions, confirmed the perovskite water stability, by showing a Sn release of about 5% wt.

In addition, Figure 2.9c compares the UV-Vis spectrum of the as-prepared $DMASnBr_3$ with the spectrum of the sample after being treated in DW, confirming that the optical properties as well are unaltered by the water treatment.

Finally, a further and definitive confirmation of the water stability of $DMASnBr_3$ was obtained by X-ray Photoelectron Spectroscopy (XPS). Figure 2.9d reports the Sn $3d$ spectra of the as-prepared sample and of the sample after water treatment: the perfectly overlapping spectra, with unchanged peak shape and position (Sn $3d_{5/2}$ at $487.3eV$), clearly demonstrate that our material is stable under water treatment, also confirming the +2 oxidation state of Sn without any evidence of sample oxidation.[50]

All this evidence provides a solid and unambiguous proof of water stability of $DMASnBr_3$.

After having assessed the water stability of $DMASnBr_3$, we successfully prepared $C_3N_4/DMASnBr_3$ composites at different MHP loadings ranging from 1 to 33% wt. The samples have been prepared by means of mechanochemistry starting from mixtures of DMABr, $SnBr_2$ and C_3N_4 (previously synthesized from dicyandiamide decomposition at 600 °C in N_2 flux) and their crystal structures were characterized by XRD.

Figure 2.11a reports some selected patterns of the $C_3N_4/DMASnBr_3$ composites at varying % wt of MHP loading and shows that composites have an overall amorphous-like structure, with the main peak of C_3N_4 around 28° and the general sample scattering becoming progressively less intense with the increase of the amount of MHP. No clear diffraction peaks of crystalline perovskites are found in the patterns, suggesting that the presence of C_3N_4 during ball-milling tends to reduce the structural order of the $DMASnBr_3$.

Fourier-Transform Infrared spectroscopy (FT-IR) data (represented in Figure 2.10) suggest the presence of the MHP through specific fingerprint regions of the $DMASnBr_3$ in the composite.

However, a more conclusive information regarding the presence of

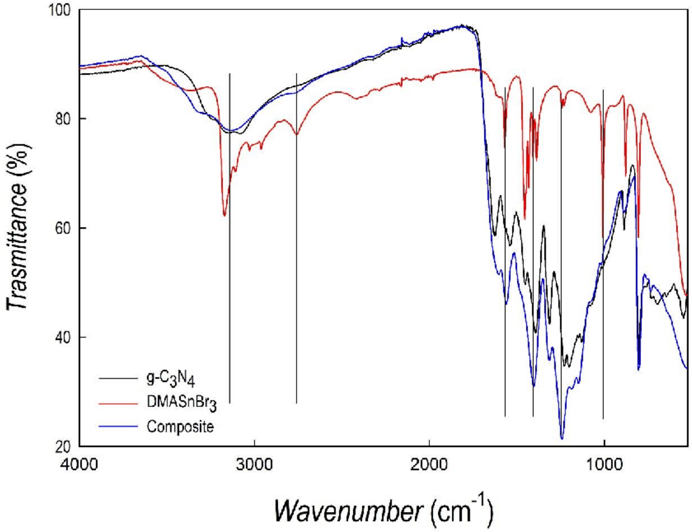

Figure 2.10. FT-IR data of C_3N_4 (black curve), DMASnBr$_3$ (red curve) and C_3N_4/DMASnBr$_3$ 33% *wt* (blue curve). Vertical black lines mark region of interest in the spectrum. Reprinted with permission from ref.[37] Copyright 2021 Angewandte Chemie International Edition.

the MHP in the composite was obtained by XPS analysis, carried out on the $C_3N_4/DMASnBr_3$ composite at $33\%\,wt$ loading, which is the most active one. Figure 2.11b compares the Sn $3d$ XPS spectrum of pristine $DMASnBr_3$ with that of the $C_3N_4/DMASnBr_3$ composite, showing the same peak position and shape. In addition, N $1s$ XPS spectra (Figure 2.11c) confirms the presence of the typical fingerprint of ammonium group ($401.4eV$) in the composite and its absence in the pristine C_3N_4.[51,52] These results rule out also the possible decomposition of the perovskite when included in the composites since this would lead to changes of the binding energies in the Sn spectra, which is not the case as clearly shown in Figure 2.11b.

SEM and Energy Dispersive X-ray Spectroscopy (EDS) analysis of composites are shown in Figure 2.12, indicating a morphology without distinct features, as anticipated due to ball-milling process, and micron-sized grains. The Br/Sn ratio determined over a large scanning area is in good agreement with nominal value (calculated as 2.95 (6) from the average of four measures).

Finally, TEM of the composites along with EDS data (on a smaller area of about $1mm^2$), shown in Figure 2.13, further confirm the composition and the local homogeneous distribution of the elements (i.e., Br, Sn, C and N).

Optical absorbance spectra of $C_3N_4/DMASnBr_3$ composites (15 and $33\%\,wt$), which are represented in Figure 2.14b, show a slight blue-shift with respect to C_3N_4 by increasing the amount of $DMASnBr_3$ with the band gap (calculated though the Tauc plots in Figure 2.14b) varying from $\approx 2.72eV$ (for pure carbon nitride) to $\approx 2.85eV$, without significant differences among the composites at the various perovskite loadings. This result could be anticipated considering the relatively small difference in the band gap between carbon nitride and $DMASnBr_3$.

Surface area of selected representative samples has been measured by B.E.T. adsorption method and the results are listed in Table 2.3. C_3N_4 shows the highest surface area ($\approx 26\,m^2\,g^{-1}$), and there is a trend towards lower values by increasing the loading of the MHP during the ball-milling process. Such synthetic route, while favouring the dispersion and improving the contact between the two materials, leads to a reduction of the surface area in the samples.[53–55] However, ball-milling is a very simple and straightforward synthetic method, suitable also for large scale catalyst synthesis.

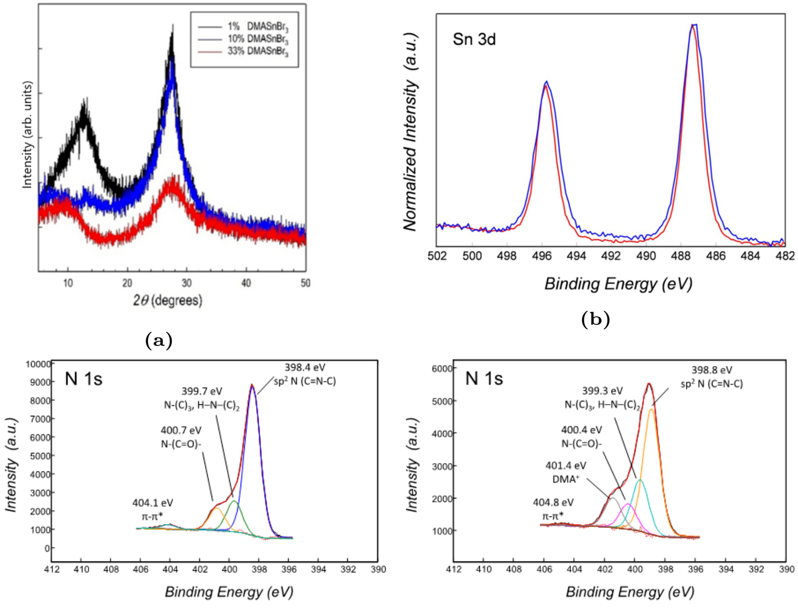

(a)

(b)

(c)

Figure 2.11. a) XRD patterns of C_3N_4/DMASnBr$_3$ composites at different percentages of metal halide perovskite loading; b) Sn $3d$ XPS spectra of DMASnBr$_3$ (red curve) and of C_3N_4/DMASnBr$_3$ composite at 33% *wt* (blue curve); c) XPS N1s spectra of C_3N_4 (left) and of the C_3N_4/DMASnBr$_3$ 33 %*wt* composite (right). Reprinted with permission from ref.[37] Copyright 2021 Angewandte Chemie International Edition.

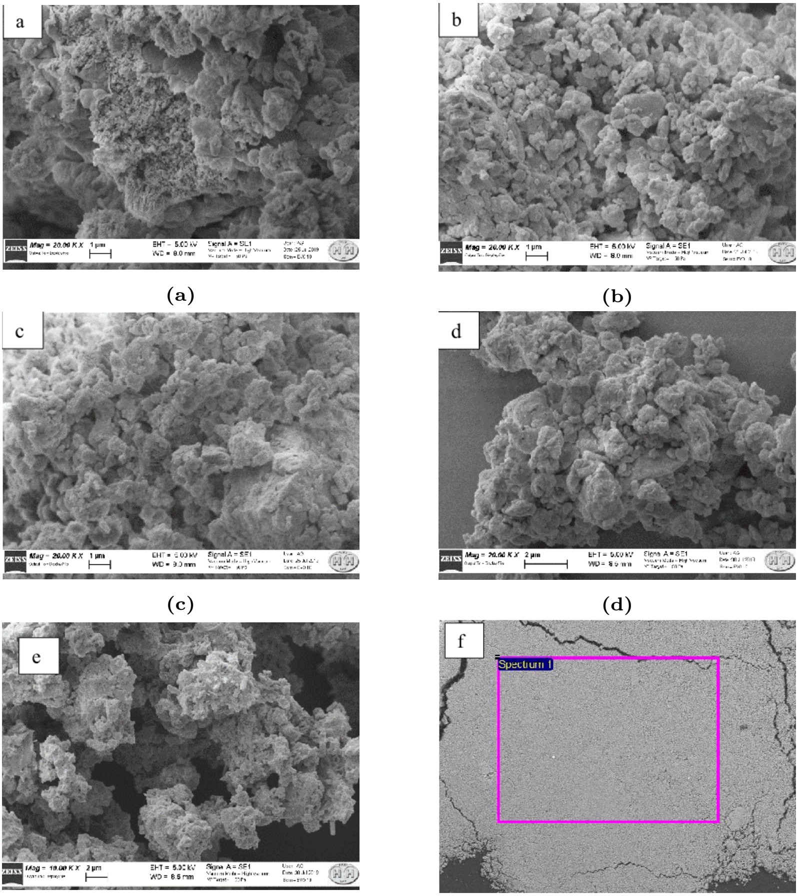

(a) **(b)** **(c)** **(d)** **(e)** **(f)**

Figure 2.12. SEM images of a) C_3N_4; b) C_3N_4/DMASnBr$_3$ 5% *wt*; c) C_3N_4/DMASnBr$_3$ 15% *wt*; d) C_3N_4/DMASnBr$_3$ 33% *wt*; e) DMASnBr$_3$; f) representative scan for EDS determination on C_3N_4/DMASnBr$_3$ 33% *wt*. Reprinted with permission from ref.[37] Copyright 2021 Angewandte Chemie International Edition.

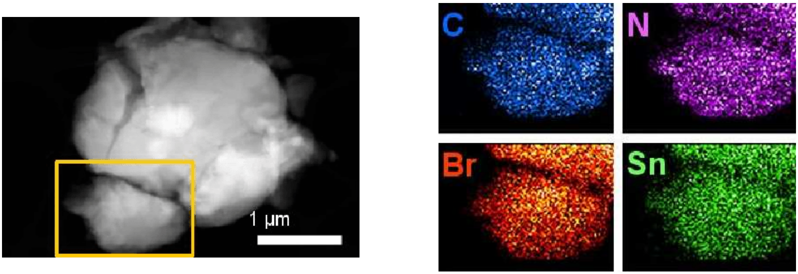

(a)

(b)

Figure 2.13. a) TEM micrograph and b) related elemental distribution maps on selected area of C_3N_4/DMASnBr$_3$ 33% *wt*. Reprinted with permission from ref.[37] Copyright 2021 Angewandte Chemie International Edition.

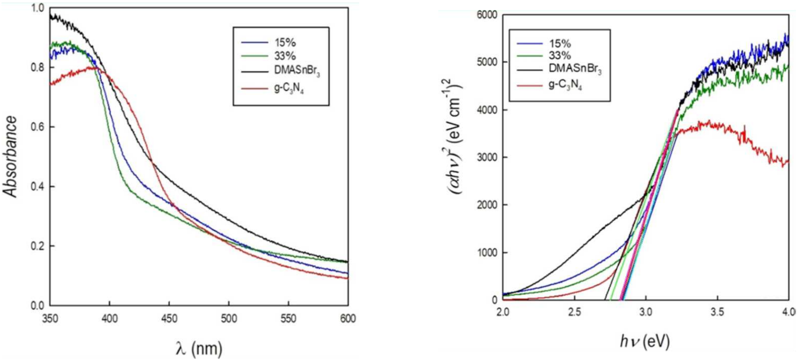

(a)

(b)

Figure 2.14. a) Absorption spectra and b) Tauc plots of C_3N_4/DMASnBr$_3$ composites and end-members. Reprinted with permission from ref.[37] Copyright 2021 Angewandte Chemie International Edition.

We determined the hydrogen photogeneration characteristics of the above discussed composites by employing common protocols used for similar C_3N_4-based composites.[44] The results reported in the following have been performed on several replicas.

Firstly, hydrogen photogeneration properties of the C_3N_4/DMASnBr$_3$ composite have been determined in $10\%\frac{V}{V}$ aqueous TEOA as a typical sacrificial agent, and without any metal co-catalyst (e.g., Pt). The HERs as a function of perovskite loading of the composites are shown in Figure 2.15a.

The composites perform significantly better than C_3N_4 alone, even for small perovskite amounts ($1\%\,wt$) (see Table 2.4), and the highest HER ($\approx 19\,\mu mol\,g^{-1}\,h^{-1}$) for the composite represents a nearly 10-fold improvement with respect to pure C_3N_4 ($\approx 2\,\mu mol\,g^{-1}\,h^{-1}$ – 0% MHP loading in Figure 2.15a). Irradiation of TEOA aqueous solution (no catalyst, blank control test) yielded just $0.014\,\mu mol\,h^{-1}$, confirming the key role of each catalyst.

Such 10-fold improvement for the composites HER is even more significant if considering that their surface area is, for example, at $33\%\,wt$ loading, $\frac{1}{7}$ of that of C_3N_4 (see Table 2.3) and that such parameter strongly affects the performances of heterogeneous photocatalysts (as a rough idea, in our previous experiments on C_3N_4, we demonstrated that a reduction of $\frac{1}{5}$ of the surface area correspond to about $\frac{1}{3}$ reduction of hydrogen photogeneration).[56] Moreover, this is an impressive value also considering the absence of any metal co-catalyst, which is usually employed with C_3N_4 and/or common semiconducting photocatalysts.

Optimal photocatalytic performance has been found at $33\%\,wt$ MHP. Further loading (e.g., $50\%\,wt$, data not shown) did not provide any enhancement in the HER, while a general reduction (below

Table 2.3. Surface area of C_3N_4 and C_3N_4/DMASnBr$_3$ composites at different percentages of MHP loading, the error was calculated as the standard deviation over three measures. Data have been reproduced from ref.[37]

	Specific Surface Area $\left(\frac{m^2}{g}\right)$
C_3N_4	26.4 (4)
C_3N_4/DMASnBr$_3$ 5% *wt*	8.5 (2)
C_3N_4/DMASnBr$_3$ 15% *wt*	5.0 (4)
C_3N_4/DMASnBr$_3$ 33% *wt*	3.4 (1)

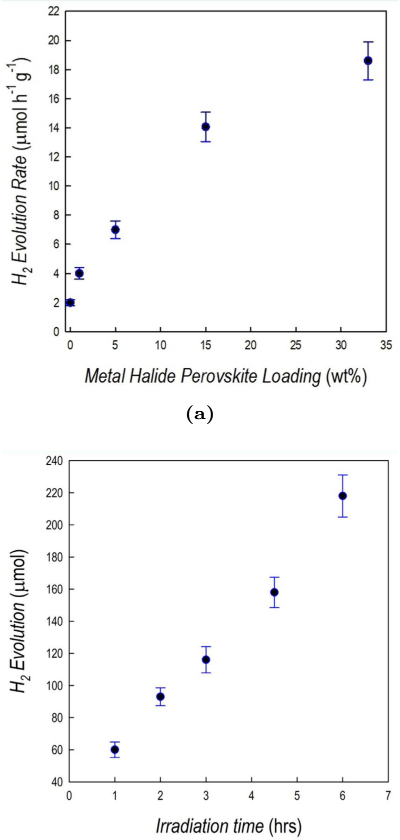

(a)

(b)

Figure 2.15. a) HERs for $C_3N_4/DMASnBr_3$ composites ($1\,g\,L^{-1}$) at different percentages of MHP loading, without any metal co-catalyst; b) hydrogen evolution profile over irradiation time for the $C_3N_4/DMASnBr_3$ $33\%\,wt$ composite, with $3\%\,wt$ Pt; $1\,g\,L^{-1}$ catalyst in $10\%\frac{V}{V}$ TEOA aqueous solution, under simulated solar light ($6h$ irradiation, Xenon lamp, $500\,W\,m^{-2}$, 300–800nm, IR-treated soda lime glass UV-outdoor filter). Reprinted with permission from ref.[37] Copyright 2021 Angewandte Chemie International Edition.

$\approx 14\, \mu mol\, g^{-1}\, h^{-1}$) was observed possibly due to covering of active sites and/or shielding of light absorption in C_3N_4.

To clarify the role of surface area and to provide comparable data, we performed an experiment with a lower amount of C_3N_4 ($0.13\, g\, L^{-1}$) which corresponds to approximately the same catalytic surface in suspension for $1\, g\, L^{-1}$ of C_3N_4/DMASnBr$_3$ 33% wt (see Table 2.3). Under these conditions, the irradiation test gave little H_2 ($0.5\, \mu mol\, g^{-1}\, h^{-1}$), far below the HER of the composite material (see Figure 2.15a).

Notably, there is a clear synergic role within the composite since, under the same experimental conditions, C_3N_4 produces $2\, \mu mol\, g^{-1}\, h^{-1}$ while DMASnBr$_3$ stands below $1\, \mu mol\, g^{-1}\, h^{-1}$.[43]

Photogeneration experiments have been further undertaken employing metallic Pt as co-catalyst (3% wt), to reproduce the common photocatalytic conditions used for carbon nitride-based composites.[13, 19, 22, 38, 39] Under these conditions, the C_3N_4/DMASnBr$_3$ with 33% wt MHP composite reached an impressive H_2 production of $1730\, \mu mol\, g^{-1}\, h^{-1}$ (apparent quantum yield, AQY 6.6%) that places it close to the materials with ultra-high HER.[45] Under these experimental conditions (i.e., with Pt co-catalyst), the synergic effect of the composite is especially evident, being the HER of C_3N_4 $620\, \mu mol\, g^{-1}\, h^{-1}$ (for a surface area 7-fold higher than the composite) and that of DMASnBr$_3$ around $6\, \mu mol\, g^{-1}\, h^{-1}$.[45]

The kinetics of H_2 evolution for the composite was also studied and the profile (Figure 2.15b) indicates substantially a linear increase of the production as a function of time.

For comparison with a benchmark catalyst, the well-known Evonik Aeroxide P25 TiO_2 (10–50nm, $60.8\, m^2\, g^{-1}$) was tested ($1\, g\, L^{-1}$, 10% $\frac{V}{V}$ TEOA, 6h irradiation). Despite its 15-folds higher surface area, the commercial semiconductor gave HERs of 155 and $6970\, \mu mol\, g^{-1}\, h^{-1}$, without and with 3% wt Pt respectively, further corroborating the above argument.

To assess the effect of the sacrificial agent, the 33% wt MHP composite was tested also in pure water, obtaining a hydrogen production of $14\, \mu mol\, g^{-1}\, h^{-1}$ ($7\, \mu mol\, g^{-1}\, h^{-1}$ with no metal co-catalyst, to be compared with a H_2 production $< 0.1\, \mu mol\, g^{-1}\, h^{-1}$ of C_3N_4 alone, see Table 2.4).

A final test to prove the effectiveness of C_3N_4/DMASnBr$_3$

Table 2.4. HERs for C_3N_4 and $C_3N_4/DMASnBr_3$ composites at different percentages of MHP loading as well as for $C_3N_4/DMASnBr_3$ 33% *wt* under different photocatalysis test conditions. RSD $< 10\%$ ($n = 3$). Data reproduced from ref.[37]

Catalyst	**Experimental Conditions**	**HER** ($\boldsymbol{\mu mol\, g^{-1}\, h^{-1}}$)
C_3N_4	pure water, no Pt	< 0.1
C_3N_4	$10\%^V/_V$ TEOA, no Pt	2.0
$C_3N_4/DMASnBr_3$ 1% *wt*	$10\%^V/_V$ TEOA, no Pt	4.0
$C_3N_4/DMASnBr_3$ 5% *wt*	$10\%^V/_V$ TEOA, no Pt	7.0
$C_3N_4/DMASnBr_3$ 15% *wt*	$10\%^V/_V$ TEOA, no Pt	14.1
$C_3N_4/DMASnBr_3$ 33% *wt*	$10\%^V/_V$ TEOA, no Pt	18.6
$C_3N_4/DMASnBr_3$ 33% *wt*	pure water, no Pt	7.0
$C_3N_4/DMASnBr_3$ 33% *wt*	pure water, 3% *wt* Pt	14.0
C_3N_4	$10\%^V/_V$ TEOA, 3% *wt* Pt	620
$DMASnBr_3$	$10\%^V/_V$ TEOA, 3% *wt* Pt	6
$C_3N_4/DMASnBr_3$ 33% *wt*	$10\%^V/_V$ TEOA, 3% *wt* Pt	1730
C_3N_4	$0.1M$ aqueous glucose, no Pt	< 0.4
C_3N_4	$0.1M$ aqueous glucose, 3% *wt* Pt	3
$C_3N_4/DMASnBr_3$ 33% *wt*	$0.1M$ aqueous glucose, no Pt	8
$C_3N_4/DMASnBr_3$ 33% *wt*	$0.1M$ aqueous glucose, 3% *wt* Pt	300

($33\%\, wt$) is to test its photogeneration activity in $0.1M$ aqueous glucose, representative of a biomass-derived sacrificial agent. The HER activity for C_3N_4/DMASnBr$_3$, with $3\%\, wt$ Pt, was $300\, \mu mol\, g^{-1}\, h^{-1}$ (AQY 1.1%) while that of C_3N_4 was $3\, \mu mol\, g^{-1}\, h^{-1}$, resulting in an impressive 100-fold improvement. Meanwhile in absence of Pt, the composite produced $8\, \mu mol\, g^{-1}\, h^{-1}$ of hydrogen gas while carbon nitride alone resulted in not quantifiable HER ($< 0.4\, \mu mol\, g^{-1}\, h^{-1}$). In the absence of any catalyst, irradiation of glucose solution yielded not quantifiable HER ($< 0.01\, \mu mol\, h^{-1}$). A summary of the HERs for different composite compositions and photogeneration conditions is reported in Table 2.4.

These results can be interpreted by considering the alignment of the relevant energy levels at the semiconductor-water interface. We employed advanced electronic-structure calculations to align the band edges of DMASnBr$_3$ and C_3N_4 with respect to a computational standard hydrogen electrode via the vacuum level.[57, 58]

The results depicted in Figure 2.16 show that valence and conduction band edges of DMASnBr$_3$ and C_3N_4 are placed at 6.5 and $3.65\, eV$ below the vacuum level, respectively (values referred to RHE: 6.0 and $3.3\, eV$ respectively).

Being both materials absorbers in the visible region, the achieved alignment implies that excited electrons in the conduction band of C_3N_4 can be effectively transferred to the perovskite, and similarly, holes in the valence band of DMASnBr$_3$ can migrate to the C_3N_4. Overall, this alignment results in an efficient separation and transport of photo-induced electrons and holes, which is likely to drastically hinder charge recombination.

Furthermore, since the rate of non-adiabatic charge transfer shows an inverse exponential dependence on the energy difference between initial and final state, the lower energy difference between the conduction band edge of DMASnBr$_3$ and the H^+/H_2 produces a kinetically more favourable alignment.[59] We notice that, for the same reason, the alignment between the valence band of C_3N_4 and the TEOA/TEOA$^+$ redox level (Figure 2.16) would be particularly beneficial for the oxidation reaction.

Overall, the mechanism of hydrogen photogeneration reaction in this novel composite provides an efficient charge separation and improved photocatalysis.[46]

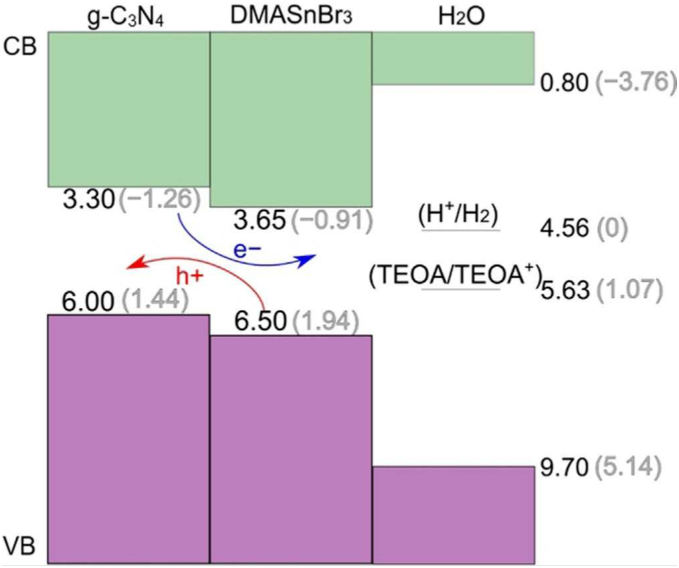

Figure 2.16. VB and CB edges of C_3N_4 and $DMASnBr_3$ aligned with the band edges of liquid water and with the H^+/H_2 and TEOA/TEOA$^+$ redox level (cf. ref.[60]) through the vacuum level. Values are referred to the vacuum level (black) and to the RHE (grey) using the computational alignment achieved in ref.[58] All values are given in eV. Reprinted with permission from ref.[37] Copyright 2021 Angewandte Chemie International Edition.

Conclusions

In summary, we reported solid evidence of water stability of $DMASnBr_3$ perovskite. Such properties have been exploited in the design and realization of a new class of photocatalytic composites based on the coupling between C_3N_4 and $DMASnBr_3$, showing promising catalytic properties in aqueous solutions under simulated solar light. The results show an effective synergic role between the perovskite and the carbon nitride deriving from a beneficial band alignment as demonstrated by DFT calculations.

These preliminary results pave the way to the realization of a new class of photocatalysts which couple the efficient optical absorption and carrier lifetime properties of MHPs with the well-known photocatalytic activity of carbon nitride.

PEA_2SnBr_4

PEA_2SnBr_4: a Water-Stable Lead-Free Two-Dimensional Perovskite and Demonstration of its Use as a Co-Catalyst in Hydrogen Photogeneration and Organic-Dye Degradation[61]

Purpose

In this work we report the development of a novel lead-free 2D material, namely phenylethylammonium tin bromide PEA_2SnBr_4, that shows impressive water-resistance by retaining its original crystal structure and optical properties when placed in contact with water.

Such properties have been advantageously used for the fabrication of a co-catalytic system by coupling with graphitic carbon nitride. C_3N_4/PEA_2SnBr_4 composites at different metal halide perovskite loadings (5 and $15\%\,wt$) have been prepared and tested in hydrogen photogeneration in an aqueous environment and organic dye degradation (Methylene Blue, MB).

Introduction

The poor water stability of 3D MHPs is a major concern, and it limits their application in solar cell technology and optoelectronic devices.[62–66] Such an issue can be overcome by using 2D layered perovskite derivatives of the general formula $R_2(CH_3NH_3)_{n-1}B_nX_{3n+1}$, where n represents the number of inorganic layers; R represents a large organic cation, for example $C_6H_5(CH_2)_2NH_3^+$ (PEA^+); B represents a metal cation and X represents a halide. The improved moisture resistance of 2D MHP derivatives comes from the presence of the hydrophobic R groups occupying the surface sites and protecting the inorganic layers from water.[62]

To date, several examples of the use of 2D protecting layers in perovskite solar cells with a 2D/3D architecture have been reported.[63–71] On the other hand, the optical properties of MHP could be used to explore their application in other fields, such as photocatalysis.

In this respect, some examples of hydrogen photogeneration by metal halide perovskites have been reported in the current literature, where, due to the inherent water instability of MHPs, the use of concentrated solutions of halo acids (such as HI) was required to avoid decomposition.[17, 19, 40, 41, 43] We have recently shown that it is possible to achieve an improved stability of a selected 3D lead-free MHP (namely $DMASnBr_3$) in water where, possibly, the hydrophobic organic group protects the perovskite from both water and tin oxidation, as recently also found by computational modelling.[43, 72]

In order to envisage novel applications of MHPs and their derivatives, in the photocatalysis field, we have devised a novel 2D lead-free MHP derivative that could meet the prerequisites of water stability and suitable optical properties for co-catalysis. PEA_2SnBr_4 allowed us to achieve these goals, showing an exceptional water stability that was exploited in the preparation of novel co-catalysts with graphitic carbon nitride (C_3N_4).

Experimental Methods and Discussion

PEA_2SnBr_4 was synthesized by a wet-chemistry route (by precipitation from a stoichiometric solution of the halogen precursors, that was evaporated until dry) in the form of bulk material and its XRD pattern is shown in Figure 2.17a. The crystal structure agrees with the orthorhombic *Cmca* space group symmetry that was defined for the BZA_2SnBr_4 material, and the pattern is dominated by (h00) reflections, a typical feature of 2D layered materials.[73] Before preparing the final catalyst, the water stability of the perovskite was tested in two ways:

- by dispersing the powders in distilled water under stirring and

recovering them by filtration,
- by measuring the amount of tin in DW after powder removal.

Figure 2.17a also shows the XRD pattern of PEA_2SnBr_4 after $4\,h$ in DW under stirring, which is superimposable onto that of the starting material, thus confirming that it does not dissolve in water. A further comparison of the two patterns is shown in Figure 2.17b as the square root of the intensity, in order to possibly put in prominence a very low amount of impurities. Moreover, the leaching test showed that just $0.14\%\,wt$ of the initial amount of tin in the material is released in water after $4\,h$ stirring, confirming the water-stability.

The UV-Vis absorbance spectra of the perovskite before (as-prepared) and after water dispersion are shown in Figure 2.17c and again the absorption edge remains fixed at $2.67\,eV$ without the appearance of any absorption tail. This aspect is of particular importance, since the defect state associated with Sn^{2+} to Sn^{4+} oxidation is well known to cause a significant change in the optical properties of the MHPs and their derivatives.[74]

Finally, the strongest proof of water stability comes from the results of XPS analysis. Figure 2.17d shows the Sn $3d$ XPS spectra of the as-prepared PEA_2SnBr_4 and that after $4\,h$ in DW under stirring. The binding energies correspond to those of Sn^{2+} ($487.6\,eV$), and as can be seen, the two spectra are superimposable in terms of both the position and the shape, confirming the water-stability of PEA_2SnBr_4 and the absence of oxidation.[50]

We remark that a very recent computational modelling work indicated that the presence of PEA^+ hydrophobic groups not only protects the inorganic layer from water but also protects tin from oxidation.[72] It may be possible that the presence of long and hydrophobic organic groups directly linked to the single inorganic slab creates a close and water-repellent environment that protects it both from moisture and in turn from oxidation.

After having assessed the optimal water-stability of PEA_2SnBr_4, we prepared composite catalytic systems by coupling this 2D lead-free perovskite, as a co-catalyst, to C_3N_4. This strategy is commonly used to improve the properties of C_3N_4, to increase charge migration and the recombination time, and to extend the absorption range.[46,47] As was observed for $DMASnBr_3$,[37] the band-gap of PEA_2SnBr_4 (around $2.67\,eV$) matches well with that of C_3N_4 ($2.72\,eV$), thus suggesting a possible synergic effect between the two materials.

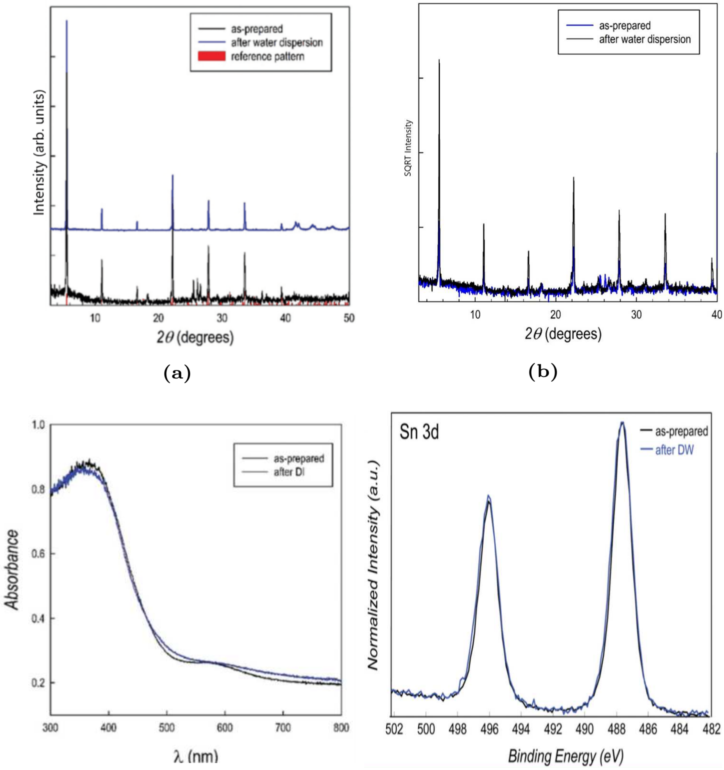

(a) **(b)**

(c) **(d)**

Figure 2.17. a,b) XRD pattern (respectively linear intensity and square root of intensity) of the as-prepared PEA_2SnBr_4 and after recovery from DW, the red vertical bars represent the reflections of the orthorhombic structure of the perovskite; c) UV-Vis spectra of the as-prepared PEA_2SnBr_4 and after recovery from DW; c) Sn 3*d* XPS spectra of the as-synthesized PEA_2SnBr_4 and after recovery from aqueous solution. Reprinted with permission from ref.[61] Copyright 2020 Journal of Materials Chemistry C.

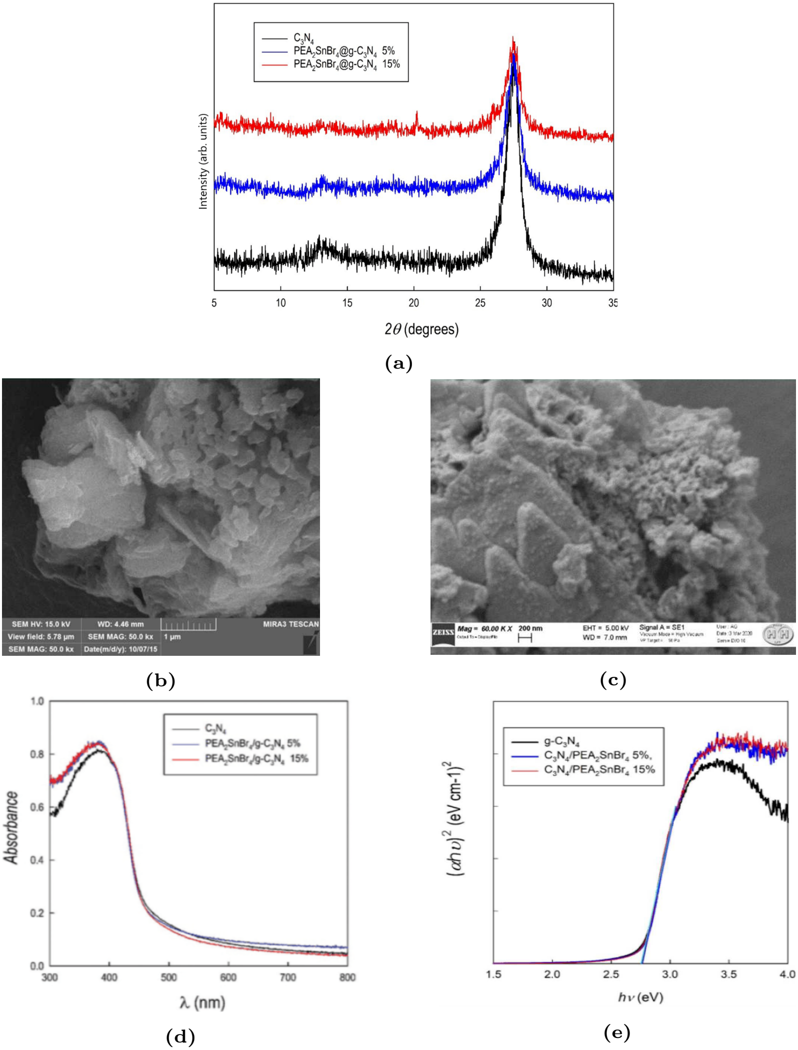

Figure 2.18. a) XRD patterns of pure C_3N_4 and C_3N_4/PEA_2SnBr_4 composites at different percentages of co-catalyst loading; b,c) Representative SEM images collected respectively on pristine C_3N_4 and C_3N_4/PEA_2SnBr_4 composite (15% *wt*). Reprinted with permission from ref;[61] d) UV-Vis spectra of pristine C_3N_4 and C_3N_4/PEA_2SnBr_4 composites; e) Tauc plots of pure C_3N_4 and C_3N_4/PEA_2SnBr_4 composites at different percentages of co-catalyst loading. Copyright 2020 Journal of Materials Chemistry C.

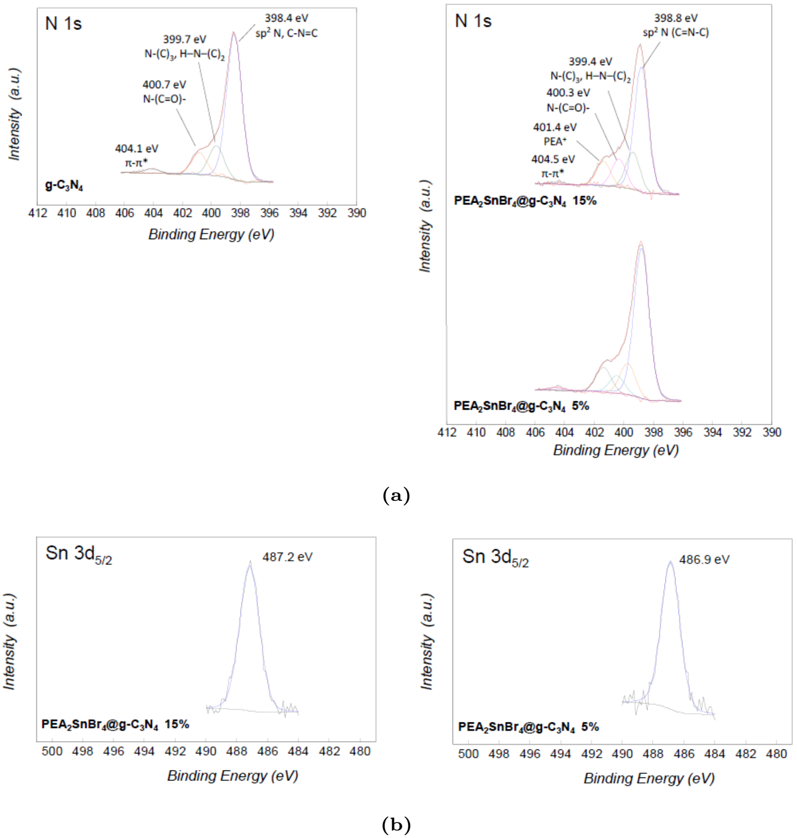

(a)

(b)

Figure 2.19. a) XPS N 1*s* spectra of the pristine C_3N_4 and of the C_3N_4/PEA_2SnBr_4 composites, the experimental spectra are shown in black, while each contribution is depicted with different colors, and the global fit is shown in red; b) XPS Sn $3d_{5/2}$ spectra of the C_3N_4/PEA_2SnBr_4 composites. Reprinted with permission from ref.[61] Copyright 2020 Journal of Materials Chemistry C.

C_3N_4/PEA_2SnBr_4 composites at different co-catalyst loadings (5 and 15% *wt*) were synthesized by a wet-chemistry route and their crystal structures were characterized by using XRD (Figure 2.18a). The composites reveal an overall amorphous-like structure, with the main peak of C_3N_4 (around 27.51°) and the general sample scattering becoming progressively less intense with the increasing amount of co-catalyst. No clear diffraction peaks of crystalline PEA_2SnBr_4 were found in the patterns, suggesting that this can be due the presence of C_3N_4 during the synthesis which tends to reduce the structural order of PEA_2SnBr_4, and/or to the formation of small particles on carbon nitride, as revealed by the significant change of morphology passing from pristine C_3N_4 to the composite (Figures 2.18b-2.18c).

EDS analysis of the composites (the data of which are reported in Table 2.5) confirmed the good accordance of the Sn/Br ratio with the expected value, ruling out the formation of different phases and/or clusters.

The XPS spectra of N 1*s* (Figure 2.19a) confirmed the presence of quaternary ammonium around 401.4 *eV* in both composites, which is absent in pristine carbon nitride.[51,52] Also, the Sn 3*d* XPS spectra of both composites (Figure 2.19b) show analogous signals to the starting PEA_2SnBr_4 with a slight shift to lower binding energies (less than 1 *eV*), which rules out oxidation during composite preparation (Sn^{4+} would appear at higher binding energies than Sn^{2+}). The origin of this shift goes beyond the scope of the present paper and may be related to the interaction between the perovskite and C_3N_4 as well as to the peculiar morphology of the composites.

The UV-Vis absorbance spectra of the C_3N_4/PEA_2SnBr_4 composites (Figure 2.18d) show the expected predominance of the C_3N_4 feature for both 5 and 15% *wt* loadings, by keeping the absorbance threshold around 2.72 *eV* (see the Tauc plots in Figure 2.18e). This

Table 2.5. Elemental composition of composite samples probed by EDS. Data reproduced from ref.[61]

	Experimental Br/Sn Ratio		
PEA_2SnBr_4/C_3N_4 5% *wt*	3.79	4.04	3.91
PEA_2SnBr_4/C_3N_4 15% *wt*	4.02	4.01	3.96

result could also be anticipated considering the relatively small difference in the band gap between carbon nitride and PEA_2SnBr_4.

Once pure PEA_2SnBr_4 and the composites were characterized, we focused on the evaluation of their photocatalytic properties, by looking at hydrogen photogeneration from water and the degradation of model organic water pollutants, by employing common protocols used for similar C_3N_4-based composites.[75] The results reported have been obtained on several replicas of the composites.

Firstly, the hydrogen photogeneration efficiency of the C_3N_4/PEA_2SnBr_4 composites has been determined in water containing $10\%\frac{V}{V}$ TEOA, as a typical sacrificial agent, and with a $3\%\,wt$ Pt loading. The HERs as a function of co-catalyst loading of the composites are reported in Table 2.6.

From the data reported in Table 2.6, it is possible to make several observations:

- hydrogen production ($4\,\mu mol\,g^{-1}\,h^{-1}$) is achieved by the perovskite alone;
- C_3N_4 shows a significant HER of $81\,\mu mol\,g^{-1}\,h^{-1}$;
- a synergic effect is observed for both composites, providing HERs that are more than 20 and 10 times that of pure carbon nitride, for the co-catalyst loadings of 5 and $15\%\,wt$, respectively;
- a HER of about $1600\,\mu mol\,g^{-1}\,h^{-1}$ for the C_3N_4/PEA_2SnBr_4 $5\%\,wt$ composite places it close to that of materials with an ultra-high HER.[75]

Table 2.6. HERs from aqueous solutions for C_3N_4 and C_3N_4/PEA_2SnBr_4 composites at different percentages of MHP derivative loadings as well as for PEA_2SnBr_4 ($1\,g\,L^{-1}$ catalyst, $3\%\,wt$ Pt, $6\,h$ irradiation under simulated solar light, $500\,W\,m^{-2}$). ($RSD \leq 10\%$, $n = 3$). Data reproduced from ref.[61]

	HER $(\mu mol\,g^{-1}\,h^{-1})$	
	$10\%\frac{V}{V}$ TEOA	**$0.1\,M$ glucose**
PEA_2SnBr_4	4 (0.4)	< 0.1
C_3N_4/PEA_2SnBr_4 $5\%\,wt$	1613 (98)	107 (8)
C_3N_4/PEA_2SnBr_4 $15\%\,wt$	963 (59)	n.d.
C_3N_4	81 (6)	3 (0.3)

n.d. = not determined

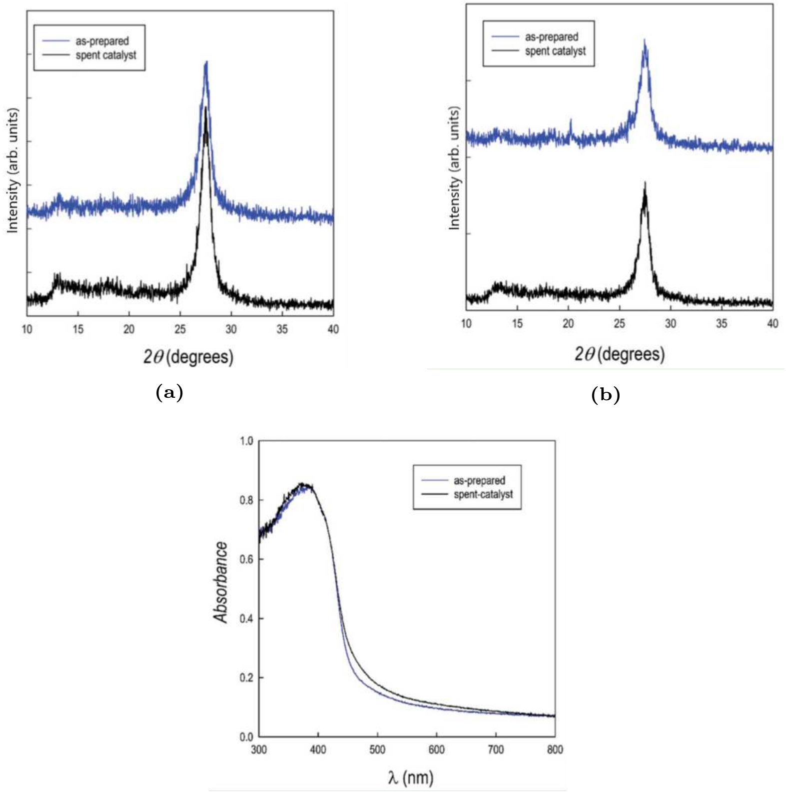

(a) **(b)**

(c)

Figure 2.20. a,b) XRD pattern of C_3N_4/PEA_2SnBr_4, respectively 5% *wt* and 15% *wt*, composite as-prepared and after the H_2 photogeneration experiment (spent catalyst); c) UV-Vis spectra of C_3N_4/PEA_2SnBr_4 5% *wt* composite as-prepared and after the H_2 photogeneration experiment (spent catalyst). Reprinted with permission from ref.[61] Copyright 2020 Journal of Materials Chemistry C.

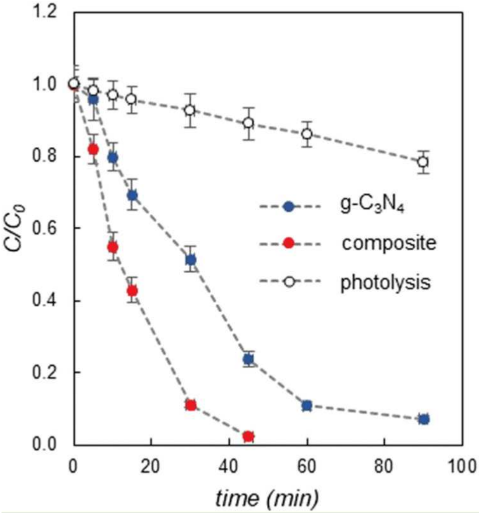

Figure 2.21. Variation of MB concentration as a function of irradiation time for C_3N_4 (blue dots) and C_3N_4/PEA_2SnBr_4 5% *wt* composite (red dots), compared to the photolysis effect (empty dots). Conditions: $1\,g\,L^{-1}$ catalyst, $250\,W\,m^{-2}$ simulated solar light. $RSD \leq 10\%$ $(n = 3)$. Reprinted with permission from ref.[61] Copyright 2020 Journal of Materials Chemistry C.

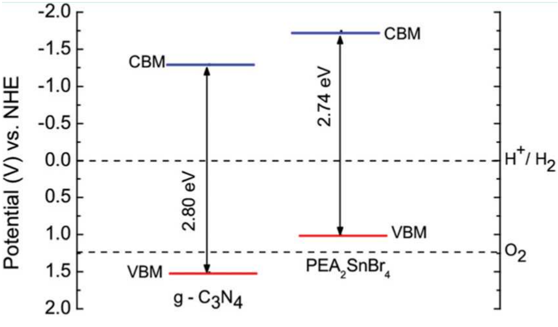

Figure 2.22. Calculated band edge positions (solid lines) for two semiconductors relative to RHE potential. The two dashed lines indicate the water redox reaction potentials. Reprinted with permission from ref.[61] Copyright 2020 Journal of Materials Chemistry C.

Table 2.6 also reports the photogeneration activity of C_3N_4/PEA_2SnBr_4 5% wt in 0.1 M aqueous glucose, representative of a biomass-derived sacrificial agent. The HER for the composite was 107 $\mu mol\, g^{-1}\, h^{-1}$ and showed a 30-fold improvement against that of pure C_3N_4 (3 $\mu mol\, g^{-1}\, h^{-1}$).

To check the stability of the C_3N_4/PEA_2SnBr_4 composites after the photogeneration reaction, the reaction suspension was filtered, and the powder was recovered and subjected to XRD and UV-Vis spectroscopy analyses. The patterns of the composites before and after the photocatalytic tests are shown in Figures 2.20a-2.20b, showing unaltered patterns of the spent catalysts compared to those of the starting material.

Moreover, compared to the as-prepared powder, the UV-vis spectra also remain unchanged for the spent catalyst (the spectra of the 5% wt sample are represented in Figure 2.20c).

The composite with a higher HER was also tested to check its activity towards the decomposition of organic dyes, by selecting MB as a representative model compound of this class. Figure 2.21 shows the variation of MB concentration (plotted as $\frac{C}{C_0}$, where C_0 is the initial concentration) as a function of irradiation time, compared to that of pure C_3N_4 and direct photolysis.

It emerged from the data reported in Figure 2.21 that the composite material also performs better than pure carbon nitride with respect to organic dye degradation. In particular, pristine C_3N_4 cannot completely degrade MB even after 90 min of irradiation, while the C_3N_4/PEA_2SnBr_4 5% wt composite completely decomposed the dye in about 40 min.

The particularly efficient performance of the C_3N_4/PEA_2SnBr_4 composite can be understood on the basis of the relative band- alignment of the two semiconductors when present in the composite.

The Valence Band Maximum (VBM) and Conduction Band Minimum (CBM) edge positions of C_3N_4 and PEA_2SnBr_4 relative to the RHE potential were calculated using the work function method:

$$E_{VBM} = -\Phi - 0.5E_g \tag{2.1}$$

$$E_{CBM} = -\Phi + 0.5E_g \tag{2.2}$$

$$E'_{CBM(VBM)} = -E_{CBM(VBM)} - 4.5 \tag{2.3}$$

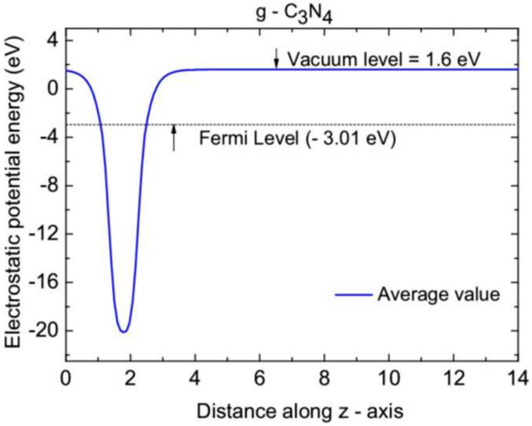

(a)

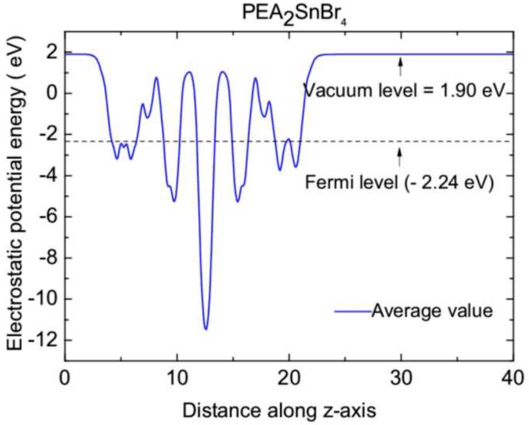

(b)

Figure 2.23. a) Electrostatic potential energy for C_3N_4 plotted along z-axis (Å) of unit cell; b) electrostatic potential energy for PEA_2SnBr_4 monolayer along z-axis (Å) . Reprinted with permission from ref.[61] Copyright 2020 Journal of Materials Chemistry C.

where Φ is the work function, defined as the minimum energy required to extract an electron from a material, and is equal to the energy difference between the Fermi level and the electrostatic potential energy in vacuum. Furthermore, E_g is the band gap and $E'_{CBM(VBM)}$ is the potential *vs.* RHE, and they are reported in Figure 2.22.[76, 77]

The calculated Φ values of C_3N_4 and PEA_2SnBr_4, obtained using the HSE06 functional (that is the hybrid functional approach proposed by Heyd, Scuzeria and Ernzerhof, that allows the calculation of the band gap of the material[78]), are $4.61\,eV$ (Figure 2.23a) and $4.14\,eV$ (Figure 2.23b), respectively. Notably, the calculated E_g values for the C_3N_4 ($2.8\,eV$) and PEA_2SnBr_4 ($2.74\,eV$) monolayers are in good agreement with the experimental values of $2.72\,eV$ and $2.67\,eV$, respectively.

As depicted in Figure 2.22 the CBMs of C_3N_4 and PEA_2SnBr_4 are located at $1.29\,V$ and $1.74\,V$ *vs.* RHE, which are above the H^+/H_2 potential, whereas the VBM of C_3N_4 is at $1.51\,V$ *vs.* RHE, below the O_2 potential.

Since the band gap values of both semiconductors are comparable, electron–hole pairs are generated in both the semiconductors under visible-light irradiation. Due to the band alignment shown in Figure 2.22, the photo-induced electrons from PEA_2SnBr_4 can easily move towards C_3N_4 due to the CBM lying at a less negative potential. Finally, the accumulated electrons take part in the photochemical reduction of water to generate hydrogen. In this way, the hetero-junction formed could limit the recombination rate of the photo generated electron–hole pairs, thus remarkably increasing the photocatalytic activity for hydrogen evolution compared to that of pure C_3N_4.

Conclusions

A novel 2D lead-free MHP derivative, PEA_2SnBr_4, has been synthesized and characterized, showing an impressive water-resistance in both structural and optical properties.

Such features have been exploited in the preparation of novel cocatalytic systems by coupling PEA_2SnBr_4 with C_3N_4 due to the close band-gap of the two semiconductors. The composites synthesized showed a synergic effect in the enhancement of photocatalytic hydrogen production in aqueous environment as well as in the degradation of organic dyes, without any degradation observed in the spent catalyst.

Computational modelling provides a description of the favourable band-alignment between PEA_2SnBr_4 and C_3N_4, thus confirming the synergic role from a microscopic point of view.

Additional Study on $DMASnBr_2$ and PEA_2SnBr_4

Additional study on the photocatalytic performance of $DMASnBr_3$ and PEA_2SnBr_4 was per formed in collaboration with the research groups of Professors Profumo[79] and Quadrelli,[80] of the University of Pavia, who took care, respectively, of the chemometric study and statistical treatment of the data, and of the considerations on the organic reactions that were performed.

Carbon Nitride-Perovskite Composites: Evaluation and Optimization of Photocatalytic Hydrogen Evolution in Saccharides Aqueous Solution[79]

Purpose

In this work we deepened the study of biomass-promoted hydrogen photo-generation involving hybrid photocatalysts, namely $C_3N_4/DMASnBr_3$ and C_3N_4/PEA_2SnBr_4.

The composites were tested and compared in terms of HER, using Pt as a reference co-catalyst, and glucose as a representative sacrificial biomass. The conditions were optimized to maximize H_2 generation by a design of experiments involving catalyst amount, glucose concentration and Pt loading. Under optimized conditions, $C_3N_4/DMASnBr_3$ showed a 5-fold higher HER compared to C_3N_4/PEA_2SnBr_4. Encouraging results were also collected by explorative tests on raw starch solution.

Introduction

The search for new photocatalytic systems working under solar light for hydrogen production is increasingly triggering the interest of the scientific community.

In the framework of novel photocatalysts, graphitic carbon nitride has emerged in the last decade as one of the most promising material to run H_2 photoproduction from water under visible light, due to cost-effective and easy synthesis, chemical stability, narrow band-gap and band potentials suitable to perform relevant redox reactions in aqueous solution.[81,82] Its intrinsic limitations, namely, relatively high charge carriers recombination, low surface area and restricted light harvesting in the visible region, have been in part compensated by several strategies. For instance, metal and non-metal doping, structural and morphological modifications, dye-sensitization, and combination with co-catalysts of different nature (e.g., carbon nanotubes, carbon dots, metallic nanoparticles) have proved to be rewarding in terms of enhanced photocatalytic activity towards H_2 generation from water also in the presence of sacrificial agents.[82,83] Among these, mainly fine chemicals have been used, as recently reviewed by Nasir et al.,[82] while just a few studies were undertaken in aqueous biomass solutions or directly in wastewaters.[84–86]

In recent times, the application of MHPs and their derivatives in the photocatalysis field has aroused great interest in view of the relatively narrow band gaps compared to traditional metal oxide photocatalysts.[12,13] MHPs possess exclusive optical properties, such as consistent light absorption in the visible region, tuneable band gap and extended carriers lifetimes, conveniently exploited in photovoltaics and optoelectronics.[22]

Recently, coupling MHPs with C_3N_4 has become a cutting-edge research field,[82,87,88] although limited work has been done so far concerning photocatalysis.[82] Recently, lead-free MHPs and MHP derivatives showing an exceptional stability in water were synthesized and characterized,[37,43,61] thus opening a new avenue for the preparation and application of innovative photocatalysts.

In this context, our group advantageously coupled DMA and PEA-based materials, $DMASnBr_3$ and PEA_2SnBr_4, respectively, to C_3N_4, providing new micron-sized composites with excellent photocatalytic properties towards H_2 production from TEOA aqueous solution. In particular, up to a 20-fold increase of HER was achieved compared to C_3N_4 alone, due to a synergistic effect between the two constituents in the composite,[37,61] essentially due to improved charge carrier separation.

Such an effect results from the positive band-alignment between the two semiconductors and the co-catalyst was selected based on its band gap to exploit this synergistic effect. It was also observed in an explorative test that such catalytic systems can generate H_2 from glucose solution under UV-Vis light, with HERs from 30 to 100 times higher relative to pristine C_3N_4.[37, 61]

In this study, the two best performing materials we previously identified, namely C_3N_4/PEA_2SnBr_4 5% and C_3N_4/$DMASnBr_3$ 33%, were systematically tested, under simulated solar light, in aqueous glucose through a Design of Experiments (DOE) with the aim to maximize HER and compare the performance of each photocatalyst under the best conditions. The most performant composite was further investigated for its photochemical stability by recycling tests, compared to the well-known Evonik Aeroxide® P25 TiO_2, used without any metal co-catalyst, and in the presence of soluble starch as a low-cost and abundant polysaccharide.

Experimental Methods and Discussion

Based on the preliminary findings obtained with carbon nitride composites in TEOA solution,[37, 61] the two best performing materials, C_3N_4/$DMASnBr_3$ 33% and 5% C_3N_4/PEA_2SnBr_4, are investigated here for a systematic study of H_2 photoproduction from glucose aqueous solution.

Glucose was selected as a biomass-derived sacrificial agent because in the wastewaters from food industry sugars are present at considerable amounts,[84, 85] and Pt was used as the reference metal co-catalyst because of its excellent properties for water reduction due to the large work function, resulting in a strong Schottky barrier effect.[89, 90]

With the aim of investigating the behaviour of the two catalysts and maximizing H_2 evolution, a chemometric approach was chosen to easily individuate the effects of the key operational parameters of heterogeneous photocatalysis, namely the relative amounts of catalyst, glucose, and metal.[91–94] Accordingly, a full 2^3 experimental design was setup considering glucose concentration (x_1), catalyst amount (x_2) and Pt loading (x_3). As reported in Table 2.7, the experimental domain was comprised of two levels (-1 and $+1$) of each variable.

HERs obtained under the different conditions (mean values of duplicate tests), according to the experimental matrix, are reported in Table 2.8.

The values were used as the experimental response (y), and they were modelled (using the MATLAB® software) relative to each variable (x_i), in line with the following equation:

$$y = b_0 + b_1x_1 + b_2x_2 + b_3x_3 + b_{12}x_1x_2 +_{b_{13}} x_1x_3 + b_{23}x_2x_3 \quad (2.4)$$

Figure 2.24 shows the plot of the coefficients (b_i) of the model, while the response surfaces are gathered in Figure 2.25.

The models elaborated on the experimental results are:

$$HER = 390 + 99x_1 - 251x_2 - 64x_3 - 70x_1x_2 - 6x_1x_3 + 60x_2x_3 \quad (2.5)$$

$$HER = 101 + 15x_1 - 43x_2 - 41x_3 + 14x_1x_2 - 12x_1x_3 + 4x_2x_3 \quad (2.6)$$

for $C_3N_4/DMASnBr_3$ and C_3N_4/PEA_2SnBr_4, respectively.

As apparent from the significance of the coefficients (Figure 2.24), the picture is similar for both composites, as the three variables significantly affect the HER; in particular, the photoreaction is favoured by high glucose concentration and low levels of catalyst in the suspension and metal photo-deposited on the catalyst surface.

In addition, some interactions are statistically relevant, in particular x_1–x_2 and x_2–x_3 for $C_3N_4/DMASnBr_3$. In line with the response surfaces (see Figure 2.25), HER increases by keeping the catalyst amount at the low level but with the highest concentration of sacrificial agent, whereas both catalyst and co-catalyst at the lowest level enhance H_2 evolution.

For C_3N_4/PEA_2SnBr_4, x_1–x_2 and x_1–x_3 are significative, accordingly, the response surfaces show that also in this case, HER is maximized with low Pt loading and catalyst amount, and the high level

Table 2.7. Experimental domain for the 2^3 factorial design. Data have been reproduced from ref.[79]

Variable	**Level Codes**	
	−1	**+1**
x_1 : glucose concentration (M)	0.025	0.2
x_2 : catalyst amount ($g\,L^{-1}$)	0.5	2
x_3 : Pt loading ($\%\,wt$)	0.5	3

Table 2.8. Mean HERs obtained in the conditions of the experimental plan for both composite photocatalysts. Data have been reproduced from ref.[79]

entry	**1**	**2**	**3**	**4**	**5**	**6**	**7**	**8**
x_1 : glucose concentration (M)	0.2	0.025	0.2	0.025	0.2	0.025	0.2	0.025
x_2 : catalyst amount ($g\,L^{-1}$)	2	2	0.5	0.5	2	2	0.5	0.5
x_3 : Pt loading (% wt)	3	3	3	3	0.5	0.5	0.5	0.5
$DMASnBr_3$/ C_3N_4 HER ($\mu mol\,g^{-1}\,h^{-1}$)	143	128	696	341	194	92	925	606
PEA_2SnBr_4/ C_3N_4 HER ($\mu mol\,g^{-1}\,h^{-1}$)	27	14	99	100	147	43	191	188

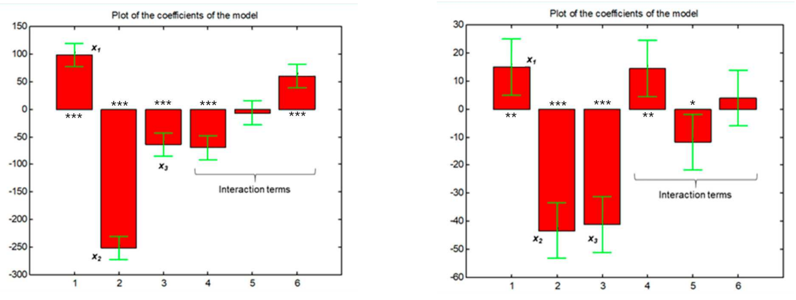

(a) **(b)**

Figure 2.24. Plots of the coefficients of the model for: a) $C_3N_4/DMASnBr_3$ and b) C_3N_4/PEA_2SnBr_4. " * " indicate the significance of the coefficients (*: $p < 0.05$, **: $p < 0.01$, ***: $p < 0.001$), while error bars indicate the confidence intervals ($p = 0.05$). Reprinted with permission from ref.[79] Copyright 2020 Catalysts.

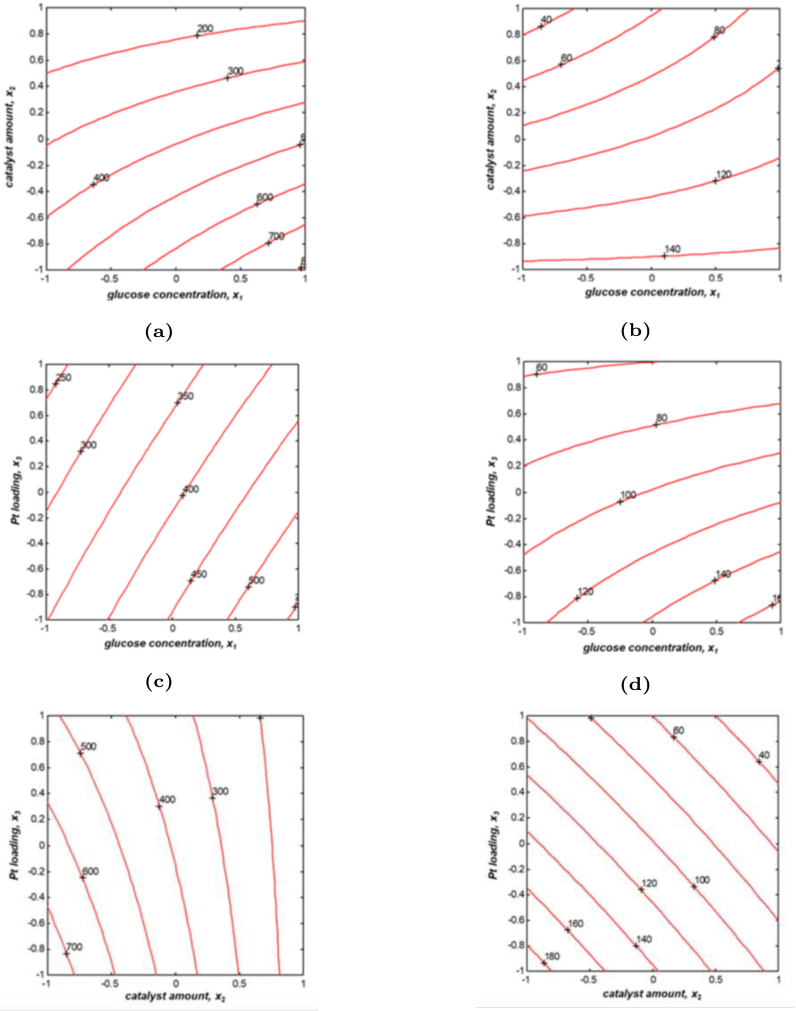

(a)

(b)

(c)

(d)

(e)

(f)

Figure 2.25. Response surfaces obtained by MATLAB® elaboration for: a,c,e) $C_3N_4/DMASnBr_3$ and b,d,f) C_3N_4/PEA_2SnBr_4 (for level codes −1, +1 see Table 2.7); the number close to each curve represents the HER. Reprinted with permission from ref.[79] Copyright 2020 Catalysts.

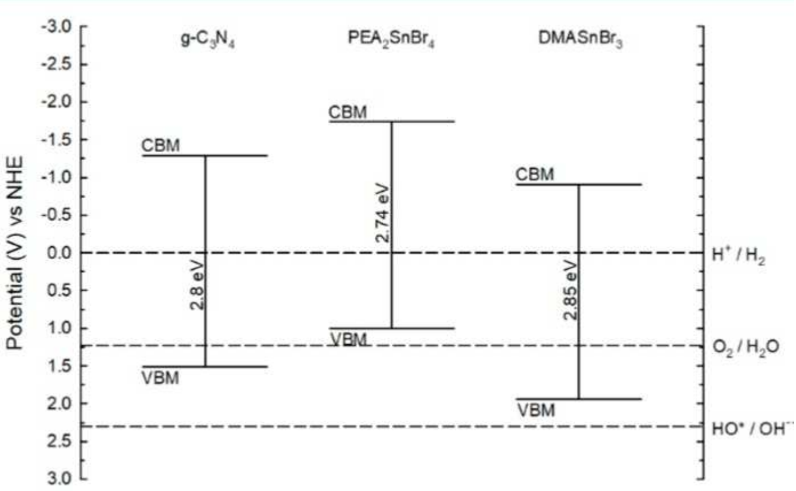

Figure 2.26. Scheme of the redox potentials (pH 7, vs RHE) of relevant reactions in relation to the band edges positions of as-prepared C_3N_4 and metal halide co-catalysts. Reprinted with permission from ref.[79] Copyright 2020 Catalysts.

Table 2.9. Key experiments for evaluating the photocatalytic system based on C_3N_4/DMASnBr3 33% (simulated solar light). Data have been reproduced from ref.[79]

Sample	**Solvent**	**HER** $\mu mol\, g^{-1}\, h^{-1}$
catalyst ($0.5\, g\, L^{-1}$)	water	12
catalyst ($0.5\, g\, L^{-1}$) + 0.5% wt Pt	water	62
catalyst ($0.5\, g\, L^{-1}$)	$0.2\, M$ glucose	142
catalyst ($0.5\, g\, L^{-1}$) + 0.5% wt Pt	$0.2\, M$ glucose	925
-	water	n.q.
-	$0.2\, M$ glucose	n.q.

n.q. = not quantified

of sacrificial biomass is useful, especially when working with $0.5\%\,wt$ Pt.

These findings can be explained considering that at low sacrificial agent concentration, the mass transfer of glucose from water to the catalyst surface is the bottleneck of photocatalytic reaction, whilst in concentrated solutions, interfacial reactions govern the process, due to the saturation of glucose on the catalyst.[91] Furthermore, excessive Pt loading reduces the catalytic surface available for light absorption; additionally, a high concentration of suspended powder causes scattering of the incident radiation, thus decreasing the overall process.[89, 92]

Based on these outcomes, the selected conditions were $0.2\,M$ glucose, $0.5\,g\,L^{-1}$ catalyst, and $0.5\%\,wt$ Pt. These are advantageous conditions, involving the use of small amounts of both catalyst and metal co-catalyst, and suggesting that large dilution of the reaction solution can be avoided when using food industry wastewaters, where the total sugar content is up to tens of grams per liter.[85]

The reproducibility was good, with RSD $\leq 11\%$ and $\leq 15\%$ observed on four independent experiments for C_3N_4/$DMASnBr_3$ and C_3N_4/PEA_2SnBr_4, correspondingly.

For the best performing composite, C_3N_4/$DMASnBr_3$, the optimal conditions were further confirmed by validation of the model, working at the test point ($x_1 = 0$; $x_2 = 0$; $x_3 = 0$). Being the mean HER ($407 \pm 69\,\mu mol\,g^{-1}\,h^{-1}$, $p = 0.05$, $n = 4$) not significantly different from the value predicted by Equation 2.4, namely $390\,\mu mol\,g^{-1}\,h^{-1}$, it is demonstrated that the model is effective, and it can be applied to the whole experimental domain.

The chemometric study provided key information. First, it enabled pointing out the most convenient conditions for H_2 evolution, which resulted in a three-fold increase in HER relative to the first pilot work;[61] at the same time, the results clearly highlight the superior photocatalytic activity of C_3N_4/$DMASnBr_3$.

Given the very small difference between the co-catalysts' band gaps, 2.85 and $2.74\,eV$ for $DMASnBr_3$ and PEA_2SnBr_4, respectively,[37, 61] and the higher surface area of C_3N_4/PEA_2SnBr_4 ($5.5\,m^2\,g^{-1}$ *vs.* $3.4\,m^2\,g^{-1}$ of C_3N_4/$DMASnBr_3$), it could be speculated that the better performance of the first catalyst derives from the different band alignments of the co-catalysts' VB and CB edges with those of carbon nitride (represented in Figure 2.26). This results in a different electron transfer and charge carriers' stabilization mechanism.

The synergistic effect between the two constituents of the $DMASnBr_3$-based photocatalyst has been explained in terms of favourable band alignment and prolonged charge carrier lifetimes.[61] In the case of PEA_2SnBr_4, this is also true, but it is known that 2D layered MHP derivatives have higher excitonic binding energies that may slightly reduce the charge carrier dynamics, thus affording a lower photocatalytic efficiency.[95]

Another reason rationally stands in the better dispersibility of the DMA composite in aqueous phase due to its lower hydrophobicity. Because of the low surface area of the composites, good mechanical stirring is important; on the other hand, the fast sedimentation of the powders can be an advantage to recover them from water after photocatalysis.

The photocatalytic behaviour of the composite containing the $DMASnBr_3$ perovskite was further studied. Table 2.9 summarizes the HERs collected by key tests aimed at assessing the role of the metal co-catalyst, of the glucose biomass and to evaluate the contribute of ”direct water splitting”, i.e., H_2 evolved from water in the absence of the sacrificial donor.[96]

As is apparent, the model biomass has a major role in sustaining H_2 evolution, which is 15-fold higher relative to the HER observed in neat water (the contribution of ”direct water splitting” is $< 7\%$). In addition, the metal co-catalyst largely rules the photoreaction to give gas phase H_2, both in the presence of the sacrificial agent and in pure water. Notice that appreciable HER was gained also with no metal, underlining the potentiality of such photoactive material. This evidence corroborates a photoreaction mechanism typical of the photocatalytic systems for H_2 production from water,[81, 83, 97] wherein:

- the catalyst absorbs the radiation generating the characteristic charge separation (holes and electrons);
- the sacrificial organic material serves as scavenger of the oxidizing species and, by undergoing gradual oxidation (photoreforming), supplies electrons;
- the metal works as an electron collector and is the active site for hydrogen ions reduction while hindering charge carriers' recombination and backward reactions.[83]

Regarding the $C_3N_4/DMASnBr_3$ composite, VB holes, not hydroxyl radicals, are generated in the solution and these trigger biomass oxidation to boost H_2 formation from water, while avoiding a complete aqueous phase reforming of the organic substrate until mineralization,[81] which instead occurs in titanium dioxide photocatalysis, especially with Pd co-catalyst.[90, 96, 98] The negligible H_2 evolution ($< 0.008\,\mu mol\,h^{-1}$) observed by irradiation of neat water and $0.2\,M$ glucose, as the control tests (Table 2.9), further substantiated the proposed mechanism.

The synergistic effect between carbon nitride and co-catalyst described above and assessed in foregoing work[37] was here confirmed in glucose solution under the best conditions. Indeed, HER was 74 and $40\,\mu mol\,g^{-1}\,h^{-1}$ for C_3N_4 and $DMASnBr_3$ individually tested, respectively, against $925\,\mu mol\,g^{-1}\,h^{-1}$ of the hybrid catalyst (see Table 2.9).

The values of Apparent Quantum Yield (AQY), calculated as the percent ratio $\frac{mol_{\mathrm{H_2}}}{mol_{\mathrm{incident\ photons}}}$,[85] and Turn Over Number (TON), calculated as the ratio $\frac{mol_{\mathrm{H_2}}}{mol_{\mathrm{Pt}}}$,[90] for $C_3N_4/DMASnBr_3$ in the optimized conditions are reported in Table 2.10.

These results are very interesting and highlight the efficiency of the composite catalyst that, despite the very low surface area ($< 4\,m^2\,g^{-1}$, 18-times lower than that of the commercial nanometric P25 TiO_2[99]), promoted HER equal to about one third of the latter ($2906\,\mu mol\,g^{-1}\,h^{-1}$), under the same conditions. To point out the role of surface area and to provide comparable data, we tested a lower amount of P25 TiO_2 ($0.028\,g\,L^{-1}$) to have approximately the same catalytic surface area of $0.5\,g\,L^{-1}$ of the composite. HER was $377\,\mu mol\,g^{-1}\,h^{-1}$, 2.5-times lower than that afforded by employing the composite.

Additional trials were devoted to investigating the stability of the

Table 2.10. AQY and TON values for $C_3N_4/DMASnBr_3$ ($0.5\,g\,L^{-1}$ catalyst, 0.5% *wt* Pt. Data have been reproduced from ref.[79]

Solvent	**AQY**	**TON**	**HER ($\mu mol\,g^{-1}\,h^{-1}$)**
distilled water	0.1	202	62
aqueous glucose	2.0	3007	925
aqueous starch	0.3	473	146

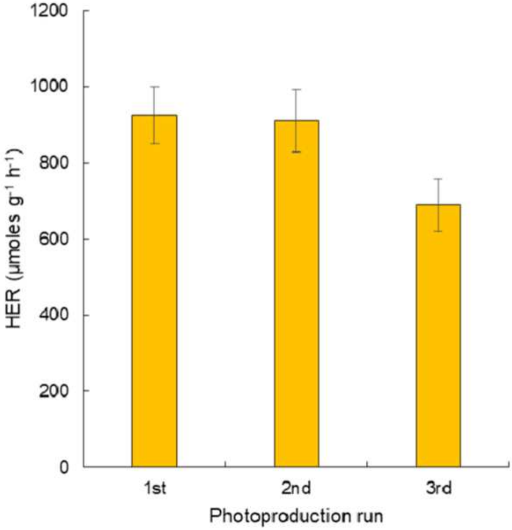

Figure 2.27. Reusability of C_3N_4/DMASnBr$_3$ ($0.5\,g\,L^{-1}$, $0.5\%\,wt$ Pt, $0.2\,M$ aqueous glucose), $RSD < 11\%$ ($n = 3$). Reprinted with permission from ref.[79] Copyright 2020 Catalysts.

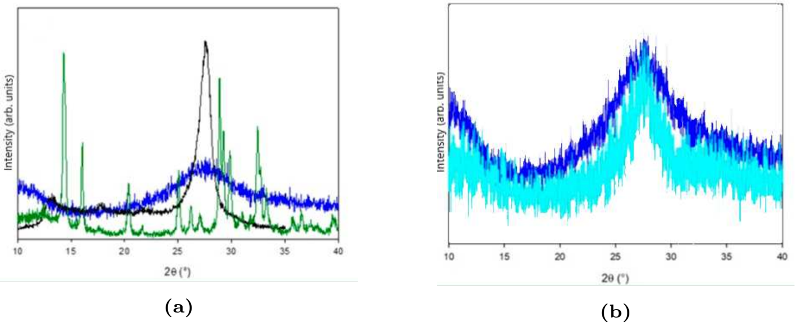

(a)

(b)

Figure 2.28. XRD patterns collected on: a) DMASnBr$_3$ (green), C_3N_4 (black) and as-prepared C_3N_4/DMASnBr$_3$ (blue); b) the composite after three irradiations (azure) compared to the as-prepared one (blue). Reprinted with permission from ref.[79] Copyright 2020 Catalysts.

catalyst upon subsequent irradiations. As is shown in Figure 2.27, no loss of efficiency was noticed using the recycled powder in a new sample solution, and only a 25% decrease in H_2 evolution in a third treatment.

The XRD profiles overlaid in Figure 2.28 attest the preservation of the pristine structure in the composite employed after the three sequential photoreactions (18 h total irradiation time) in aqueous glucose.

Although in the XRD pattern of the as-synthesized catalyst the peaks characteristic of the perovskite are not visible, a broad signal centred on the principal peak of the carbon nitride that stabilizes an amorphous structure of the perovskite is present, as previously discussed.[37] Superimposable patterns were observed on both fresh and recycled materials (see Figure 2.28b). These findings support both the integrity of the hybrid material and the maintenance of the perovskite in the photocatalyst. Thus, this can be utilized for at least three consecutive irradiations, as a proof of photo-chemical stability that strengthens the applicability of C_3N_4/DMASnBr$_3$ for a potential practical use.

Such new outcomes prompted us to test the composite in the presence of a polysaccharide sacrificial substance, and starch was chosen as the representative bio-polymer because of its low cost, large availability, and attractiveness as bio-oxygenated specie for H_2 photogeneration.[85, 98]

Hydrogen gas was effectively produced from starch solution (see Table 2.10), at a concentration of $4.5\,g\,L^{-1}$ (the maximum solubility[85]), although at lower amount compared to glucose. This is justified considering that that the rate of hydrogen evolution from water decreases with increasing molecular weights and structure complexity of carbohydrates.[89–91, 98] Additionally, since the VB holes are the oxidizing species of the present catalytic system, an intimate contact between the sacrificial substrate and the catalyst surface is certainly required. This could be more favoured with monosaccharides than polysaccharides with a branched skeleton such as starch, which realistically has slower mass transfer kinetics from solution to the composite surface sites.[90, 98]

Such new findings highlight that C_3N_4/DMASnBr$_3$ can carry forward H_2 photoproduction exploiting the sacrificial role of a raw polysaccharide such as soluble starch, which thus can be employed directly without any pre-treatment, e.g., enzymatic hydrolysis or microwave-assisted hydroxylation.[100, 101]

Conclusions

Lab-scale tests proved the superior photocatalytic activity of C_3N_4/DMASnBr$_3$ against C_3N_4/PEA$_2$SnBr$_4$ for H_2 evolution from glucose solution, under simulated solar light, using Pt as a co-catalyst.

The systematic optimization of the experimental conditions by a DOE provided HER higher than $900\,\mu mol\,g^{-1}\,h^{-1}$ using the former composite. The results herein collected highlight the importance to work under selected conditions to maximize the H_2 yield while reducing the use of catalyst and co-catalyst. The comparison with P25 TiO_2 strengthened the catalytic efficiency of C_3N_4/DMASnBr$_3$, while avoiding the handling of nano-sized powders. Notably, a rewarding H_2 formation (around $140\,\mu mol\,g^{-1}\,h^{-1}$) was gained, also avoiding any metal deposition.

C_3N_4/DMASnBr$_3$ showed good photochemical stability to be utilized for two consecutive runs without any loss of efficiency and with a decrease of 25% in the third cycle, as verified by H_2 evolution measurement and XRD analysis.

The system turned out to work also in raw starch solution as sustainable, model sacrificial biomass, providing ca. $150\,\mu mol\,g^{-1}\,h^{-1}$.

These outcomes corroborate the potential application of this new class of photocatalysts for clean energy retrieval under sustainable conditions and deserve further investigation to move the photoproduction experiments on sugar-rich wastewaters under natural solar light.

g-C_3N_4/Metal Halide Perovskite Composites as Photocatalysts for Singlet Oxygen Generation Processes for the Preparation of Various Oxidized Synthons[80]

Purpose

In this work g-C_3N_4/MHP and MHP derivative composites were prepared and used for the first time as photocatalysts for in situ $^1O_2$ generation to perform Hetero Diels–Alder (HDA), ene and oxidation reactions with suitable dienes and alkenes.

The standardized methodology was made applicable to a variety of olefinic substrates. The scope of the method is finely illustrated, and the reactions afforded desymmetrized hydroxy-ketone derivatives, unsaturated ketones, and epoxides.

Some limitations were also observed, especially in the case of the alkene oxidations, and poor chemoselectivity was somewhere observed in this work which is the first application of MHP-based composites for in situ $^1O_2$ generation. The experimental protocol can be used as a platform to further expand the knowledge and applicability of this kind of materials to organic reactions, since they offer a rich variety of tuning strategies which may be explored to improve reaction yields and selectivity.

Introduction

Singlet oxygen ($^1O_2$)[102–105] is a highly reactive and short-lived oxygen species and can undergo a variety of reactions; among them, the HDA [4+2] cycloadditions, the [2+2] cycloadditions, the ene reactions and epoxidations are representative of the most interesting ways to afford valuable synthons to be used in remarkable approaches toward organic molecules.[106–109] Photocatalysis uses light and pure oxygen to insert oxygenated functionalities on a carbon skeleton, avoiding the use of, in some cases, extremely toxic heavy metal catalysts; for these and other reasons, photocatalysis is an intrinsically environmentally friendly methodology.

$^1O_2$ is photochemically produced by the use of organic molecules (sensitizers)[110] or, alternatively, through classical hydrogen peroxide decomposition promoted by hypochlorite or hypobromite and ozonide decomposition. Moreover, $^1O_2$ can also be obtained by thermal decomposition of unstable molecules, such as arene endoperoxides, or by photolysis of oxone.[111] These methodologies are not devoid of problems due essentially to the instability of the organic sensitizers or not completely applicable to the experimental conditions required by specific syntheses. For these reasons, the modern chemical literature on $^1O_2$ reports the photochemical properties of new catalytic systems that proved to be nicely applicable to the generation of such transient oxygen species.

For example, the use of a Pd-conjoined metal-square with encapsulated fullerenes produces an efficient and photochemically stable $^1O_2$ photosensitizer. The metal-cage with the encapsulated fullerenes can oxidize a series of cyclic and acyclic alkenes at room temperature via visible light. These reactions take advantage of the excellent spin-converting properties of fullerenes, which makes them excellent agents for $^1O_2$ production.[112]

The need for oxygen-containing heterocycles or simply oxidized organic synthons is a continuous growing task in organic synthesis.[113] A range of products was obtained from the photo-oxidation of cyclopentadiene from photochemically generated $^1O_2$ using carbon dioxide as a solvent and 5,10,15,20-tetrakis(pentafluorophenyl) porphyrin as a CO_2-soluble photosensitizer. The endoperoxide intermediate was transformed into one of several different products in good yield depending on the conditions applied and by adding different reactors and reagents downstream of the photo-reactor, allowing the reaction products to be switched in one streamlined process. Quite remarkably, quenching with thiourea yielded the *syn*-diol, (1R,3S)-cyclopent-4-ene-1,3-diol, a valuable synthon for a variety of natural products. Treatment with an acid or a base afforded furfuryl alcohol and 4-hydroxy-2-cyclopentenone, respectively. High productivities for all products were obtained when compared to traditional batch reactions.[114, 115]

Moreover, continuous flow photooxidation of several conjugated dienes and subsequent rearrangement were engineered, involving endoperoxidation, Kornblum–DeLaMare rearrangement, and additional rearrangements to obtain useful hydroxyenones, furans, and 1,4-dicarbonyl building blocks.[109]

In this panorama, recently, we entered this challenging competition for $^1O_2$ generation easy methods by proposing the catalytic use of oxidized graphitic carbon nitride (g-C_3N_4) for $^1O_2$ generation under photochemical conditions. Some HDA and ene reactions were conducted on selected dienes and alkenes showing a general ability of oxidized g-C_3N_4 to promote chemoselective and unselective oxidative processes with strong dependence on substrate nature. The results offer a good picture of the ability of this type of catalyst to be employed in organic reactions to prepare valuable synthons that can be used in several value-added preparations.[116] Tuning of the oxidative properties of suitably modified g-C_3N_4 has a pivotal role in determining a sustainable change in the approach to $^1O_2$ generation methods, allowing for greener ways to perform organic reactions.

The large possibilities for g-C_3N_4 functionalization and controlling its catalytic activity make it a very promising material for the development of new solar-driven ecologically friendly reactions.[117] It must be noted that g-C_3N_4 is the most stable allotropic form of carbon nitride and possesses unique electronic properties as well as catalytic and photocatalytic activity.[118]

Upon pursuing our interest in finding new and greener methods for $^1O_2$ generation, as well as sustainable applications in the synthesis of valuable organic intermediates, we wish to report here our recent results concerning $^1O_2$ generation through a variety of modified g-C_3N_4 catalysts in the presence of metal halide perovskites (MHPs), thus forming a heterojunction composite. We have recently reported the favourable coupling of a lead-free 2D MHP derivative, namely PEA_2SnBr_4, with g-C_3N_4 for hydrogen photogeneration, demonstrating the synergic effect of coupling the two semiconductors in such a catalytic system.[12, 43, 61]

Considering the optical properties of MHPs and their derivatives, particularly the reduced charge carrier recombination and the strong absorbance, it is an appealing strategy to create novel catalytic systems where they improve the efficiency of traditional materials such as graphitic carbon nitride through the formation of a heterojunction composite. For these reasons, in the present work, we exploited the possible application of various catalytic systems, most of them already tested by our group for hydrogen photogeneration, composed of 2D or 3D materials, coupled to g-C_3N_4, to investigate the scope of the method in HDA, ene and oxidation reactions with representative dienes and alkenes.

We increased the number of substrates used to perform the reactions and found interesting as well valuable limitations occurring with some of them. The obtained value-added compounds are commonly the synthons for a remarkably high range of synthetic transformations, widely applied in modern organic synthesis and here derived from a sustainable and greener $^1O_2$ methodology in organic synthesis taking advantage of easily tuneable catalysts.

Experimental Methods and Discussion

We have prepared g-C_3N_4/PEA_2MX_4 (M = Pb and Sn; X = Br and Cl) and g-C_3N_4/$DMASnBr_3$ composites (Table 2.11) with the methodologies already discussed in the previous paragraphs.[43, 61] As mentioned above, such composites have been selected based on their favourable photocatalytic activity shown in hydrogen generation and organic pollutant degradation.[12, 43, 61] Such preliminary evidence suggests their possible exploitation in other catalysis fields as pursued in the present work.

Table 2.11 reports all the formulas of the catalysts with the corresponding labelling. To optimize the reaction conditions, and, to select the best performing catalyst from the list in Table 2.11, we conducted a typical $^1O_2$ HDA cycloaddition reaction with 1,3-cyclohexadiene using acetonitrile as a solvent, at room temperature for $24\,h$ (Scheme 2.1). The conditions were the same as those used in previous experiments catalysed by oxidized g-C_3N_4 and applied here for the sake of comparison.[116]

The choice of 1,3-cyclohexadiene is due to its reduced reactivity with respect to cyclopentadiene; this helps in limiting the potentially expected polymerization of the diene as well as side reactions under the experimental conditions. Irradiation was conducted under simulated solar light for $24\,h$, saturating the acetonitrile phase with pure oxygen, and leaving the reaction under an oxygen atmosphere. Table 2.12 reports the data relative to the different catalysts used and the yield values for the reaction at hand. In all the reactions, and as similarly done in the previous work,[116] we verified that the 1,3-cyclohexadiene conversions were quantitative by Gas Chromatography-Mass Spectroscopy (GC-MS) analyses that served also for the correct detection of the reaction products and structure attribution. Independent replicated experiments were performed to verify the obtained results.

Intermediate **1** represents the primary HDA cycloadduct and was never detected in all the performed experiments. 4-Hydroxycyclohex-2-en-1-one (**2**) was the only reaction product for the yields reported in Table 2.12. This hydroxyl ketone is a known compound derived from the reductive cleavage of the peroxide O−O bond and simultaneous

Table 2.11. List of the catalysts with their formula and literature references for preparation. Data reproduced from ref.[80]

Entry	Catalyst	Formula	ref.
1	**C1**	g-C_3N_4/PEA_2PbCl_4 5%	61
2	**C2**	g-C_3N_4/PEA_2SnBr_4 5%	61
3	**C3**	g-C_3N_4/PEA_2PbBr_4 5%	61
4	**C4**	g-C_3N_4/$DMASnBr_3$ 33%	37

oxidation of one of the hydroxy functionalities, both being pathways promoted by the catalyst; the structure was confirmed by comparison with that of authentic samples (primary standard compounds were purchased) as well as Nuclear Magnetic Resonance (NMR) characterization.[116]

Catalysts **C1–3** gave modest to good yields of compound **2** and the best result was obtained with catalyst **C4** (Table 2.12) that provided 63% yield of **2**. Catalyst **C4** ameliorated the results obtained with oxidized g-C_3N_4 alone (55% yield of compound 2).[116]

Based on the above-illustrated results, we also investigated the behaviour of cyclopentadiene to probe the scope of the reaction with a highly reactive diene, testing all the prepared catalysts. Scheme 2.2 shows the structures of the products obtained from the reaction of photogenerated $^1O_2$ with freshly distilled cyclopentadiene. The reaction conversion is complete although affected by an important amount of cyclopentadiene polymerization material. The composition of the reaction mixtures is reported in Table 2.13 as found by GC-MS analyses and comparison with standard references. The experimental conditions clearly activate a very fast cyclopentadiene dimerization that is responsible for the reaction outcome as shown in Scheme 2.2.

The primary HDA cycloadduct **3** was neither isolated nor detected in the final reaction mixtures from independent experiments. Compound **4** that derives from the peroxide bond reductive cleavage was not detected too. All the reported products are known in the cited literature and the structures are consistent with the reported data.[119–127]

Catalysts of type **C1–3** showed somewhat a similar behaviour with a neat preference for compound **5d** that is the bis-epoxy derivative of the cyclopentadiene dimer. Comparable amounts of the ketones **5a** and **5e** were observed (13 – 21%) as oxidation products

Table 2.12. Product **2** yields in photocatalysed HDA reactions with 1,3-cyclohexadiene. Data reproduced from ref.[80]

Entry	Catalyst	Product 2 (%)
1	**C1**	43
2	**C2**	26
3	**C3**	16
4	**C4**	63

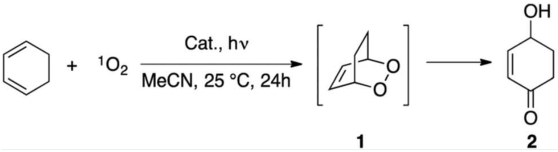

Scheme 2.1. HDA cycloaddition reaction of 1,3-cyclohexadiene and $^1O_2$ used as the benchmark reaction to test the efficiency of all the catalysts. Reprinted with permission from ref.[80] Copyright 2019 ACS Sustainable Chemistry & Engineering.

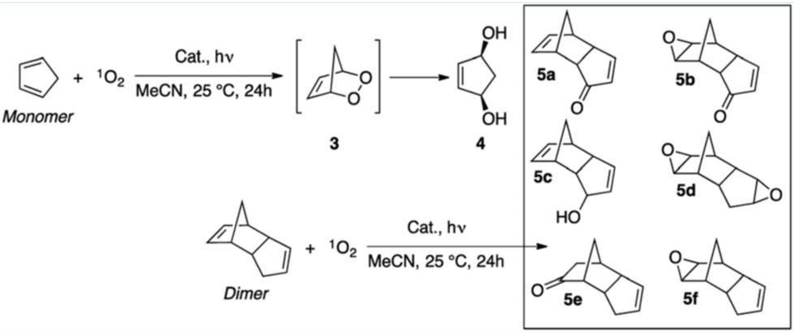

Scheme 2.2. HDA cycloaddition reaction of cyclopentadiene and $^1O_2$. Reprinted with permission from ref.[80] Copyright 2019 ACS Sustainable Chemistry & Engineering.

of the cyclopentadiene dimer. Minor amounts of the reduction product **5c** were also observed in the range of $5-13\%$ yield.

Ending with catalyst **C4**, the mono-epoxy derivative of the cyclopentadiene dimer **5f** was obtained in 43% yield, along with up to 10% of ketones **5a** and **5b**.

Oxidation of alkenes and ene reactions represent another important task where $^1O_2$ plays a pivotal role in olefin functionalization, extremely useful for the synthesis of allylic alcohols and unsaturated carbonyl compounds and, in general, value-added compounds.

The investigations in this field were conducted on a variety of alkenes, acyclic and cyclic, ranging from the highly C=C double bond substituted ones, such as tetramethylethylene (TME) and trimethylethylene (tME), to the monosubstituted ones (for example 1-octene). The studies were extended to some aromatic alkenes, such as allylbenzene, indene and dihydroanthracene. In all these cases, the reactions were performed by using the catalyst that gave the best performances in HDA cycloadditions (catalyst **C4**) under the typical set-up experimental conditions above reported.

Scheme 2.3 shows the results corresponding to the first series of reactions of $^1O_2$ conducted in the presence of cyclic olefins. In addition, we tested acyclic alkenes, from mono- to tetra-substituted ones with different degrees of substitution on the C=C double bond as reported in Scheme 2.4.

Cyclic alkenes (from 5- to 8-membered rings) gave interesting and various results that can be classified within allylic oxidation reactions such as in the cases of products **6a**, **6b**, **7a**, **7b**, **8b** and **9b** (Scheme 2.3). The product yields are fair; good performances are observed for cyclohexene where a variety of oxidized compounds were obtained with poor chemoselectivity. Some epoxydated products are often

Table 2.13. Product distribution in the photocatalysed HDA reactions with cyclopentadiene. Data reproduced from ref.[80]

Entry	Catalyst *	yield (%)						
		4	**5a**	**5b**	**5c**	**5d**	**5e**	**5f**
1	**C1**	-	13	-	5	30	21	-
2	**C2**	-	13	-	13	34	15	-
3	**C3**	-	16	-	7	27	13	-
4	**C4**	-	9	10	-	-	-	43

* the amount of catalyst is 13% *wt* with respect to cyclopentadiene

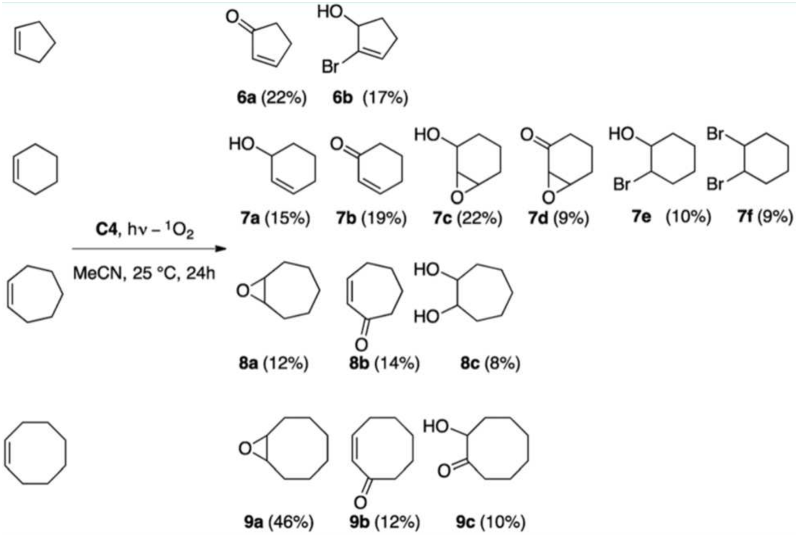

Scheme 2.3. Oxidation products from cyclic alkenes in $^1O_2$ photocatalysed reactions. Reprinted with permission from ref.[80] Copyright 2019 ACS Sustainable Chemistry & Engineering.

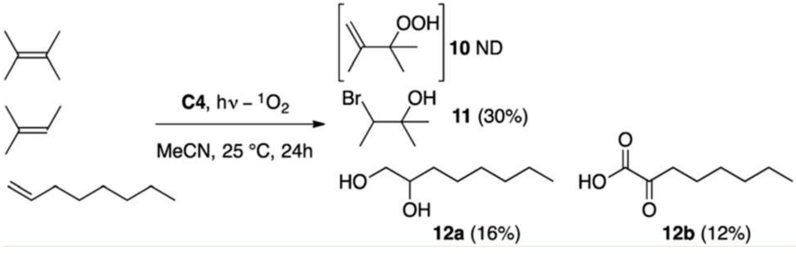

Scheme 2.4. Oxidation products from acyclic alkenes in $^1O_2$ photocatalysed reactions. Reprinted with permission from ref.[80] Copyright 2019 ACS Sustainable Chemistry & Engineering.

obtained in particular for 6-, 7- and 8-membered rings. Remarkably, compound **9a** was obtained in nearly 50% yield. Cyclooctene also affords compound **9c** derived from partial reductive processes. Lastly, the structures of brominated compounds **6b**, **7e** and **7f** can be attributed on the basis of the presence of bromide anions in the catalysts. All the detected products are known compounds reported in the cited literature.[128–132]

On the other hand, acyclic alkenes were quite unproductive (Scheme 2.4); the ene adduct **10**, quantitatively prepared in previous studies,[116] could not be obtained here and compound **11** was obtained in modest yields and ”suffers” from the presence of bromide from the catalyst structure. Disubstituted alkenes, such as cis-2-hexene or trans-4-nonene, just to cite some of the tested olefins, did not give any positive result. In contrast, the monosubstituted 1-octene underwent oxidative pathways to afford in fair yields the diol **12a** and the ketoacid **12b**. The structures were confirmed upon comparison with known data reported in the cited literature and the used appropriate standard reference compounds.[133–135]

Representative aromatic unsaturated compounds were also tested in photocatalysed $^1O_2$ reactions and the results are shown in Scheme 2.5. Indene (**13**) is prone to be oxidized with our catalytic method but the primary ene adduct **14a** was not detected in the crude reaction mixture. The diol **14b** was obtained in the reactions with catalyst **C4** in fair yields as a mixture of cis- and trans- isomers while ketone **14c**, a product of the direct oxidation of the sp^2 carbon atom, was also obtained. Dihydroanthracene (**15**) afforded anthraquinone **16a** in excellent yields (71%). The reaction is accompanied by the formation of anthracen-9(10H)-one (16 b) (9% yield) and of anthracene (**16c**) from complete reduction of the starting material in 20% yield. Finally, we also investigated the oxidation of allylbenzene (**17**). A poorly chemoselective process results in the yields of the obtained products **18a–f**. The primary ene adduct **18a** was obtained in 3% yield using catalyst **C4**. Cinnamaldehyde (**18b**) and the corresponding alcohol **18c** are the major products along with the hydroxylketone **18d**. Minor amounts of **18e** and **f** complete the mix of the products. All the compounds reported in Scheme 2.5 are known in the literature[136–140] and some of them were already reported in our previous work.[116]

In summary, g-C_3N_4/PEA_2MX_4 and g-C_3N_4/$DMASnBr_3$ com-

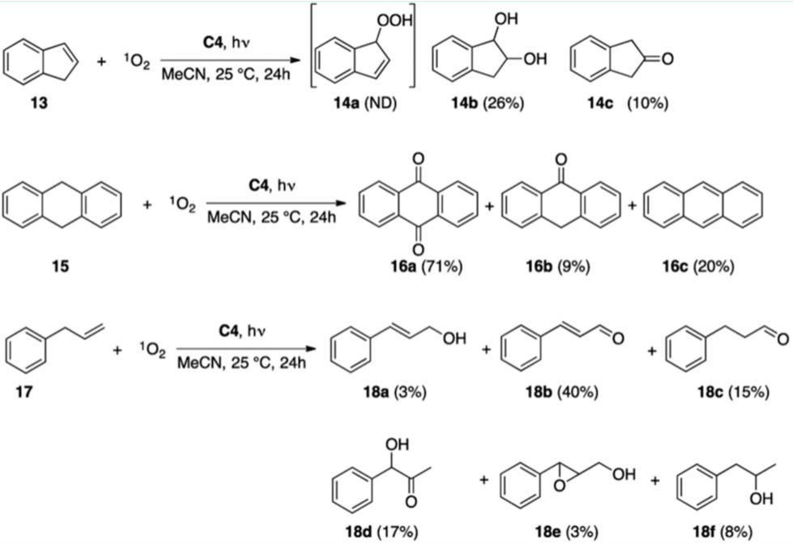

Scheme 2.5. Oxidation products from aromatic compounds in $^1O_2$ photocatalysed reactions. Reprinted with permission from ref.[80] Copyright 2019 ACS Sustainable Chemistry & Engineering.

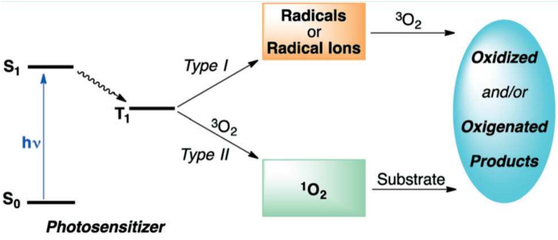

Scheme 2.6. Photooxidation reactions of type I and type II pathways. Reprinted with permission from ref.[80] Copyright 2019 ACS Sustainable Chemistry & Engineering.

posites were prepared and used as photocatalysts in HDA, ene and general oxidation reactions of alkenes. HDA cycloaddition reactions with 1,3-cyclohexadiene and cyclopentadiene were used to define the best catalysts to conduct photooxidative processes with a variety of substrates. Catalyst **C4** was found to give the best results with HDA in the presence of 1,3-cyclohexadiene, affording compound **2** up to 63% yield, ameliorating our previous results obtained with simple oxidized g-C_3N_4 as the catalyst.[116]

In spite of the new catalysts employed, cyclopentadiene continues to confirm its extreme reactivity towards dimerization; this spontaneous tendency also accompanied by polymerization under the experimental conditions offers however the possibility to obtain a variety of oxidized compounds of the dimer itself.

Interesting results were obtained with cyclic alkenes of different ring sizes. The oxidation reactions are not chemoselective but α,β-unsaturated ketones are often the main products of the reactions along with the epoxides. Less promisingly, the results of acyclic alkenes do not offer a picture of the applicability of the methodology for this type of molecule, presumably not structurally fit to interact positively with the catalysts in order to give valuable oxidized compounds. Finally, aromatic compounds such as indene, dihydroanthracene and allylbenzene were easily oxidized by the selected catalysts. Specifically, catalyst **C4** did not give quantitatively anthraquinone **16a** as in our previous work[116] but still, **16a** remains the major product (up to 71%). Indene is mainly oxidized to the corresponding diol **14b** and allylbenzene offers a wide selection of oxidized compounds.

We have conducted photocatalysed reactions with in situ $^1O_2$ generation in the presence of a variety of olefinic compounds. The catalysts used in the present work are substantially different from the oxidized g-C_3N_4 previously employed and offer a large matter of discussion, however, in close similarity, all the catalysts examined in this study display a low chemoselectivity in the presence of some substrates or even in the absence of any reaction.

These outcomes lead to the introduction of the possibility to differentiate between photooxidation reactions of type I and type II as shown in Scheme 2.6.[141] Radicals or radical-ions can be photogenerated by suitable triplet state sensitizers and oxygen suitably trapped to give the oxidized products according to the type I photoreaction. An example is offered by the absence of any $^1O_2$ ene reactions in some of the examined reactions; the presence of other non-$^1O_2$ products such as in the indene case suggests a process promoted by a type I reaction, derived from oxygen radicals and oxygen radical ions.[142–144] On the other hand, the sensitizer promotes the $^1O_2$ formation which undergoes oxidation reactions with various substrates (type II). To discern between these two types of mechanisms, new studies are needed (chemical trap investigations) and can be reasonably planned.

Looking at Table 2.12, it is possible to observe that the best performing composite, providing the highest reaction yield, is the one containing $DMASnBr_3$ (**C4**). This general trend agrees with the superior photocatalytic activity observed during hydrogen photogeneration for this system relative to **C1**–**C3**, suggesting a direct correlation between the general activity level and the further use in HAD reactions.[43, 61] On the other hand, among the 2D-based systems, the best activity is found for **C1** (PEA_2PbCl_4) which has a band-gap centred at around $3.6\,eV$, i.e. in a region where the redox potentials may even directly promote oxidation reactions. **C2** and **C3** have analogous bandgaps of $\approx 2.7 - 2.8\,eV$ and provide a direct synergy with carbon nitride (bandgap of $\approx 2.75\,eV$) in terms of charge carrier transfer.[43, 61] However, as we determined through computational modelling, such a positive band-alignment between the two semiconductors has the maximum efficiency for **C4**, as demonstrated by the reaction yields. Let us also remember that the charge carrier lifetimes are generally longer for 3D perovskites also due to the lower binding energies, resulting in higher photocatalytic efficiencies.[12]

The selectivity reported in Table 2.13 suggests a correlation between the type of perovskite used in the heterojunction formation (2D or 3D) and the product selectivity of the reaction. In this case, irrespective of the relative yields, 2D-based systems, both containing Br or Cl and Pb or Sn, behave similarly. In this respect, and considering the above reported arguments, it seems that the increase in catalytic activity of **C4** directly correlates with the product selectivity.

Conclusions

In conclusion, we can affirm that the g-C_3N_4/PEA_2MX_4 and g-C_3N_4/$DMASnBr_3$ composites are interesting and valuable photocatalysts for the in situ generation of $^1O_2$ to perform HDA, ene and oxidation reactions with suitable dienes and alkenes.

The methodology has been reasonably standardized and made applicable to a variety of olefinic substrates. The scope of the method has been finely illustrated by the results in all the tested reactions, which allowed for obtaining of desymmetrized hydroxy-ketone derivatives, unsaturated ketones, and epoxides. Notable limitations were also observed especially in the case of the alkene oxidation as well as the poor chemoselectivity somewhere observed.

The tuned-up oxidative properties of the suitably modified g-C_3N_4 catalysts offer a remarkable improvement in determining a change in the approach to singlet oxygen generation methods that may open other ways to perform organic reactions through greener and sustainable methodologies.

$Cs_3Bi_2Br_9$

Experimental Strategy and Mechanistic View to Boost the photo-catalytic Activity of $Cs_3Bi_2Br_9$ Lead-Free Perovskite Derivative by C_3N_4 Composite Engineering[145]

Purpose

In this work, an experimental and computational study on the synergic coupling between a lead-free all-inorganic perovskite, namely $Cs_3Bi_2Br_9$, and C_3N_4 is presented.

A relevant boost of the hydrogen photogeneration by more than one order of magnitude is recorded when going from pure C_3N_4 to the $C_3N_4/Cs_3Bi_2Br_9$ system. Effective catalytic activity is also achieved in the degradation of an organic pollutant, with MB as a model molecule. Based upon complementary experimental outputs and advanced computational modelling, a rationale is provided to understand the heterojunction functionality as well as the trend of hydrogen production as a function of perovskite loading.

Introduction

In the past few years MHPs, with general formula ABX_3, where A is a monovalent cation, B a divalent metal cation, and X is a halide anion, have emerged among the most promising materials for optoelectronic applications, because of their tuneable direct band gap, high absorption coefficient, low exciton binding energy, and high carrier mobility.[22,146] Several potential optoelectronic applications of MHPs have been proposed, spanning from emitters for next-generation light emitting diodes, emitters in coherent-light sources and mainly as absorbers in solar cells providing high power conversion efficiencies.[147] Further potential use of MHPs lies in the development of field-effect transistors, photodetectors, and photo transistors which all require a low exciton binding energy.[148]

In the last few years, MHPs have also attracted significant attention for their possible use in heterogeneous photo-catalysis, in virtue of the long carrier lifetimes and high mobility, together with a good defect tolerance and easily tuneable band gap in the visible region to catalyse solar-driven reactions.[12,13,15,16,149] Furthermore, the band alignment of the various MHPs with the most common redox half-reactions determines their thermodynamic suitability to effectively run both reduction and oxidation reactions.[13] Among the solar-driven processes of current interest, MHPs have been studied for the evolution of hydrogen, the reduction of carbon dioxide, the photodegradation of dyes and contaminants, and the synthesis of organic compounds.[12,13,15,16,149]

MHPs for photo-catalytic applications share the same problems of those used as absorbers in photovoltaics:[12]

- the most-efficient MHPs are lead-based with the intrinsic toxicity of this element being extremely undesirable for mass production;
- the poor stability under moisture/water exposure.

Therefore, the development of novel MHPs for photo-catalysis need to overcome these issues. Replacing lead may be achieved by using metals with similar electronic structure and comparable ionic radius to obtain analogous optoelectronic properties along with a stable perovskite structure. Moreover, the organic cations may be replaced with alternative inorganic cations to increase the photostability of the perovskite.[146]

In this context, given their similar electronic configuration, Group 14 Sn^{2+} and Ge^{2+} and Group 15 Bi^{3+} and Sb^{3+} were employed as Pb^{2+} substitutes to obtain stable perovskite and perovskite-derivate structures.[146,150] In particular, tin-based perovskites exhibit a narrower band gap compared with their lead analogues, they have low exciton binding energies and longer carrier diffusion lengths, however they are often sensitive towards moisture and oxygen since Sn^{2+} tends to oxidize to Sn^{4+}.[146] Likewise, germanium-based perovskites, while possessing similar electronic conductive behaviour, stability and optical properties compared with lead-based perovskites, are also affected by Ge^{2+}/Ge^{4+} oxidation.[146] Bi^{3+} has the advantage of having not only an electronic configuration similar to Pb^{2+} but also a comparable ionic radius and, in fact, $A_3Bi_2X_9$ perovskite-derivates demonstrated high Photoluminescence Quantum Yields (PLQY) and moisture and air stability.[146,150] On the other hand, antimony-based perovskite derivatives, with the same $A_3Sb_2X_9$ structure of the bismuth-based materials, still show low efficiencies.

Given their good water stability, bismuth-based perovskite derivates have already shown promising results as heterogeneous photocatalysts; Bresolin et al. used $Cs_3Bi_2I_9$ for the photodegradation of dyes, as model organic pollutants, and for hydrogen evolution.[151–153] Bhosale et al. employed three different bismuth-based materials ($Cs_3Bi_2I_9$, $Rb_3Bi_2I_9$ and $MA_3Bi_2I_9$) for the photoreduction of carbon dioxide to carbon monoxide and methane at the gas–solid interface,[154] while Dai et al. used $Cs_3Bi_2Br_9$ for the photo-catalytic addition of alcohols to epoxides, for the production of β-alkoxyalcohols.[155] Furthermore, they synthetized a heterogeneous structure of $Cs_3Bi_2Br_9$ nanoparticles embedded in mesoporous silica that they used for the selective photo-catalytic activation of $C(sp^3)-H$ bonds.[156]

Focusing on the visible-light photogeneration of hydrogen, a few perovskites have already been employed as heterogeneous photocatalysts for the evolution of hydrogen, but, since most perovskites are unstable in aqueous environment, the vast majority of measurements have been conducted in hydrohalic acids that prevent the complete dissolution of the perovskite by common-ion effect.[12] However, being hydrogen production from concentrated acids hardly sustainable, the development of water-stable photo-catalysts is imperative.[12]

Based on the above considerations, Bi-based perovskite materials are suitable candidates for effective photocatalytic hydrogen evolution in aqueous media due to their demonstrated stability.[151–153]

For this reason, herein, we report the synthesis and the characterization of a new heterogeneous photo-catalyst, namely $C_3N_4/Cs_3Bi_2Br_9$, achieved by coupling the semiconducting $Cs_3Bi_2Br_9$ (with a band gap of $\approx 2.7\,eV$) to the well known visible light absorber C_3N_4 material (band gap of $\approx 2.72\,eV$), that is active under visible light irradiation.[155]

The coupling of MHPs with C_3N_4 to create photo-catalytically efficient composites is becoming a widespread strategy in the current literature for various kinds of photoreactions.[80, 157, 158] In the present paper, we decided to take advantage of bismuth resistance to oxidation and $Cs_3Bi_2Br_9$ water stability to develop this new composite material, expecting a positive band-alignment between the two semiconductors and therefore improved charge carrier dynamics as observed by some of us in other composites.[37, 61] The photo-catalytic activity of the $C_3N_4/Cs_3Bi_2Br_9$ composites, for different loading amounts of perovskites, has been tested by studying the hydrogen evolution reaction in an aqueous solution as well as the degradation of MB, representative of organic pollutants.[37, 61]

Experimental Methods and Discussion

Pristine $Cs_3Bi_2Br_9$ has been synthesized by precipitation from dimethylformamide (DMF) starting from a stoichiometric solution of the halide precursors, as already performed for the C_3N_4/PEA_2SnBr_4 samples.[61]

In Figure 2.29a, the sketch of the crystal structure is reported, while in Figure 2.29b is shown the appearance of the synthesized yellow powders. Figure 2.29c reports the XRD pattern of as-prepared $Cs_3Bi_2Br_9$, overlapped to the reference XRD pattern (trigonal symmetry, space group $P-3m$),[159] from which it can be said that the material is single-phase and presents a slight preferential orientation along the $(00l)$ crystal direction.

Water stability of $Cs_3Bi_2Br_9$ has been determined by a leaching test where $15\,mg$ of the perovskite has been placed in $5\,mL$ of water under magnetic stirring, and the amount of Bi in the solution has been determined by ICP-OES. At 4, 7, and $16\,h$ of stirring, the Bi amount detected in the solution was always $< 0.05\%$ (detection limit) of the total amount of bismuth present in the perovskite, indicating an impressive water stability.

In order to improve its efficiency, $Cs_3Bi_2Br_9$ was coupled with C_3N_4 in order to produce a series of composite materials. The

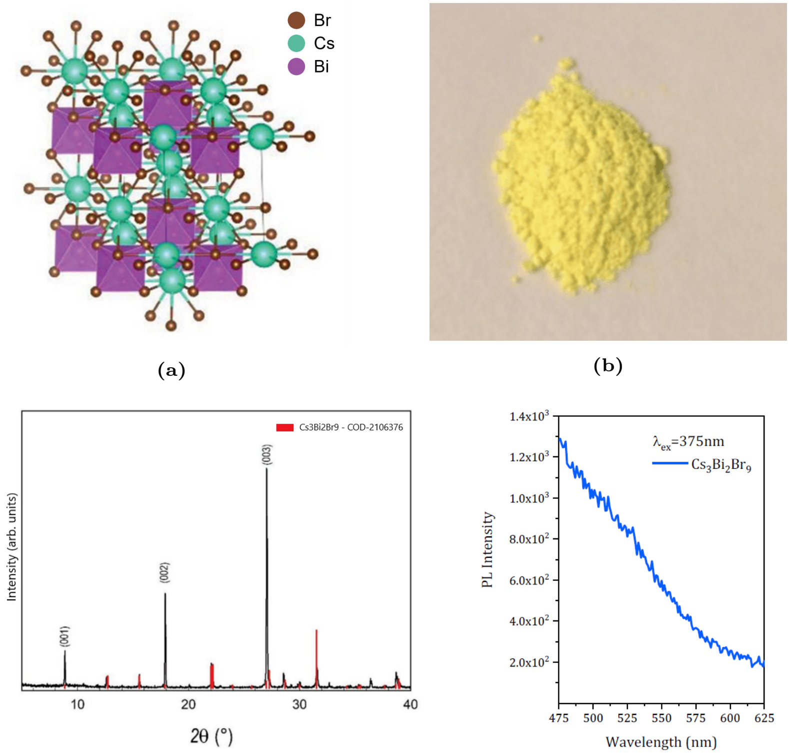

(a) **(b)**

(c) **(d)**

Figure 2.29. a) Sketch of the crystal structure of $Cs_3Bi_2Br_9$; b) appearance of the bulk sample; c) XRD pattern of the sample where red vertical bars refer to the reflection positions for trigonal structure of the perovskite ($P-3m$); d) Emission spectrum of $Cs_3Bi_2Br_9$ presenting a weak and broad peak centred at 525 nm. Reprinted with permission from ref.[145] Copyright 2021 Advanced Functional Materials.

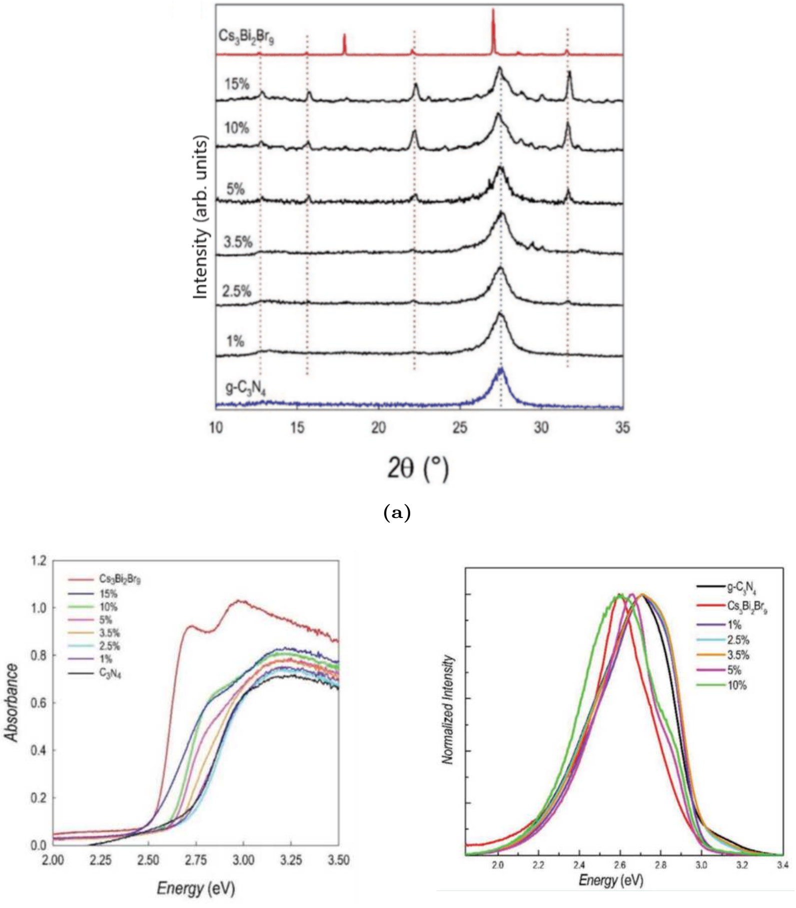

(a)

(b)

(c)

Figure 2.30. a) XRD pattern of $C_3N_4/Cs_3Bi_2Br_9$ composites at different percentages of perovskite loading ($\% \, wt$). C_3N_4 and $Cs_3Bi_2Br_9$ refer to pristine materials. b) Absorption spectra of the composites versus energy (percentages refers to the $\% \, wt$ of $Cs_3Bi_2Br_9$ in the composite); c) Emission spectra of $C_3N_4/Cs_3Bi_2Br_9$ composites powders at different percentages of perovskite loading ($\% \, wt$). C_3N_4 and $Cs_3Bi_2Br_9$ refer to pristine materials. $\lambda_{ex} = 375 \, nm$. Reprinted with permission from ref.[145] Copyright 2021 Advanced Functional Materials.

$C_3N_4/Cs_3Bi_2Br_9$ composites (% wt of perovskite: 1, 2.5, 3.5, 5, 10, and 15) have been characterized in terms of crystal structure, optical properties, and morphology. Figure 2.30a shows the XRD patterns of all prepared materials starting from pure C_3N_4 followed by composites at increasing amounts of $Cs_3Bi_2Br_9$.

Pure C_3N_4 shows the common diffraction pattern mainly characterized by a typical broad peak around 28° which is found in all the composites, where carbon nitride represents the main phase. Concerning the $Cs_3Bi_2Br_9$ contribution to the patterns, this starts to be slightly visible already at 2.5% wt of loading, but its clear signature is found starting from about 5% wt, with a progressive relative intensity increase which follows the increasing quantity of perovskite contained in the composites.

The optical properties of the $C_3N_4/Cs_3Bi_2Br_9$ composites have been determined by UV–Vis absorption spectroscopy and the data are reported in Figure 2.30b as a function of energy. Pure C_3N_4, and composites with 1% wt and 2.5% wt loading of perovskite, have very similar absorption spectra, while a contribution shifting the absorption edge to lower-energies starts to be evident from the 3.5% wt sample and becomes clearer when increasing the perovskite amount and can be associated with the $Cs_3Bi_2Br_9$ exciton, as previously reported for this and other $Cs_3Bi_2X_9$ materials.[12,160,161]

The normalized Photoluminescence (PL) spectra of pure compounds and composites, reported in Figure 2.30c, present a similar threshold behaviour. Pure C_3N_4, shows a relatively broad emission, peaking at $2.7\,eV$, corresponding to the band-band PL phenomenon of C_3N_4, only $0.15\,eV$ downshifted relatively to its band gap energy (Figure 2.30c).[162] Noticeably, the composites up to 3.5% wt loading of perovskite, show very similar emission spectra while, starting from the 5% wt sample, a shift toward low energies is observed. This suggests that the emission begins to be affected by contributions from $Cs_3Bi_2Br_9$ at higher loading of the perovskite. In fact, pristine $Cs_3Bi_2Br_9$ shows a relatively narrow and weak emission peaking at $2.59\,eV$ and, although with a broader energy distribution, the emission of the 10% wt composite resembles it.

The morphologies of the pure samples and composites have been assessed by SEM and are reported in Figure 2.31. Surface area of all the samples has been determined by B.E.T adsorption method and the results are reported in Table 2.14. As-prepared C_3N_4 shows a sur-

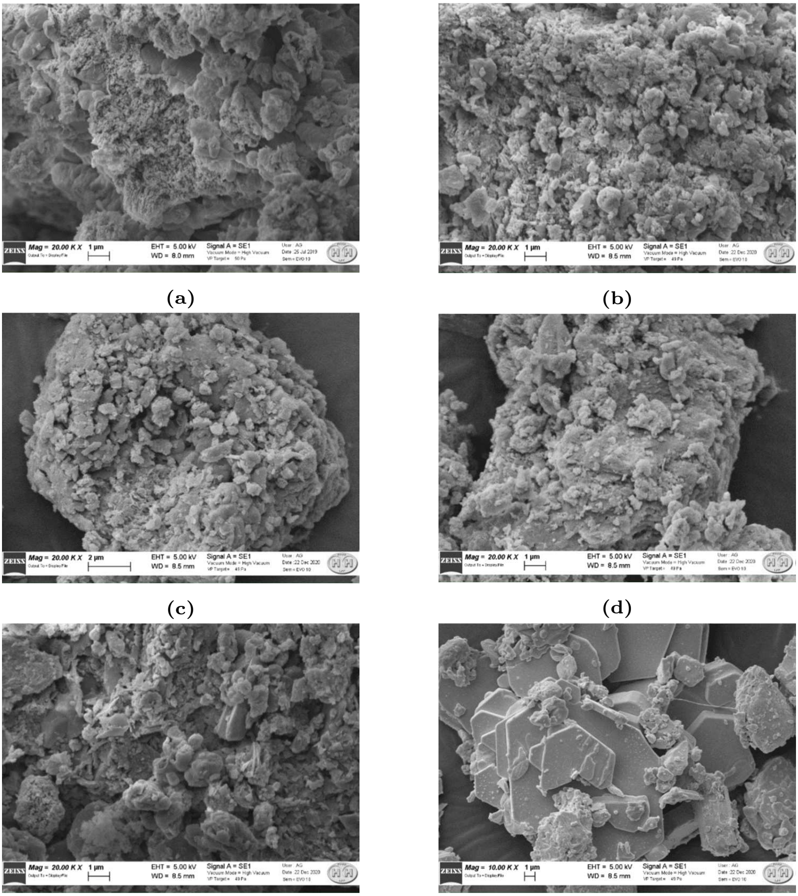

(a) **(b)** **(c)** **(d)** **(e)** **(f)**

Figure 2.31. SEM images of a) C_3N_4; b) $C_3N_4/Cs_3Bi_2Br_9$ 2.5% *wt*; c) $C_3N_4/Cs_3Bi_2Br_9$ 5% *wt*; d) $C_3N_4/Cs_3Bi_2Br_9$ 10% *wt*; e) $C_3N_4/Cs_3Bi_2Br_9$ 15% *wt*; and f) $Cs_3Bi_2Br_9$. Reprinted with permission from ref.[145] Copyright 2021 Advanced Functional Materials.

face area around $76\,m^2\,g^{-1}$ which remains substantially unchanged, within the estimated standard deviation of the measurement, up to $5\%\,wt$ loading of perovskite. A slight reduction of surface area is observed at $10\%\,wt$ and $15\%\,wt$ loadings reaching a value around $50\,m^2\,g^{-1}$. In general, however, the variation in the surface area is not particularly large thus indicating, with reference to the photocatalytic results which will be shown later, that this is not the key parameter in affecting the trend of composites activity.

The solar-driven catalytic efficiency of the prepared composites has been first determined in terms of HER by employing usual protocols applied in the current literature for C_3N_4-based composites, i.e., in $10\%\,\frac{V}{V}$ aqueous TEOA, as a typical sacrificial agent, and with Pt ($3\%\,wt$) as metal cocatalyst.[44] The following results have been performed on several sample replicas.

The HERs results as a function of perovskite loading for pure C_3N_4 and for the composites are shown in Figure 2.32a, showing an enhancement of the HER from pure C_3N_4 ($81\,\mu mol\,g^{-1}\,h^{-1}$) to $C_3N_4/Cs_3Bi_2Br_9$ $1\%\,wt$ and $2.5\%\,wt$ composites, reaching, at this last perovskite loading, the highest HER of about $\approx 1050\,\mu mol\,g^{-1}\,h^{-1}$. Further perovskite loading leads to a progressive reduction of the efficiency of hydrogen photogeneration (reaching, for pure $Cs_3Bi_2Br_9$ a HER of $22\,\mu mol\,g^{-1}\,h^{-1}$), and this trend has been later analysed by coupling advanced optical characterization tools and computational modelling.

Clearly, achieving an optimal HER at a low-loading of perovskite cocatalyst is a positive result in terms of material manufacturing and

Table 2.14. Surface area of C_3N_4 and $C_3N_4/Cs_3Bi_2Br_9$ composites at different percentages of MHP loading. Experimental standard deviation $\pm 5\%\,wt$. Data have been reproduced from ref.[145]

Sample	**Surface Area ($m^2\,g^{-1}$)**
C_3N_4	76
$C_3N_4/Cs_3Bi_2Br_9$ $1\%\,wt$	74
$C_3N_4/Cs_3Bi_2Br_9$ $2.5\%\,wt$	73
$C_3N_4/Cs_3Bi_2Br_9$ $3.5\%\,wt$	71
$C_3N_4/Cs_3Bi_2Br_9$ $5\%\,wt$	66
$C_3N_4/Cs_3Bi_2Br_9$ $10\%\,wt$	53
$C_3N_4/Cs_3Bi_2Br_9$ $15\%\,wt$	51

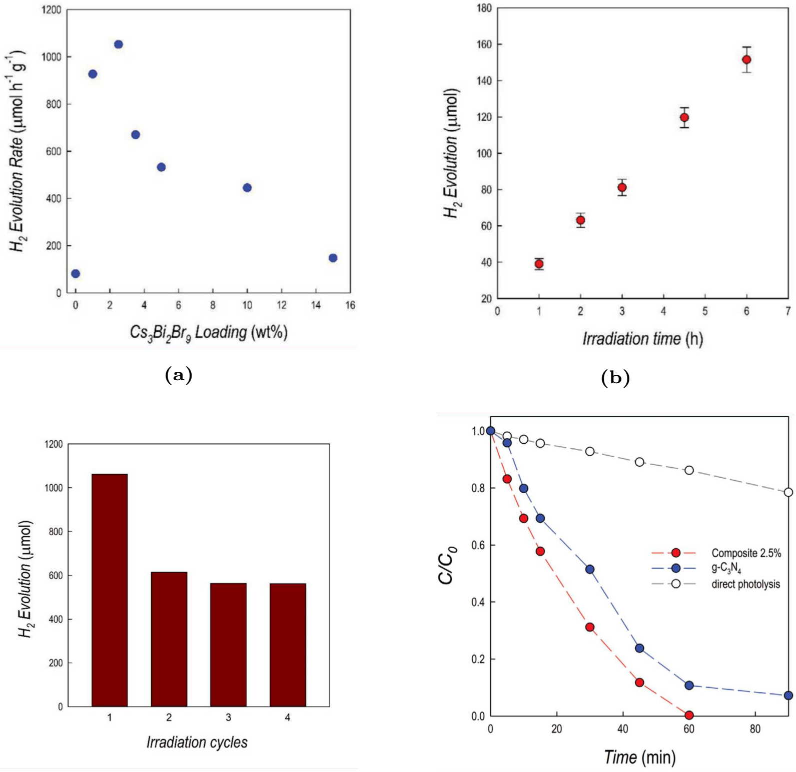

(a) **(b)**

(c) **(d)**

Figure 2.32. a) HER ($1\,g\,L^{-1}$ catalyst, $10\%\,\frac{V}{V}$ TEOA, $3\%\,wt$ Pt, $6\,h$ irradiation) for $C_3N_4/Cs_3Bi_2Br_9$ composites at different percentages of MHP loading. b) Hydrogen evolution profile over irradiation time for the $C_3N_4/Cs_3Bi_2Br_9$ $2.5\%\,wt$ composite. c) HER as a function of irradiation cycles on $C_3N_4/Cs_3Bi_2Br_9$ $2.5\%\,wt$ composite. d) Variation of MB concentration as a function of irradiation time ($1\,g\,L^{-1}$ catalyst) for $C_3N_4/Cs_3Bi_2Br_9$ composite at $2.5\%\,wt$ loading and C_3N_4, compared to photolysis effect. Xenon lamp, ($500\,W\,m^{-2}$ for H_2 evolution, $250\,W\,m^{-2}$ for MB degradation), $300-800\,nm$, IR-treated soda lime glass UV outdoor filter). $RSD < 10\%$ ($n = 3$). Reprinted with permission from ref.[145] Copyright 2021 Advanced Functional Materials.

cost. This result clearly indicates a strong synergy between the two semiconductors in the $C_3N_4/Cs_3Bi_2Br_9$ composites.

For the optimal composite, namely at 2.5% *wt* of $Cs_3Bi_2Br_9$, the kinetics of H_2 was studied and the trend, reported in Figure 2.32b, indicates a substantial linear increase of the produced hydrogen as function of time.

The XRD pattern of the spent catalyst has been collected and compared with the one of the fresh material. This has been done in particular for the sample with 15% *wt* of $Cs_3Bi_2Br_9$, in order to better highlight the perovskite reflections. The comparison of the two patterns is reported in Figure 2.33 indicating a very good stability of the material after a photocatalytic run.

In addition, on the best performing composite, namely $C_3N_4/Cs_3Bi_2Br_9$ 2.5% *wt*, we carried out four successive photocatalytic runs by collecting the sample each time by centrifugation. The performance of the HER in this reuse test is reported in Figure 2.32c. This last test revealed, overall, a good stability of the composite over 4 cycles, although with a drop in efficiency after the first cycle of about 40% *wt*. After the first cycle the HER remains constant (at 8 times the HER of pristine C_3N_4), indicating a very effective synergy between the two semiconductors in the composite.

Finally, the photo-catalytic activity of the 2.5% *wt* composite was also tested to verify its ability toward the decomposition of organic dyes, by selecting MB as a representative model compound of this class.

The results of the test are reported in Figure 2.32d showing the time-dependent absorbance for pure C_3N_4, for the composite, and for direct photolysis. This experiment confirms the very good performance of the $C_3N_4/Cs_3Bi_2Br_9$ composite also for the organic dye degradation, with a total degradation achieved in 60 *min*, while pure C_3N_4 is not able to fully degrade MB even after 90 *min* of irradiation.

To deepen the understanding of the composite behaviour and the peculiar effect of perovskite inclusion we prepared a series thin films deposited on transparent glass support.

Their normalized PL spectra are reported in Figure 2.34a. These emissions are dominated by the broad and intense features of carbon nitride. These broadbands, that completely cover the weak perovskite emission (Figure 2.29d), derive from the superimposition of multiple electronic transitions (Figure 2.34b).[163] Apart from the high energy

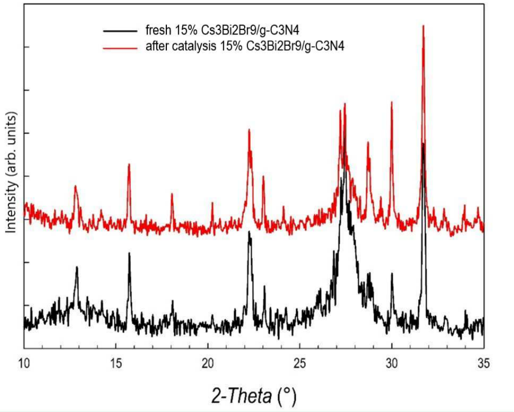

Figure 2.33. XRD pattern of $C_3N_4/Cs_3Bi_2Br_9$ 15% *wt* composite before and after catalysis. Reprinted with permission from ref.[145] Copyright 2021 Advanced Functional Materials.

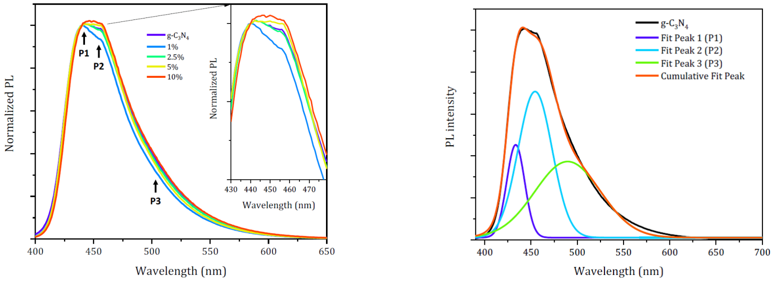

(a) **(b)**

Figure 2.34. a) Normalized Emission spectra of $C_3N_4/Cs_3Bi_2Br_9$ composites thin films at different percentages of perovskite loading (% *wt*). C_3N_4 refer to pristine material. Peak positions are labelled and indicated with arrows; b) emission spectrum of C_3N_4 thin film, the multiple peak fitting with gaussian results in three components centred at around 440 *nm* (P1), 455 *nm* (P2) and 505 *nm* (P3). $\lambda_{ex} = 375\,nm$. Reprinted with permission from ref.[145] Copyright 2021 Advanced Functional Materials.

one, which is a direct consequence of the absorption, and it is usually centred at around 440 nm, the low energy features at 455 nm and 505 nm are favoured by a non-radiative population of sub-band states, their intensity depends in fact on the population of a sp^2 C−N π band which is boosted by the presence of defects in the material.[163]

By zooming the emission band peak (inset of Figure 2.34a) it is clear how for the initial perovskite inclusion (1% wt sample) there is a reduction of low energy bands emission, in other words a reduction of the defects mediated radiative paths. Conversely, by increasing the perovskite content, the low energy transition becomes more and more pronounced.

Noticeably, it has been proposed that the photocatalytic activity of C_3N_4 could be related to the material purity. Samples containing large defect densities were less efficient in degrading organic pollutant under light irradiation, and the evidence coming from steady state PL shows how perovskite inclusion can improve C_3N_4 purity to a certain extent while, when the doping is greater than 2.5% wt, this inclusion starts to be detrimental resulting in non-radiative paths becoming more and more active.[164]

$Cs_3Bi_2Br_9$, in addition to defect distribution influence, also acts as an active player in the charge dynamics fate in virtue of its accessible states.

Herein, femtosecond transient absorption spectroscopy (TAS), a pump–probe technique consisting in measuring the ultrafast transient absorption changes induced by pulsed laser excitation, was employed to understand the excited state dynamics in photocatalytic materials.

Films of pure C_3N_4 and composite samples were excited with 100 fs, 345 nm, laser pulses to create photo-excitations. Absorption changes were monitored with a broadband, white light supercontinuum probe.

TAS is a complementary technique with respect to time-resolved PL because it is sensitive to all photo-excitations, even the dark ones, like charge-separated states that are crucial to achieve photocatalytic activity. Despite similar PL dynamics, composites with different perovskite fractions displayed extremely different TAS signals (represented in Figure 2.35).

For both starting materials, C_3N_4 and $Cs_3Bi_2Br_9$, as well as the composite with 10% wt perovskite loading, a broadband, negative differential transmission signal is observed, corresponding to photoinduced absorption. On the contrary, composites with perovskite loading of 1, 2.5, and 5% *wt*, i.e., the composites with enhanced photocatalytic activity, a positive differential transmission signal appears, corresponding to bleaching (Figure 2.35b).

Photoinduced absorption in C_3N_4 has been attributed to photoexcited electrons.[165–169] Concerning the pure perovskite, a broadband photoinduced absorption below the band gap has been associated, in double halide perovskites with Cs and Bi, to self-trapped excitons, meaning optical excitations stabilized by a lattice relaxation.[161]

In contrast, bleaching, due to phase-space filling in the excited state, only occurs at photon energies corresponding to the band gap, i.e., at the high-energy boundary of the spectral region we investigated.[170] On the other hand, bleaching is not expected as an intrinsic effect for photon energies below the band gap, and therefore could be attributed to the filling of defect states, most probably at the interface separating the two materials.

TAS measurements therefore point to the fact that the addition of $Cs_3Bi_2Br_9$ to C_3N_4, at least for loadings lower than 5% *wt*, introduces a path for optical excitations that does not exist in pure materials. For perovskite loadings greater than 5% *wt*, such an effect seems to fade, as the TAS signal reverts to both a spectral shape and a time decay similar to pure C_3N_4.

The origin of this peculiar optical behaviour at the bases of the performances of the $Cs_3Bi_2Br_3/C_3N_4$ composites has been further investigated by advanced fist-principles calculations.

We align the band edges of C_3N_4 and $Cs_3Bi_2Br_9$ with respect to a computational standard hydrogen electrode via the vacuum level. For both materials, the calculations are carried out in order to reproduce the measured fundamental gaps.[57, 170, 171]

The results illustrated in Figure 2.37 show that the alignment of the band edges between the constituents of the composite should in principle favour efficient charge separation. In fact, the valence and conduction band edges of C_3N_4 are placed, respectively, at 6.0 and $3.0\,eV$ (those of $Cs_3Bi_2Br_9$ are placed, respectively, at 5.79 and $2.79\,eV$) below the vacuum level. Therefore, photogenerated holes in the VB of C_3N_4 may migrate to that of $Cs_3Bi_2Br_9$ while, in turn, photo-excited electrons in $Cs_3Bi_2Br_9$ are easily transferred to the CB of C_3N_4.

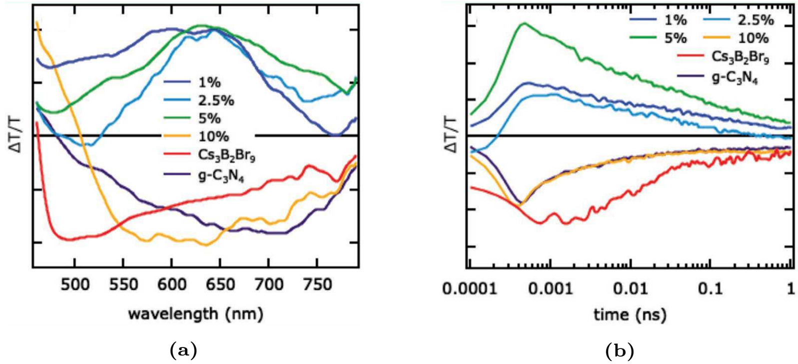

(a)

(b)

Figure 2.35. TAS of $C_3N_4/Cs_3Bi_2Br_9$ composites thin films at different percentages of perovskite loading ($\% wt$). C_3N_4 and $Cs_3Bi_2Br_9$ refer to pristine materials. a) TAS spectrum, integrated in time. b) Time decay of spectrally integrated TAS signals as a function of the pump–probe time delay (note the logarithmic time scale). $\lambda_{ex} = 345\,nm$. Reprinted with permission from ref.[145] Copyright 2021 Advanced Functional Materials.

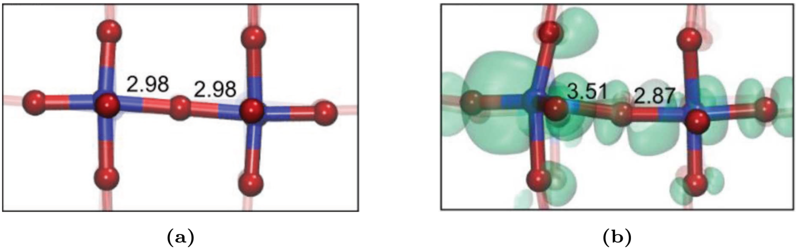

(a)

(b)

Figure 2.36. Stick & ball representation of a) neutral bulk $Cs_3Bi_2Br_9$ and b) $Cs_3Bi_2Br_9$ bearing an electron polaron. Bi atoms are given in blue and Br in red. Cs atoms are not included for ease of visualization. Isodensity representation of the electron is given in green. The z axis lies vertically. For comparison, the lengths (Å) of the Bi−Br bonds are provided. Reprinted with permission from ref.[145] Copyright 2021 Advanced Functional Materials.

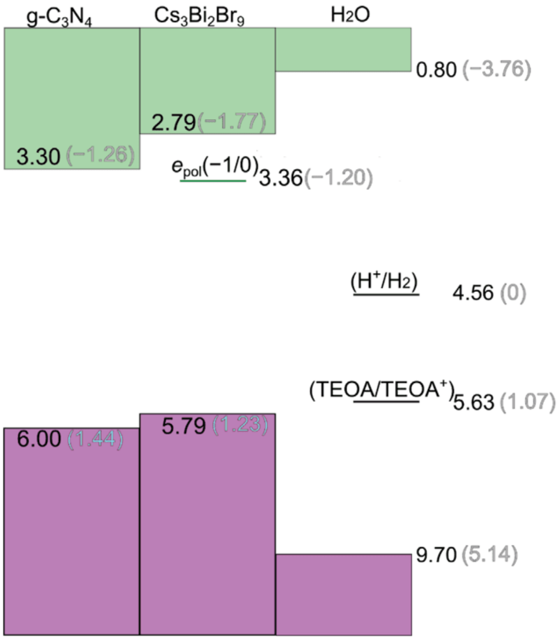

Figure 2.37. VB and CB edges of C_3N_4 and $Cs_3Bi_2Br_9$ aligned with the band edges of liquid water and with the H^+/H_2 and TEOA/TEOA$^+$ redox level (compare with ref.[12]) through the vacuum level. The (−1/0) charge transition level of the electron polaron calculated for $Cs_3Bi_2Br_9$ is also reported. Values are referred to the vacuum level (black) and to the RHE (grey) using the computational alignment achieved in ref.[148] All values are given in eV. Reprinted with permission from ref.[145] Copyright 2021 Advanced Functional Materials.

The efficient separation and transport of photoinduced electrons and holes induced by such a favourable alignment of energy levels may curb bimolecular recombination of the charge carriers, thus enhancing the photocatalytic activity of the composite with respect to the separated materials.

Nevertheless, we underline that the values reported in Figure 2.37 refer to the fundamental band gap of both materials, however, $Cs_3Bi_2Br_9$ shows a sizable exciton (see Figure 2.30b and ref.[161]) and, for this reason, photogenerated carriers within the perovskite might remain self-trapped and, therefore, not easily transferred across the composite.

Further hints suggesting this kind of behaviour are given by the emission spectra for which we observe, at higher loading of the perovskite, changes in the spectrum which are associated to the perovskite contribution. In fact, the peak at $2.59\,eV$ for $Cs_3Bi_2Br_9$ is clearly different from the $2.85eV$ value that should be expected from the fundamental band gap of the material, thus indicating that emission is occurring from a localized in-gap state.

Therefore, the calculated band alignment does not explain the bizarre trend in hydrogen evolution rates as a function of the different $Cs_3Bi_2Br_9$ loading in the composite (Figure 2.32a), nor the shift observed in the absorption and in the emission spectra upon composite loading (Figure 2.30b).

To solve this dilemma, we investigate the possible occurrence of hole and electron polarons by combining electronic structure calculations with a canonical formulation of defect in semiconductors. In fact, the $Cs_3Bi_2Br_9$ exciton might evolve into separate small hole and electron polarons (i.e., self-trapped excitons), as previously observed for both Bi-based semiconductors and layered perovskites,[58, 161, 172–174] for instance, localization of photogenerated holes onto a bromide dimer (so called V-centre defect typical of metal halides) has been suggested by a recent study.[175–177]

We first investigated hole polaron formation and verified that self-hole trapping on a Bi-bridging Br_2-dimer should be ruled out as it is energetically unfavoured. Therefore, the hole transfer across the composite is favourable (see Figure 2.37) and no trapping in the perovskite is envisaged, thus ensuring that charge losses are avoided.

In stark contrast, upon injection of a single electron in bulk $Cs_3Bi_2Br_9$, we observe strong localization of the charge around a Bi atom, i.e., self-electron trapping, which is associated with a sizable rearrangement of the local structure, as shown in Figure 2.36. In the charged system, the electron is found to localize upon distortion of a ${BiBr_6}^{3-}$ subunit: in particular, the distortion brings a substantial increase in the Bi−Br bond length for the Br atom bridging two adjacent ${BiBr_6}^{3-}$ (from 2.98 to 3.51 $\AA$, see Figure 2.36).

We calculated a binding energy of $0.59\,eV$ for this polaronic state, thus further demonstrating that the small polaron may act as a deep trap in the gap of $Cs_3Bi_2Br_9$. The associated $(-1/0)$ charge transition level (see Figure 2.37) is found to lie $3.36eV$ below the vacuum level and entails an energy gap of $2.43\,eV$, which is consistent with the low-energy emission measured for the perovskite and for the composites at high $\%\,wt$ loading.

Overall, self-trapping of the photogenerated electrons can explain the unsatisfactory performances of composites featuring a perovskite loading $> 5\%\,wt$, for which we observe a very limited enhancement of the hydrogen production with respect to the separated materials. In this sense, we also note that, TAS measurements, which indicate a broadband photoinduced absorption for the perovskite, typically associated with self-trapped excitons, are consistent with the proposed physical model, resulting in the loss of any synergic enhancement of hydrogen production. In accordance with this, the absence of any spectroscopic signature of $Cs_3Bi_2Br_9$ for low-loading composites coupled with the high hydrogen production yield, suggests that charge trapping in the perovskite might be avoided in this case.

Since photo-excitation of $Cs_3Bi_2Br_9$ could not result in electron transfer from its fundamental CB to that of C_3N_4 because of the strong exciton, a possible direct excitation mechanism, e.g., from VB to C_3N_4 CB may be operative for small $Cs_3Bi_2Br_9$ particles dispersed on the C_3N_4 surface or among its layers, thus bypassing charge localization, in line with what has been previously observed in dye-sensitized solar cells or in plasmonic photo-catalytic composites.[177,178]

In this case, TAS measurements also suggest the possible occurrence of new localized in-gap states at the complex $C_3N_4/Cs_3Bi_2Br_9$ interface, that may act as catalytic sites, thus further motivating the observed boost in hydrogen production.

Conclusions

In the present paper, we reported the design of catalytically active composites based on the coupling between $Cs_3Bi_2Br_9$ and C_3N_4 to create a heterojunction where the energy levels alignment between the two semiconductors provides an effective improvement of photoactivity.

The samples have been tested for the hydrogen evolution reaction and organic dye degradation identifying the optimal amount of $Cs_3Bi_2Br_9$ in the composite, namely $2.5\%\,wt$. The synergic effect allows an increase of photogenerated H_2 from $\approx 81\,\mu mol\,g^{-1}\,h^{-1}$ of pure C_3N_4 to $\approx 1050\,\mu mol\,g^{-1}\,h^{-1}$ for the $C_3N_4/Cs_3Bi_2Br_9$ $2.5\%\,wt$ composite. The latter resulted also to be significantly more active in MB degradation with respect to pure carbon nitride.

Steady state and ultrafast transient spectroscopical investigations suggest a peculiar charge dynamic in these systems influenced by the perovskite loading. Low levels of perovskite inclusion act both on curing C_3N_4 material defects and on funnelling the charges upon localized states. Those active sites could be fundamental in boosting the photo-catalytic performances of low loading composites.

Advanced computational modelling further adds to the rationale behind the microscopic mechanism favouring an efficient charge separation in the composite and, in addition, provides a clue to understand the optical investigation outputs and the trend of HER as a function of perovskite amount.

Chapter 3

Development of the Photoelectrodes

In this chapter the deposition of the materials in the form of films will be described, starting from the anodes and continuing with the cathodes, along with their optimization and their physical and photo-electrochemical characterization.

For all the samples, Fluorine doped Tin Oxide (FTO) glass was used as substrate in order to allow irradiation of the samples from the back during the photo-electrochemical characterization.

This requirement may seem unimportant during the characterization of the half-cells, as the working electrodes (both anodes and cathodes) are tested against the standard counter electrode and could be illuminated from the front side of the electrode; however, due to the geometry of the adopted cell, it becomes essential during the characterization of a complete cell (that will be discussed in the next chapter), in which no standard counter electrode is employed as the developed anodes and cathodes are tested against each other.

For all the photo-electrochemical characterizations a cell with fixed-photoelectrode-area was used. In this kind of cell (a generic sketch of which is represented in Figure 3.1) the electrode is placed outside the vessel against a fixed-area opening to guarantee contact with the electrolyte.

Concerning the other experimental conditions, a wire of platinum was used as counter electrode, an Ag/AgCl electrode was used as reference and two kinds of electrolytes were employed; for the CV a 1 M aqueous solution of Na_2SO_4 was used, while for the CRA measures glucose was added (with a concentration of 0.4 M) as sacrificial agent, in order to emphasize the differences in the performances of the various electrodes. The choice of the sacrificial agent fell on glucose as it could also prove to simulate a biomass-containing water, as was already discussed in Paragraph 2.2.[79]

A LED solar simulator, that emits a calibrated *AM 1.5G* spectrum, was employed as light source.

The photo-electrochemical testing of the samples consisted of three kinds of measures:

Open Circuit Voltage readings, these measures were aimed to register the potential naturally reached by the working electrodes in contact with the electrolyte, and evaluate which samples are more suitable for achievement of a photo-electrocatalytic cell that works only through an internal bias;

Cyclic Voltammetry, although they do not in any way represent the actual working conditions, these kinds of measures were employed in order to both identify the actual range of potentials at which the materials become active as catalysts and to verify which samples develop the higher electric current at said potential.

Measures were performed at different scan rates, the choice of which was based on the data found in literature; in particular, while the lower scan rates are closer to the actual working conditions, the higher ones served as an accelerated degradation test;[1]

Constant-potential Chronoamperometric readings, these measures were used in order to simulate the actual working conditions, by means of imposition of a constant potential on the working electrode and monitoring of the evolved electric current; the artificial imposition of the potential was a necessary means in order to reach the working voltage as the materials per se were not able to develop the potential necessary for the realisation of a cell only internally biased.

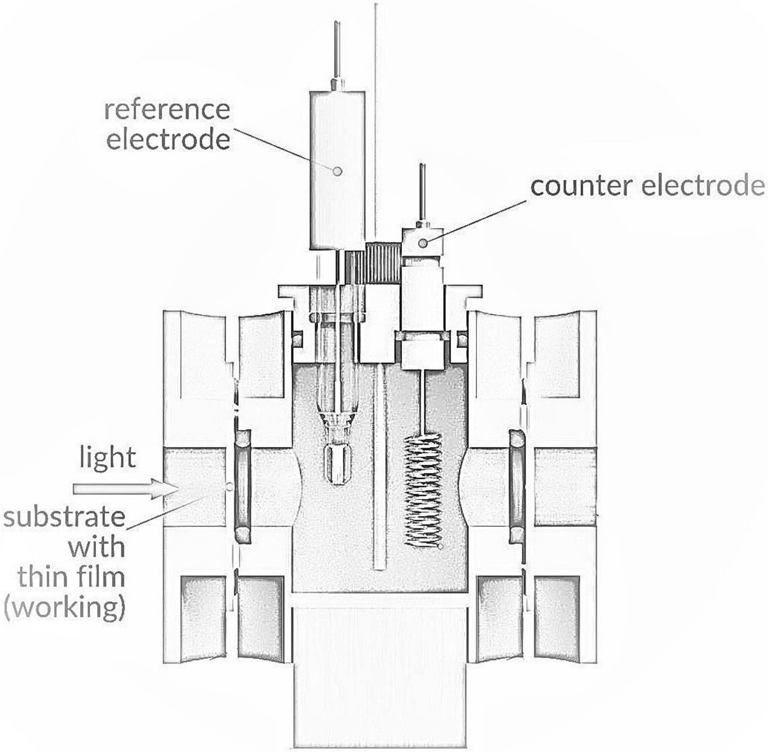

Figure 3.1. Schematic representation of the photo-electrochemical cell employed.

These measures were performed only on a selection of the samples, the choice of which will be explained in the following paragraphs.

For ease of interpretation of the photo-electrochemical results, the graphs will report only a part of the data, that will be selected in order to highlight the differences between the performances of the samples:

- for OCV readings, only the curves of one representative sample will be plotted, in order to highlight the difference of behaviour of the material in the dark and under illumination.

  The data of all the other samples will be summarized in an appended table;
- for CV curves, only one cycle per curve will be plotted, and the plotted curves will be selected in order to illustrate the various trends that were identified between the measures;
- for CRA measures, the curves will be plotted in their entirety, and the area considered for the quantification of evolved hydrogen and/or oxygen will be highlighted.

Due to the difficulty in the interface between the employed cell and a GC analyser the quantification of the evolved gas was based on the amount of the developed current, that is directly related to the number of exchanged electrons.

3.1 Anodes

$BiVO_4$

As was previously described, layers of bismuth vanadate were directly synthetized on the surface of the electrode substrates via a combustion synthesis.[29]

Morphological Characteristics

The quick nucleation that occurs when employing this kind of synthesis causes the material to be made up of micrometric grouped particles, instead of a continuous layer, as can be seen from the SEM images in Figure 3.2 (the smaller particulate that can be seen in the background is part of the crystalline substrate).

Photo-Electrochemical Characterization

The photo-electrochemical characterizations were aimed not only to determine the intrinsic performances of the material as a photo-electrocatalyst, but also the influence on them of the amount of material deposited onto the electrode.

For this reason, samples were prepared using same quantities of precursor-solutions but with two different concentrations, with one concentration double than the other one; they are listed in Table 3.1.

From the OCV curves the effect of illumination can be clearly seen, as the measures conducted in this condition gave potentials considerably more negative than the ones conducted in the dark, as depicted by the curves and the data reported in Figure 3.5 and Table 3.2.

The second effect that was noted is that, even though the two samples are made of the same material, the one prepared with the more concentrated precursor always developed a more negative potential when compared to the other sample. The reason behind this effect is not clear, however it was not further investigated.

When looking at the CV curves, represented in Figures 3.6-3.7, and, in particular, at the peak of current at $-1.5\,V$, that is the voltage at which the oxygen evolution reaction occurs, a few characteristics were highlighted:

- the effect of illumination is seen when comparing the electric current evolved when the measure was conducted in the dark and under irradiation;
- the electric current registered with the different scan rate is always very similar, with a slight increase at the higher scan rates;

Table 3.1. List of the characterized samples.

Label	**Sample**	**Description**
A-1.1	$BiVO_4$	diluted precursor
A-1.2	$BiVO_4$	concentrated precursor

- in the same experimental conditions, the sample prepared with the more concentrated precursor developed a higher electric current.

On the other hand, the large peak registered at $\approx -0.8\,V$ is presumably caused by the reduction of the $SO_4{}^{2-}$ anion, the standard reduction potential of which is $E^0\left(SO_4^{2-}/SO_3^{2-}\right) = -0.93\,V$.[179]

Another unfortunate effect that was noted is that the material underwent some degradation, that caused it to obviously change colour, as can be seen from the comparison of the photographs in Figure 3.8.

Following these characterizations, despite the manifest degradation, the sample prepared with the more concentrated precursor, that had developed both the higher voltage and current peak, was selected to undergo the CRA measure, so that it could be used as reference for the subsequent materials.

From the CRA curve, represented in Figure 3.9, it can be said that the sample developed a discreet amount of electric current, that can be related to the amount of evolved oxygen through the equation:

$$n\left(O_2\right) = \frac{\int\limits_{t_1}^{t_2} i\left(t\right)\,dt}{4Q_eN_A} \tag{3.1}$$

where: $n\left(O_2\right)$ is the amount of oxygen evolved, expressed in (mol); $i\left(t\right)$ is the registered electrical current, expressed as a function of time; Q_e is the charge of the electron; N_A is the number of Avogadro; and 4 is a coefficient derived from the stoichiometry of the reaction.

The calculation was performed on the curve beyond $1000\,s$ in order to avoid consideration of the initial peak of electric current, caused by the sudden imposition of the working voltage, that may lead to a misleading value.

This calculation led to an Oxygen Evolution Rate (OER) value of $5.35 \cdot 10^{-6}\,mol\,h^{-1}\,cm^{-2}$.

Structural and Morphological Characterization of the Degraded Sample

Due to the evident degradation, structural and morphological characterization was performed again on the tested sample.

Nonetheless, from the comparison of the SEM images of the pristine sample, in Figure 3.2, and those of the sample subjected to the CRA measure, represented in Figure 3.3, no great difference was noted in the morphology of the two samples. On the other hand, the EDS analysis evidenced a loss of bismuth and vanadium in the global composition of the sample, and a change in the bismuth/vanadium ratio, as can be seen from the comparison of the charts in Figure 3.4.

However, conclusive evidence on the exact composition of the tested sample could not be obtained, since the XRD analysis, represented in Figure 3.10, only highlighted the appearance of a single peak (at $\approx 27°$) in the diffraction pattern of the sample, compared to the one of the pristine sample.

Protection of the Anodic Material

Further optimization of the electrode was performed only on the samples prepared with the concentrated precursor.

In order to prevent the degradation of the bismuth vanadate during the catalytic process, the already-prepared electrodes were later covered with a layer of polyethyleneimine (PEI).[180] The deposition of the polymeric layer was achieved through the drop casting of an aqueous dispersion of the polymer, followed by a thermal annealing of the sample (at 150 °C for $10\,min$).

The samples thus prepared were tested in the same way as the previous ones.

From the OCV readings it can be seen that the response to light was not tarnished, also when compared to the uncoated sample the potential developed was more negative, presumably due to a favourable effect of the polymer itself.

On the other hand, the CV curves show that the protected sample developed a smaller amount of electric current, as one could expect from the insertion of an additional layer between the active material and the reactive specie; in any case, the drop in electric current is not so critical as to make the use of the electrode meaningless.

On this protected sample the CRA measure was also performed. The coated sample, again, developed a smaller amount of electric current, however the damage to the material was greatly reduced, as can be seen from the photographs in Figure 3.12.

The calculation of the OER gave a value of $3.68 \cdot 10^{-6}\, mol\, h^{-1}\, cm^{-2}$; this value is only $\approx 70\%$ of the one reached by the unprotected sample, however, in our view, the improved stability was enough to justify the adoption of the practice of coating the $BiVO_4$-based electrodes.

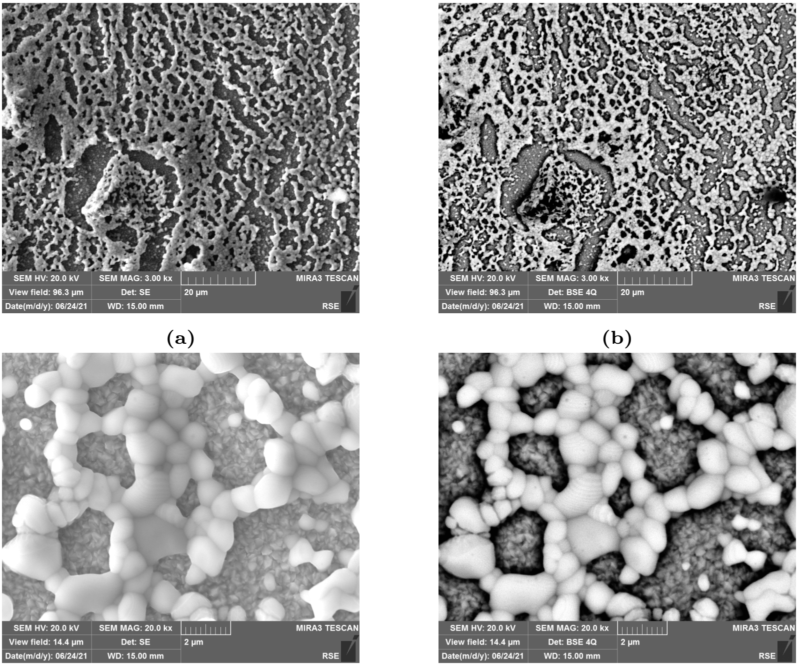

(a) **(b)**

(c) **(d)**

Figure 3.2. a,c) Secondary Electrons- and b,d) Back Scattered Electrons-SEM images of the A-1.2 pristine sample, at two different magnifications.

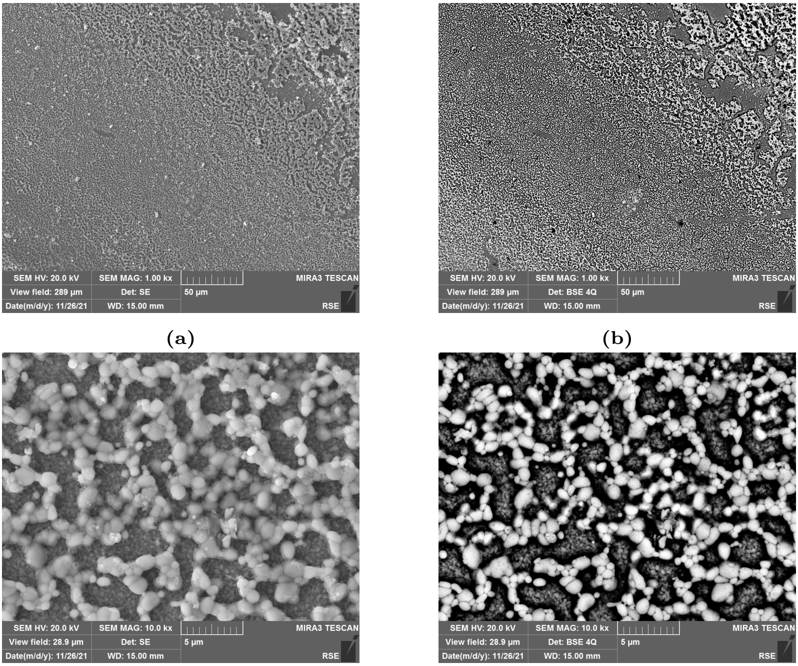

(a) (b)

(c) (d)

Figure 3.3. a,c) Secondary Electrons- and b,d) Back Scattered Electrons-SEM images of the A-1.2 sample subjected to CRA measure, at two different magnifications.

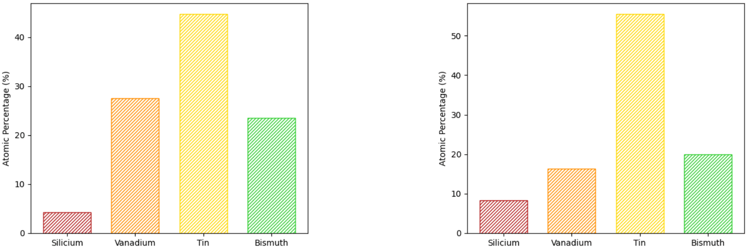

(a) (b)

Figure 3.4. EDS analysis of the A-1.2 sample, a) pristine and b) subjected to CRA measure.

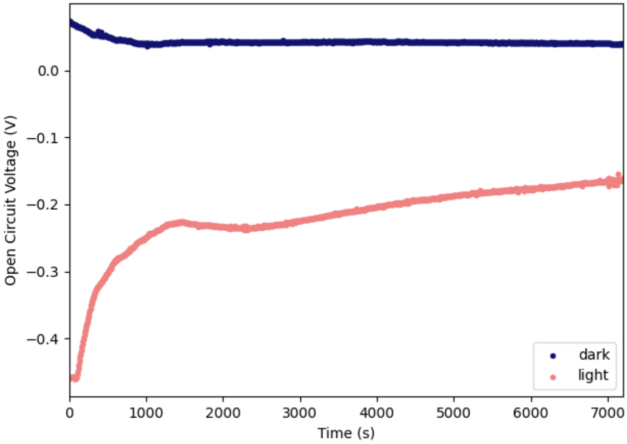

Figure 3.5. OCV reading of the A-1.2 sample.

Table 3.2. OCV values reached by each sample in the two conditions after $2\,h$ of reading.

Label	**OCV - in dark** $(\boldsymbol{mV})$	**OCV - in light** $(\boldsymbol{mV})$
A-1.1	-48	-142
A-1.2	39	-164

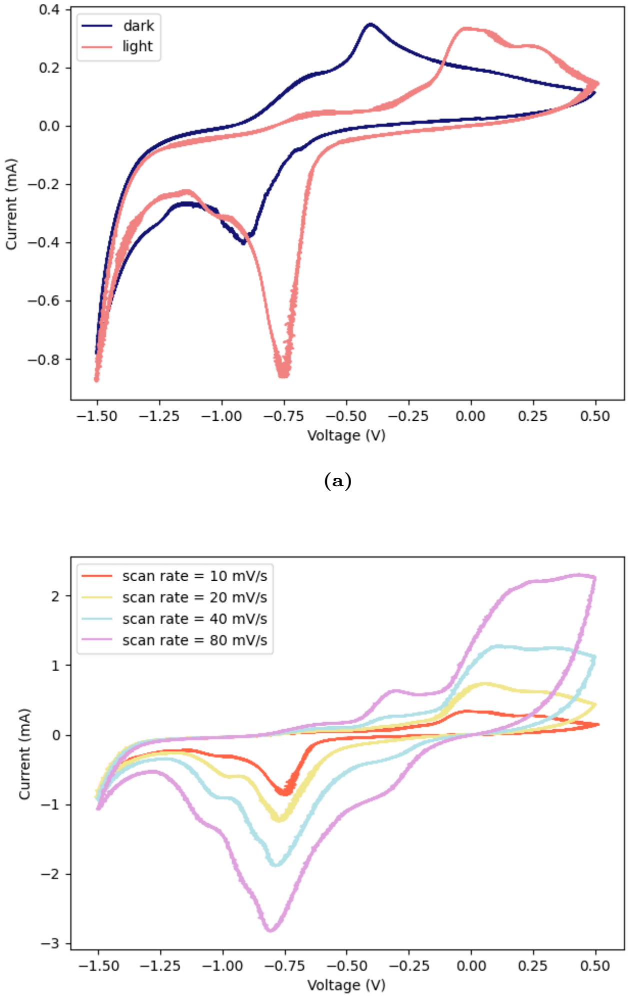

(a)

(b)

Figure 3.6. CV of the A-1.2 sample, comparison between the measures performed a) in the dark and under illumination, at $10\,mV\,s^{-1}$, b) at different scan rates, under illumination.

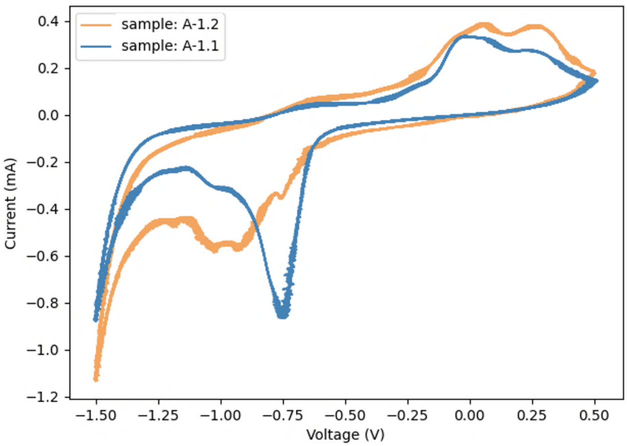

Figure 3.7. Comparison between the CV measures of the A-1.1 and A-1.2 samples, performed at $10\, mV\, s^{-1}$ under illumination.

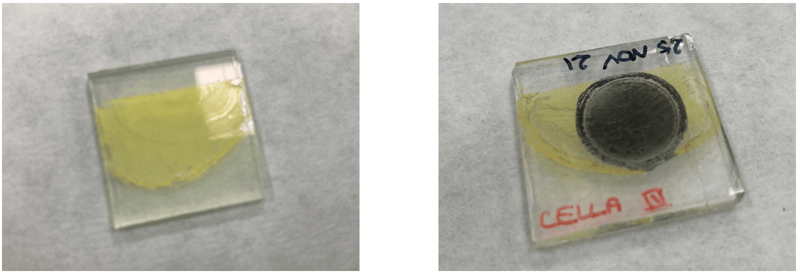

(a) **(b)**

Figure 3.8. Photographs of the samples a) pristine and b) after CV.

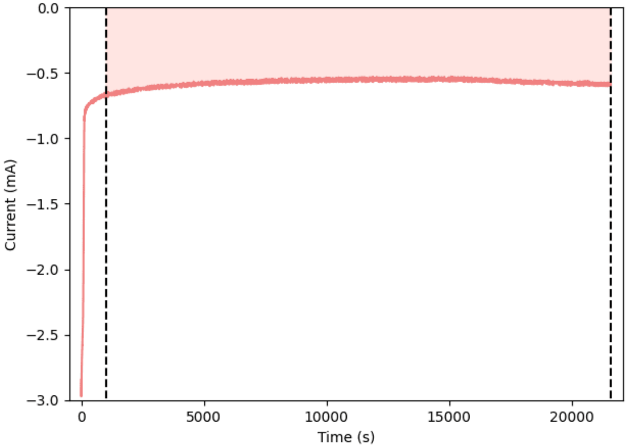

Figure 3.9. CRA measure of the A-1.2 sample, the area considered for OER calculation is highlighted.

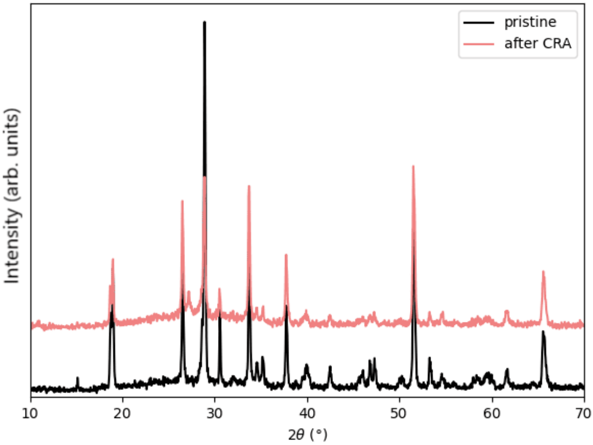

Figure 3.10. Comparison between the XRD patterns of the A-1.2 sample, pristine and after CRA.

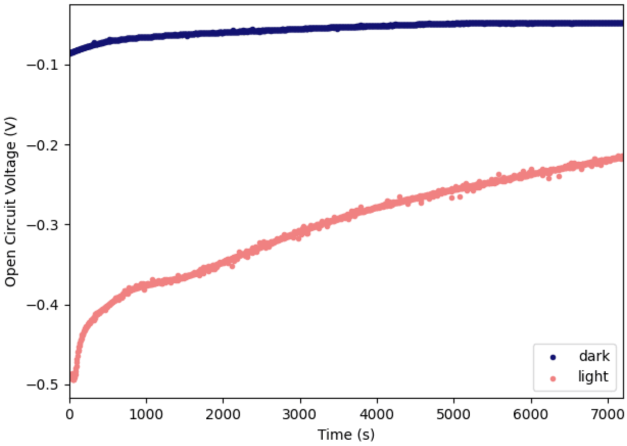

Figure 3.11. OCV readings of the A-1.2-PEI sample.

Table 3.3. OCV values reached by the samples after $2\,h$ of reading.

Label	**OCV - in dark ($\boldsymbol{mV}$)**	**OCV - in light ($\boldsymbol{mV}$)**
A-1.2	39	−164
A-1.2-PEI	−48	−215

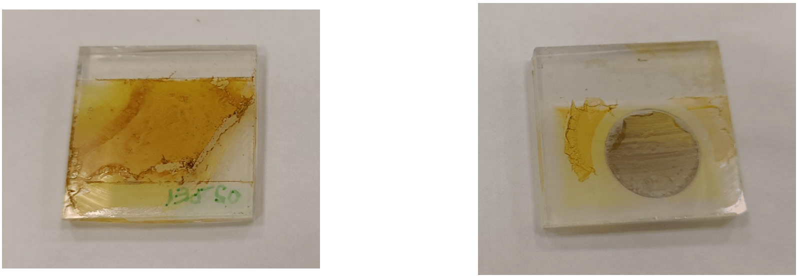
(a)

(b)

Figure 3.12. Photographs of the samples a) pristine and b) after CRA.

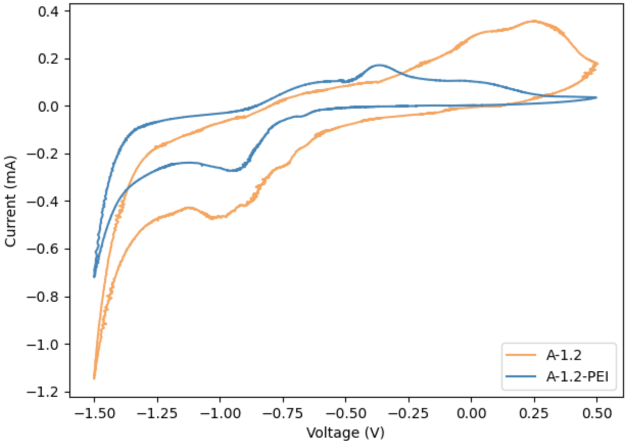

Figure 3.13. Comparison between the CV curves of the A-1.2 and A-1.2-PEI sample.

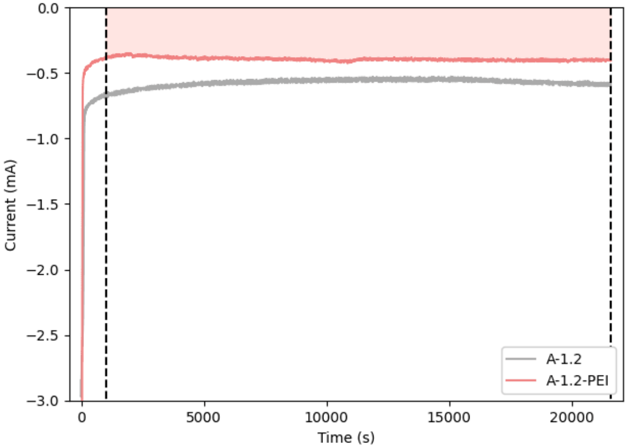

Figure 3.14. Comparison between the CRA measures of the A-1.2 and A-1.2-PEI samples, the area considered for OER calculation is highlighted.

$BiVO_4$ / TiO_2 system

For the further step of the optimization of the electrodes, a second material was added to the bismuth vanadate, namely titanium dioxide, in order to enhance the separation of the photogenerated charges, with a mechanism similar to that observed for the cathodic materials.

For the deposition of the composite material, two different kinds of nanometric powders of titanium dioxide were added in very different quantities to the bismuth vanadate precursor, and this suspension was homogenized and drop casted directly onto the FTO substrates to undergo the combustion-reaction synthesis; a list of the characterized samples can be found in Table 3.4.

The two kinds of titanium dioxide mainly differ in the amount of anatase and rutile relative content, as the first powder was the commercial Evonik Aeroxide P25 (from now on it will be referred to as "TiO_2-P25") while the second one was made of smaller particles and contained a lower amount of rutile (the powder was synthesized by Dr. Maurizio Notaro of RSE S.p.A. and it was kindly provided for the experimentation, from now on it will be referred to as "TiO_2-MN"). The XRD patterns of both titanium dioxide powders are represented in Figure 3.15 (a Rietveld analysis of the experimental patterns revealed that TiO_2-P25 contained 12.80% while TiO_2-MN only contained 5.56% of rutile).

These samples were directly prepared with the polymeric protection, due to the previous experience on the bismuth vanadate monophasic samples.

Table 3.4. List of the characterized samples.

Label	Sample	Amount of TiO_2 relative to $BiVO_4$
A-2.1	$BiVO_4$/TiO_2-P25-PEI	10% *mol*
A-2.2	$BiVO_4$/TiO_2-P25-PEI	50% *mol*
A-2.3	$BiVO_4$/TiO_2-P25-PEI	200% *mol*
A-3.1	$BiVO_4$/TiO_2-MN-PEI	10% *mol*
A-3.2	$BiVO_4$/TiO_2-MN-PEI	50% *mol*
A-3.3	$BiVO_4$/TiO_2-MN-PEI	200% *mol*

All samples were prepared with the concentrated $BiVO_4$ precursor

Structural Characteristics

Through the XRD analysis (the patterns of two representative samples are reported in Figure 3.15) it could be verified that composite materials made of bismuth vanadate and titanium dioxide were deposited on the electrodes.

However, it was noticed that the ratio of anatase to rutile phase changed during the deposition of the materials, compared to the starting powders, as the amount of rutile increased; this effect is particularly evident in the samples containing the TiO_2-MN titanium dioxide, rather than the TiO_2-P25 one, as in the pristine material the rutile phase was almost absent.

Morphological Characteristics

From the SEM images, represented in Figures 3.17a-3.17d and Figures 3.18a-3.18d, it can be seen that the morphology of these samples resembles the one of the previous ones, as the material is again formed by small and grouped micrometric particles; however, these ones are much smaller compared with the ones of the bismuth vanadate electrodes.

The SEM images, especially those at higher magnification, may appear not very clear, however this is due to the polymeric layer that blurs the details of the morphologies.

Photo-Electrochemical Characterization

From the OCV curves a couple effects were observed, apart from illumination, as depicted by the curves and the data reported in Figure 3.19 and Table 3.5, when exposed to light:

- the OCVs of the samples with TiO_2-P25 titanium dioxide seems to be less dependent on the amount of titanium dioxide incorporated, compared with those of the samples with TiO_2-MN;
- comparing the OCVs of the samples with the same amount of titanium dioxide, those of the samples with TiO_2-P25 are generally more negative than those of the ones with TiO_2-MN;
- both for TiO_2-P25 and TiO_2-MN, the sample that developed the more negative OCV was the one with medium quantity of incorporated titanium dioxide.

Comparing the CV curves of the samples, represented in Figures 3.20-3.21, it was noted that:

- the effect of illumination is easily identifiable from the amount of electric current evolved;
- the electric current registered with the different scan rate is very similar for all the samples with TiO_2-P25, while it increases together with the amount of titanium dioxide for the sample with TiO_2-MN;
- under the same experimental conditions, the samples prepared with different quantities of the same kind of titanium dioxide developed very similar electric currents, both for TiO_2-P25 and TiO_2-MN;
- under the same experimental conditions, samples prepared with same quantities of the two kinds of titanium dioxide developed very similar electric currents.

Following these characterizations, since no dramatic difference was highlighted in the electric current developed by each electrode, the two samples with medium quantity of titanium dioxide were selected to undergo the CRA measure due to the more negative values of OCV they reached, in fact more importance was given to the values of developed voltage rather than to the intensity of the current peaks.

Comparing the CRA curves of the two samples, represented in Figure 3.22, with that of the sample without titanium dioxide (Figure 3.9) it can be seen that:

- both electrodes developed a higher electric current;
- while the curves of the two samples reach similar values, the one of the sample with TiO_2-MN is slightly more negative than the other.

Equation 3.1 was employed to calculate the OERs for the two samples; they reflect the observations made on the CRA curves and are summarized in Table 3.6.

Morphological Characterization of the Tested Samples

Morphological characterization was performed again on the tested samples.

For both samples, from the comparison between the SEM images of the pristine and tested samples (respectively Figures 3.17a-3.17d against Figures 3.17e-3.17f, and Figures 3.18a-3.18d against Figures 3.18e-3.18f) the active material, i.e., the grains of mixed bismuth vanadate/titanium dioxide, does not appear to have been damaged as it retained its fine morphology.

However, the polymeric coating is not as intact:

- for the sample with TiO_2-P25 titanium dioxide, the PEI layer started to furrow, and at some points some small cuts also appeared;
- for the sample with TiO_2-MN titanium dioxide, the PEI layer did not start to wrinkle yet, however some more and less thick spots could be pinpointed from the images registered with backscattered electrons; that is presumably the step before the actual formation of the wrinkles.

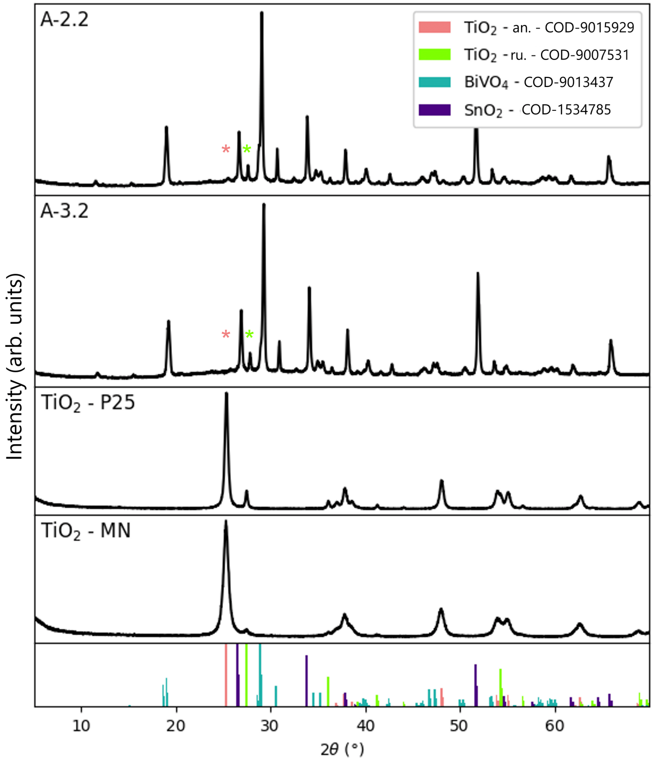

Figure 3.15. In order, experimental XRD patterns of the A-2.2 and A-3.2 samples (the position of the main peaks of anatase and rutile are highlighted by asterisks) and of the TiO_2-P25 and TiO_2-MN titanium dioxides, reference patterns of the active materials and of the crystalline substrate.

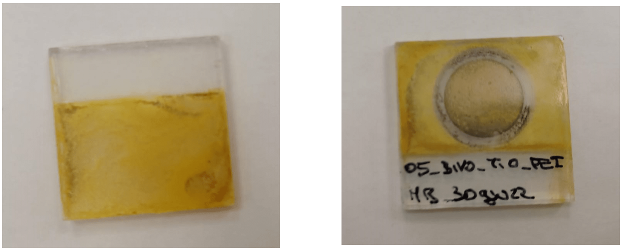

(a) **(b)**

Figure 3.16. Photographs of the samples a) pristine and b) after CRA.

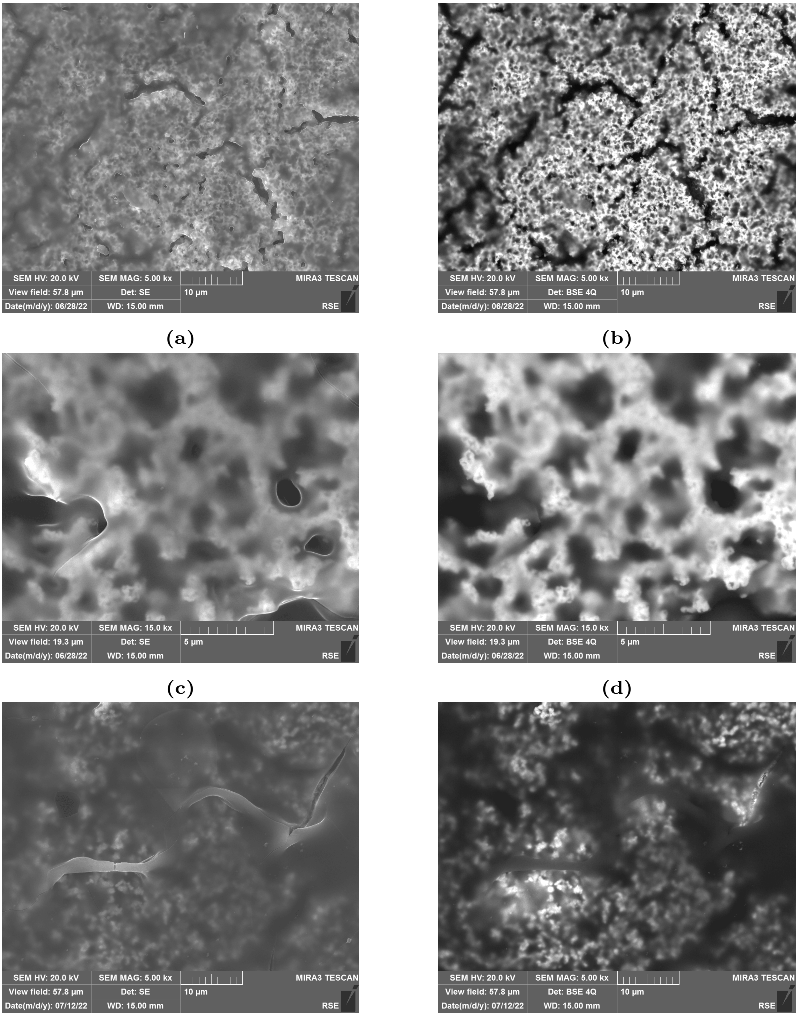

(a) **(b)**

(c) **(d)**

(e) **(f)**

Figure 3.17. a,c) Secondary Electrons- and b,d) Back Scattered Electrons- SEM images of the A-2.2 pristine sample, at two different magnifications. e) Secondary Electrons- and f) Back Scattered Electrons- SEM images of the A-2.2 sample subjected to CRA measure.

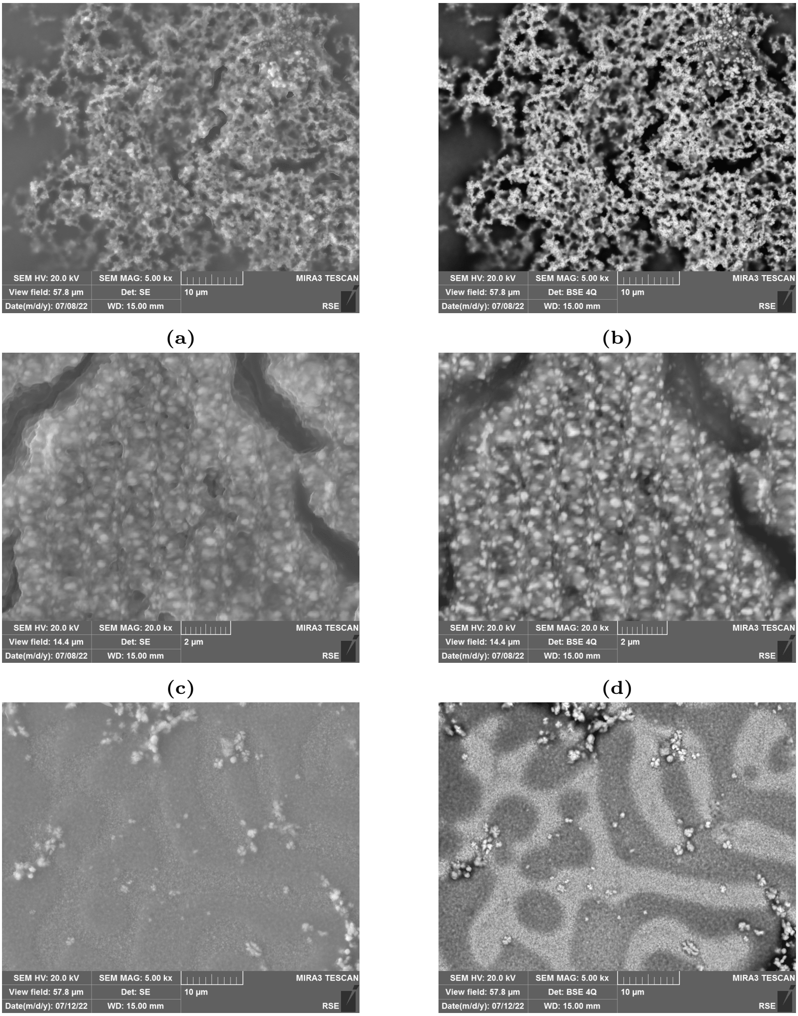

(a) **(b)** **(c)** **(d)** **(e)** **(f)**

Figure 3.18. a,c) Secondary Electrons- and b,d) Back Scattered Electrons- SEM images of the A-3.2 pristine sample, at two different magnifications. e) Secondary Electrons- and f) Back Scattered Electrons- SEM images of the A-3.2 sample subjected to CRA measure.

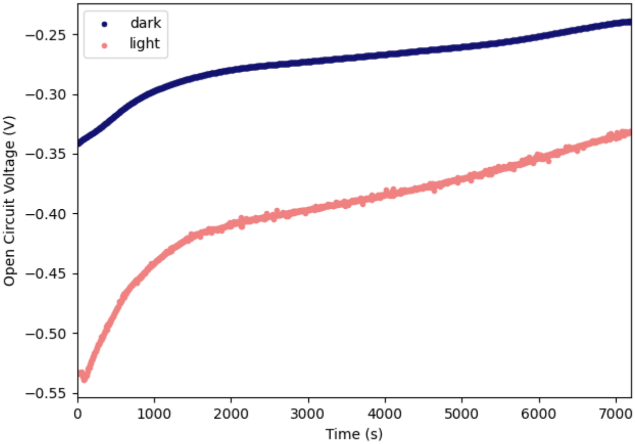

Figure 3.19. OCV reading of the A-2.2 sample.

Table 3.5. OCV values reached by each sample in the two conditions after 2 h of reading.

Label	**OCV - in dark (mV)**	**OCV - in light (mV)**
A-2.1	−205	−300
A-2.2	−239	−332
A-2.3	−320	−302
A-3.1	−140	−258
A-3.2	−275	−304
A-3.3	−22	−122

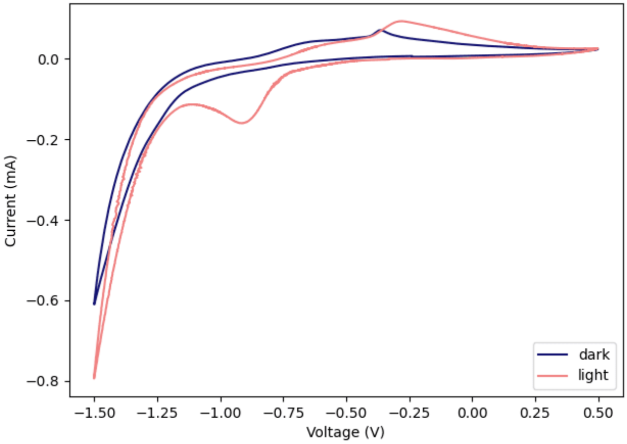

(a)

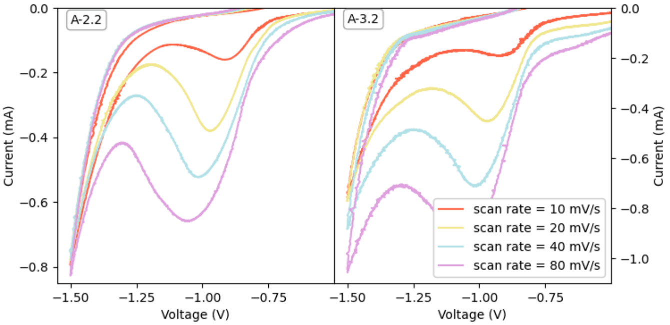

(b)

Figure 3.20. CV of the samples, comparison between the measures performed a) in the dark and under illumination, at 10 $mV\ s^{-1}$, for the A-2.2 sample and b) at different scan rates, under illumination, for the A-2.2 and A-3.2 samples.

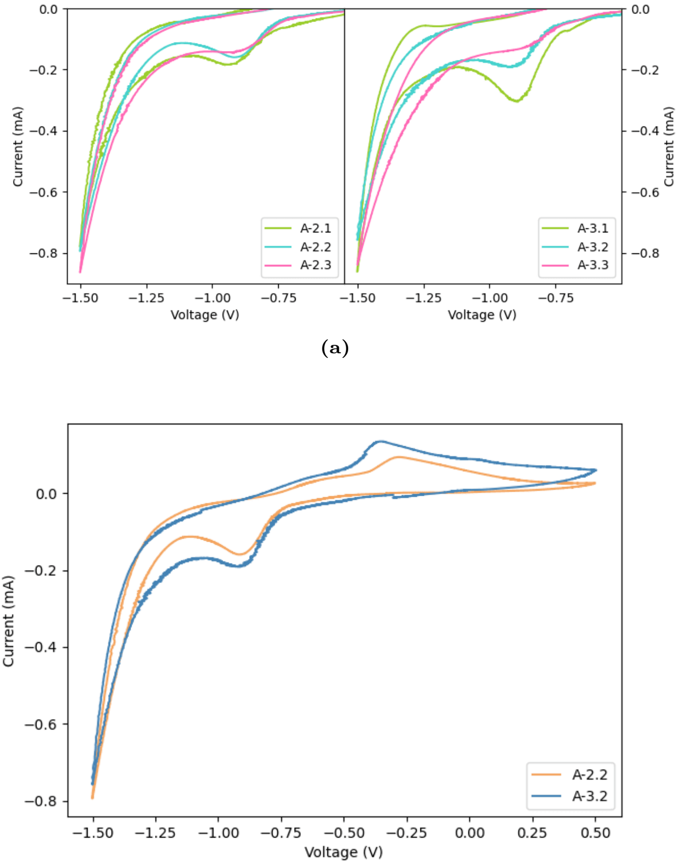

(a)

(b)

Figure 3.21. Comparison between the CV of the samples: a) with different amounts of TiO_2, b) with different types and equal amounts of TiO_2.

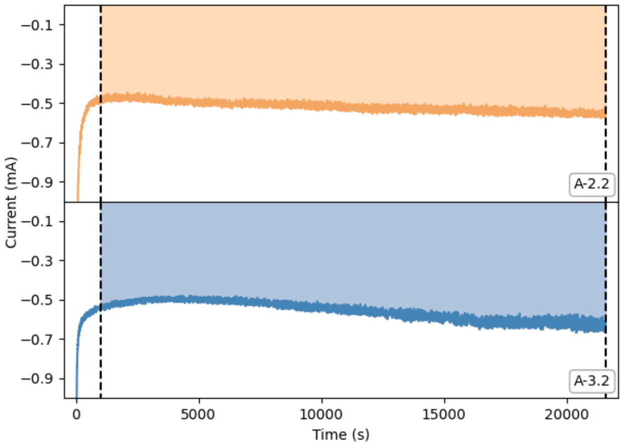

Figure 3.22. CRA measures of the A-2.2 and A-3.2 samples, the areas considered for OER calculation are highlighted.

Table 3.6. OER values of the characterized samples.

Label	**Oxygen Evolution Rate** $(mol\, h^{-1}\, cm^{-2})$
A-1.2-PEI	$3.68 \cdot 10^{-6}$
A-2.2	$4.82 \cdot 10^{-6}$
A-3.2	$5.20 \cdot 10^{-6}$

3.2 Cathodes

The data obtained from the catalysis tests from aqueous suspensions, that were described in the previous chapter, were taken into account to select the compositions of the catalysts employed for the assembling of the electrodes, said samples are listed in Tables 3.7, 3.10, 3.13.

Some of these photo-electrochemical characterizations were actually the first that were performed; due to a difficulty in procuring a suitable solar simulator, the first preliminary characterizations were conducted using a halogen lamp as light source; however, due to the evident degradation of the samples such measures have not been replicated with the solar simulator.

These measures are the OCV readings and CV of C_3N_4 and $C_3N_4/Cs_3Bi_2Br_9$ electrodes with Nafion binder.

g-C_3N_4

After having correctly reproduced the synthesis of C_3N_4 (Paragraph 2.2) and having verified its physical and functional properties, focus was put on its deposition in the form of film.

In the literature a few deposition methods are reported, they are basically divided in:[181, 182]

post-processing methods, that consist in a multi-step route which begins with the synthesis of C_3N_4 powder; the second step can be either the coating of the substrate with a C_3N_4-containing slurry (this is often achieved through tape casting, spin coating, drop casting or dip casting) or the self-assembly of the C_3N_4 particulate contained in a colloidal solution (this can be achieved through vacuum filtration, for the formation of a membrane, or interfacial self-assembly/transfer, for the formation of a supported film);

direct-growth methods, that involve the synthesis of the material directly on the surface of the substrate; the methods are various and span from thermal vapor condensation to micro-contact-printing to solvothermal to direct-contact thermal polymerization.

Vapor Phase Deposition (VPD)

At first it was chosen to adopt a deposition from vapor phase, employing the same kind of synthesis used for the bulk material, with the optimization of some experimental parameters.

In this case, the FTO substrate was placed in the reaction vessel along with the organic precursor, and care was placed on the use of slower heating and cooling ramps in order to avoid damage to the glass substrate due to a thermal shock.

The XRD analysis on these kinds of samples, in which the active material is poorly crystalline, composed of light elements and deposited on top of a crystalline substrate containing a metal as heavy as tin, is hardly useful, as can be seen from the patterns in Figure 3.23.

More significant was the UV-Vis absorption spectrum, reported in Figure 3.24, in which an absorption edge is visible in correspondence of the absorption edge of C_3N_4. The interpretation of the spectrum may prove difficult due to the background modulation that appears at higher wavelength, that is caused by interference during the interaction between the radiation and the film. Such an effect was also observed in the analysis of other kinds of samples.

After the successful deposition, the first electrochemical characterisations were performed; however, at this stage a critical flaw emerged, that is a lack of adhesion of the material to the substrate caused by the electric current flow that is believed to induce an interfacial tension which then caused the detachment that can be observed in the SEM images in Figure 3.25.

Drop Casting Deposition

The deposition method that was later adopted consists in the drop casting of a mixture of the catalyst, in the form of powder, and a polymeric binder that allows it to adhere to the substrate.[183–185]

Following the papers that were used as reference,[183–185] Nafion was the first chosen polymer; this is due to the fact that it is a hydrogen-ions-conductor and thus should favour the contact between the catalyst and the active specie.

Compared to the reference deposition method,[183] the only optimized parameter was the amount of catalyst included in the precursor suspension, that was considerably reduced in order to create thinner layers and favour the electric current flow.

During the experimentation, while the deposition method basically always remained the same, some adjustments (apart from the different co-catalysts that were studied) were made, that allowed the characteristics of the samples to develop:

- at first the normal bulk-C_3N_4 was used as basis for the powdered catalysts;
- as was mentioned in Paragraph 2.2, later, thermally exfoliated-C_3N_4 and Ca included-C_3N_4 were employed;
- it was also tested a different polymeric binder, namely PEDOT:PSS, that is an electric conductor widely known in the MHPs photovoltaic field.[186–189]

All the characterizations will be described in the following sections, gathering together the results of similar samples.

As was done for the anodes, samples were made by depositing two different quantities of precursor in order to verify an eventual effect on the performance of the electrodes; the characterized samples are summarized in Table 3.7.

Morphological and Optical Characteristics

As was mentioned previously, XRD analysis on these kinds of samples is not helpful, while some observations can be made on the UV-Vis absorption spectra, that can be seen in Figure 3.26:

- the absorption profile of the samples with Nafion and PEDOT:PSS as binders fairly resembles the profile of the C_3N_4

Table 3.7. List of the characterized samples.

Label	Sample	Binder	Description
C-1.1	bulk C_3N_4	Nafion	diluted sample
C-1.2	bulk C_3N_4	Nafion	concentrated sample
C-2.1	exfoliated C_3N_4	Nafion	diluted sample
C-2.2	exfoliated C_3N_4	Nafion	concentrated sample
C-3.1	exfoliated C_3N_4	PEDOT:PSS	diluted sample
C-3.2	exfoliated C_3N_4	PEDOT:PSS	concentrated sample
C-4.1	Ca included-C_3N_4	PEDOT:PSS	diluted sample
C-4.2	Ca included-C_3N_4	PEDOT:PSS	concentrated sample

powder, sign of the fact that the material is stable in ambient conditions and in the presence of both polymers;

- even though the spectrum of the PEDOT:PSS-containing sample is very similar the one of the C_3N_4 powder, its absorption edge is slightly shifted at higher wavelength, as a sign of the fact that the catalyst interacts with the polymer;
- the spectra of these two samples differ from the spectra of the one obtained through vapor-phase deposition (Figure 3.24), as they do not present the modulation of the background;

Concerning the morphology of the samples, as can be seen from the SEM images in Figures 3.28-3.31, the drop casting deposition does not allow the formation of a continuous layer of the material; as a matter of fact, the samples are made of a continuous layer of polymeric binder that contains a dispersion of the catalyst.

By comparison of the images of the different samples, it can be appreciated how the decrease of the dimension of the grains greatly benefits the homogeneity of the dispersion.

Photo-Electrochemical Characterization

For the samples with PEDOT:PSS as binder, it was noticed that the current flow causes the performances of the samples to rapidly change, with the current values that evidently lowered with each cycle, to the point that at first it seemed as if the electrodes worked better when the measure was conducted without illumination, rather than when they were exposed to light (in fact the measures without illumination were the very first to be performed).

For this reason, the OCV readings and CV measures were performed twice (alternating the ones in darkness and under illumination) on each sample in order to check the evolution of the performances, and the data reported are the ones of the second measures, in which the samples had stabilized, and the beneficial effect of illumination can be recognized.

The CRA measures were always performed on new samples.

From the OCV curves the effect of illumination can be observed, as the measures conducted in this condition gave potentials considerably more positive than the ones conducted in the dark, as depicted by the curves and the data reported in Figure 3.32 and Table 3.8.

Other effects that could be observed from the data are:

- the samples prepared with exfoliated-C_3N_4 developed a higher voltage, compared with the analogous prepared with bulk-C_3N_4;
- the samples prepared with Ca included-C_3N_4 developed a higher voltage, compared with the analogous prepared with exfoliated-C_3N_4.

When looking at the CV curves, represented in Figures 3.33-3.34, and, in particular, at the peak of current at $1.5\,V$, that is the voltage at which the hydrogen evolution reaction occurs, a few characteristics were highlighted:

- the beneficial effect of illumination is also seen when comparing the electric current evolved when the measure was conducted in the dark and under irradiation;
- For the electrodes prepared with Nafion as binder and for the ones with Ca included-C_3N_4 the sample prepared with the least amount of material developed a lower electric current, while for the electrodes with exfoliated-C_3N_4 and PEDOT:PSS as binder the two values are very similar;
- in the same experimental conditions, comparing samples prepared with the same amount of material, the electrodes containing Ca included-C_3N_4 developed a higher electric current then the ones with exfoliated-C_3N_4.

By visual inspection, after the CV measures, some of the Nafion films tended to detach from the substrate, and were deemed unsuitable for this application, while no evident degradation of the PEDOT:PSS-films was noted.

For the cathodes, it was chosen to perform the CRA measure on a wider variety of samples, as they are the materials in which the development was most focused and a change in their behaviour during a longer measure could not be ruled out; therefore, all the samples with PEDOT:PSS as polymeric binder were selected.

From the curves of the evolved electric current, it can be seen that all the samples reach a fairly similar value of current, and the HERs were calculated with a relation similar to the one already employed for the calculation of the OERs:

$$n\left(H_2\right) = \frac{\int\limits_{t_1}^{t_2} i\left(t\right)\,dt}{2Q_eN_A} \tag{3.2}$$

where, compared with Equation 3.1, the coefficient at the denominator is changed from 4 to 2 due to the different stoichiometry of the reactions.

The calculation was performed on the curves beyond 1000 s and the HER values are summarised in Table 3.9:

- for both types of samples, the one prepared with the least amount of active material was the one that provided a higher HER;
- comparing the samples prepared with equal amounts of material, the samples containing the exfoliated-C_3N_4 provided a slightly higher HER, compared with the ones containing the Ca included-C_3N_4.

Morphological Characterization of the Tested Samples

On a closer inspection of the CV-tested samples, from the SEM images in Figures 3.28e-3.28f the degradation of the Nafion films becomes evident as the flow of electric current caused the polymer to furrow and separate from the substrate.

On the other hand, the PEDOT:PSS-samples showed different degrees of degradation: while the samples containing exfoliated-C_3N_4 (Figures 3.30e-3.30f) did not appeared to be very affected by the CRA measure, the ones containing Ca included-C_3N_4 (Figures 3.31e-3.31f) showed an extensive degradation, with the formation of cracks and holes in the slurry.

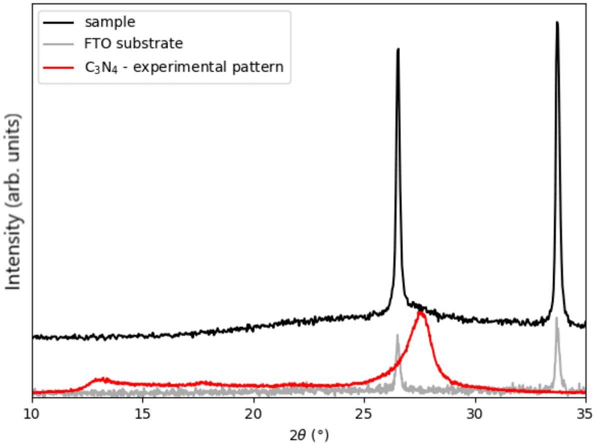

Figure 3.23. Comparison between the experimental XRD patterns of the VPD-sample, of the crystalline substrate and the powder of C_3N_4.

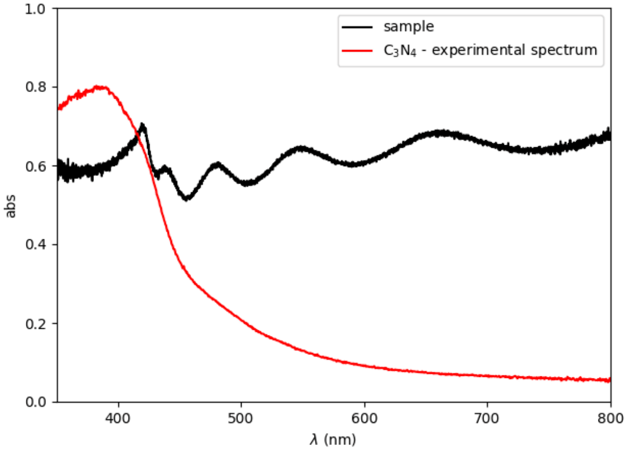

Figure 3.24. Comparison between the UV-Vis absorption spectra of the VPD-sample and of the powder of C_3N_4.

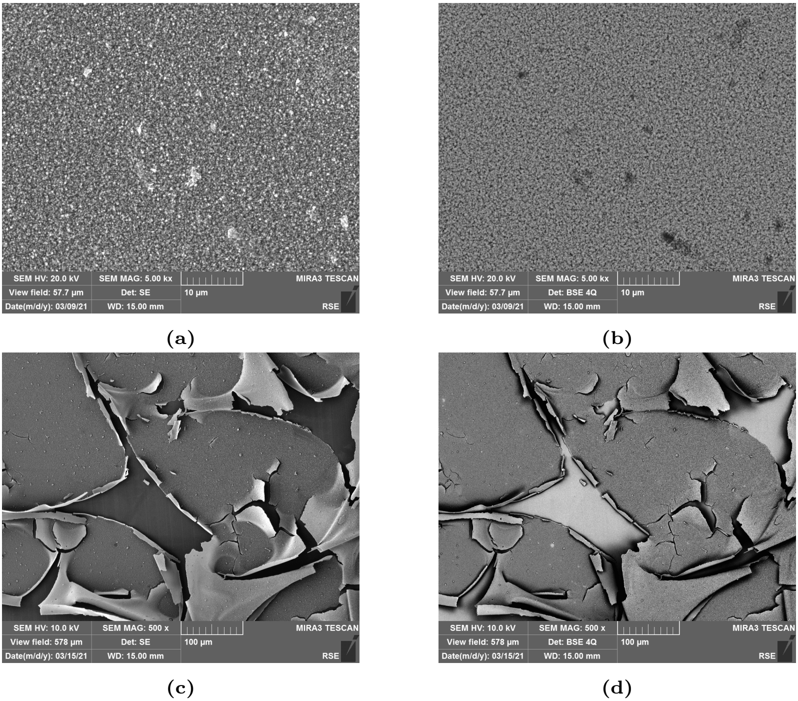

Figure 3.25. a) Secondary Electrons- and b) Back Scattered Electrons- SEM images of the pristine VPD-sample. c) Secondary Electrons- and d) Back Scattered Electrons- SEM images of the VPD-sample subjected to CV.

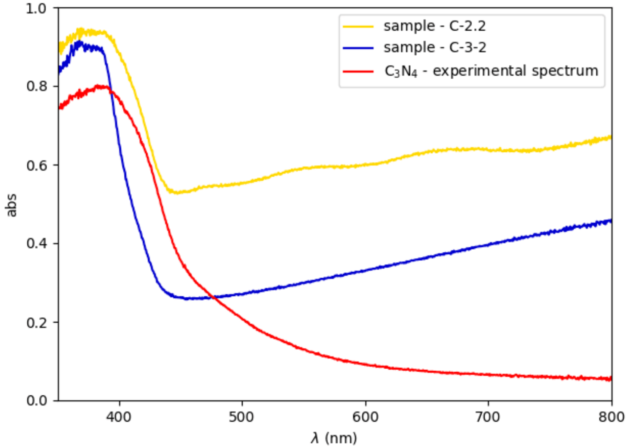

Figure 3.26. Comparison between the UV-Vis absorption spectra of the C-2.2 and C-3.2 samples and of the C_3N_4 powder.

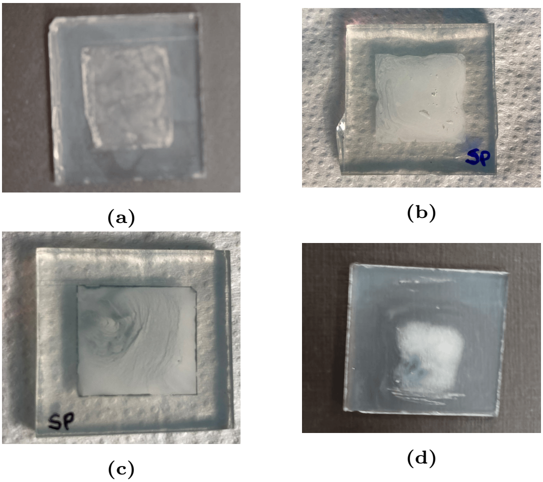

(a)

(b)

(c)

(d)

Figure 3.27. Photographs of the pristine samples a) C-1.2, b) C-2.2, c) C-3.2 and d) C-4.2.

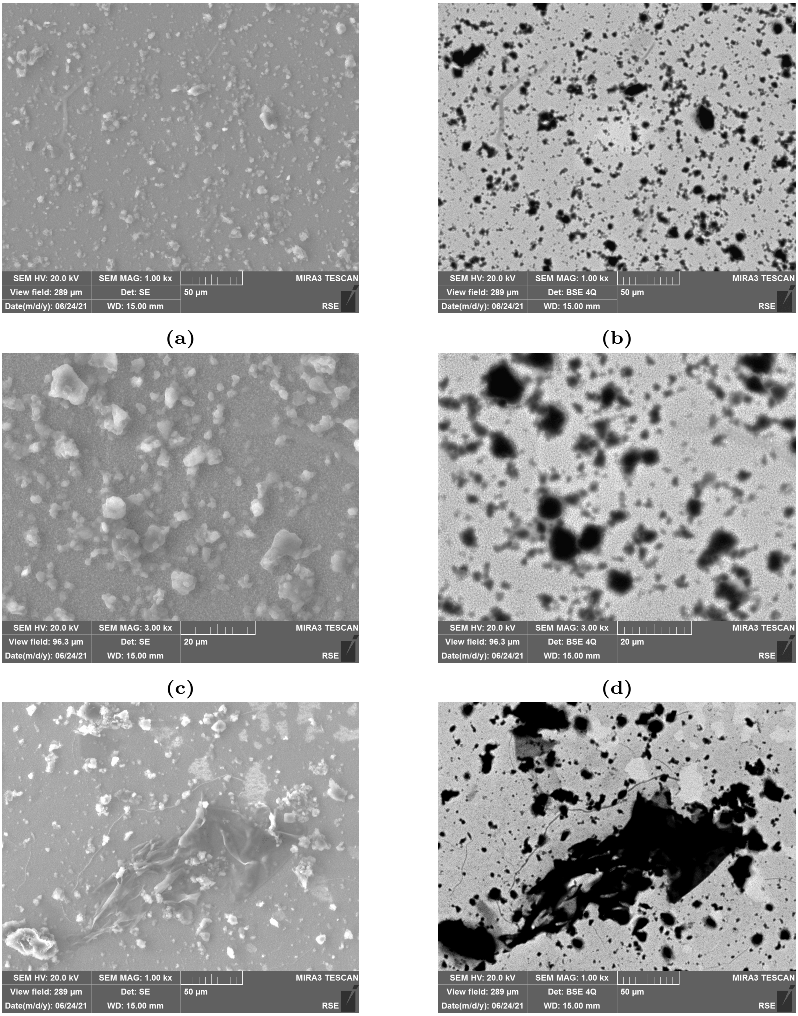

(a) **(b)**

(c) **(d)**

(e) **(f)**

Figure 3.28. a,c) Secondary Electrons- and b,d) Back Scattered Electrons- SEM images of the pristine C-1.2 sample. e) Secondary Electrons- and f) Back Scattered Electrons- SEM images of the C-1.2 sample subjected to CV measure.

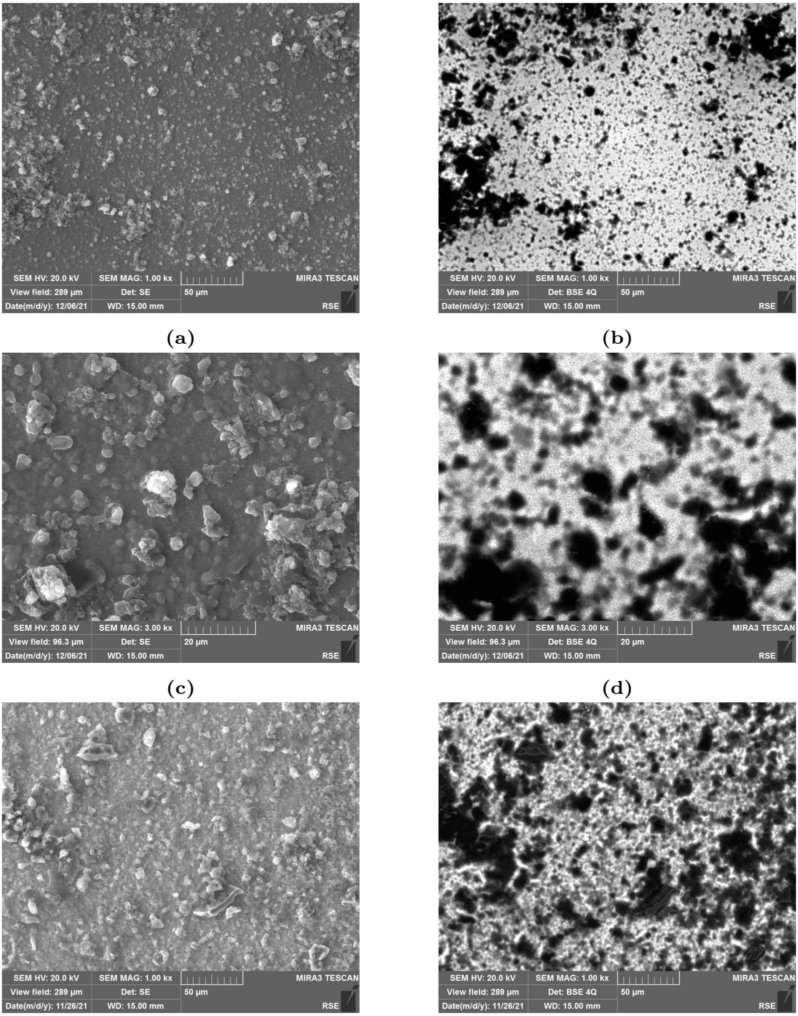

(a) **(b)**

(c) **(d)**

(e) **(f)**

Figure 3.29. a,c) Secondary Electrons- and b,d) Back Scattered Electrons- SEM images of the pristine C-2.2 sample. e) Secondary Electrons- and f) Back Scattered Electrons- SEM images of the C-2.2 sample subjected to CV measure.

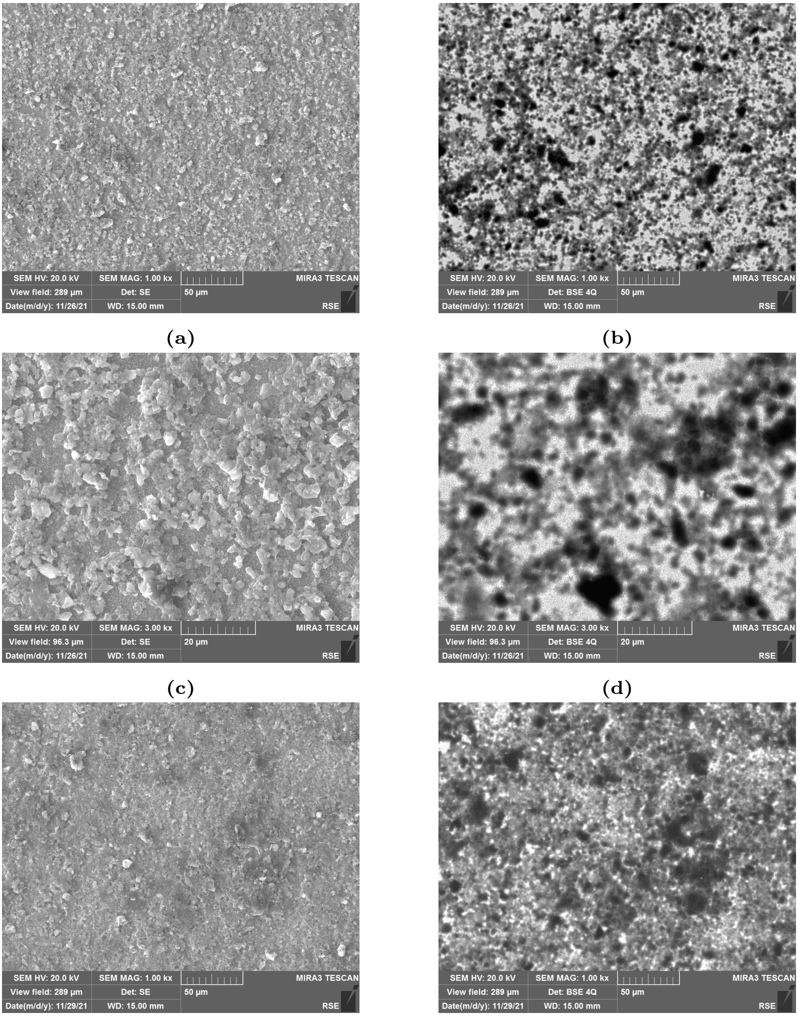

(a) **(b)**

(c) **(d)**

(e) **(f)**

Figure 3.30. a,c) Secondary Electrons- and b,d) Back Scattered Electrons- SEM images of the pristine C-3.2 sample. e) Secondary Electrons- and f) Back Scattered Electrons- SEM images of the C-3.2 sample subjected to CRA measure.

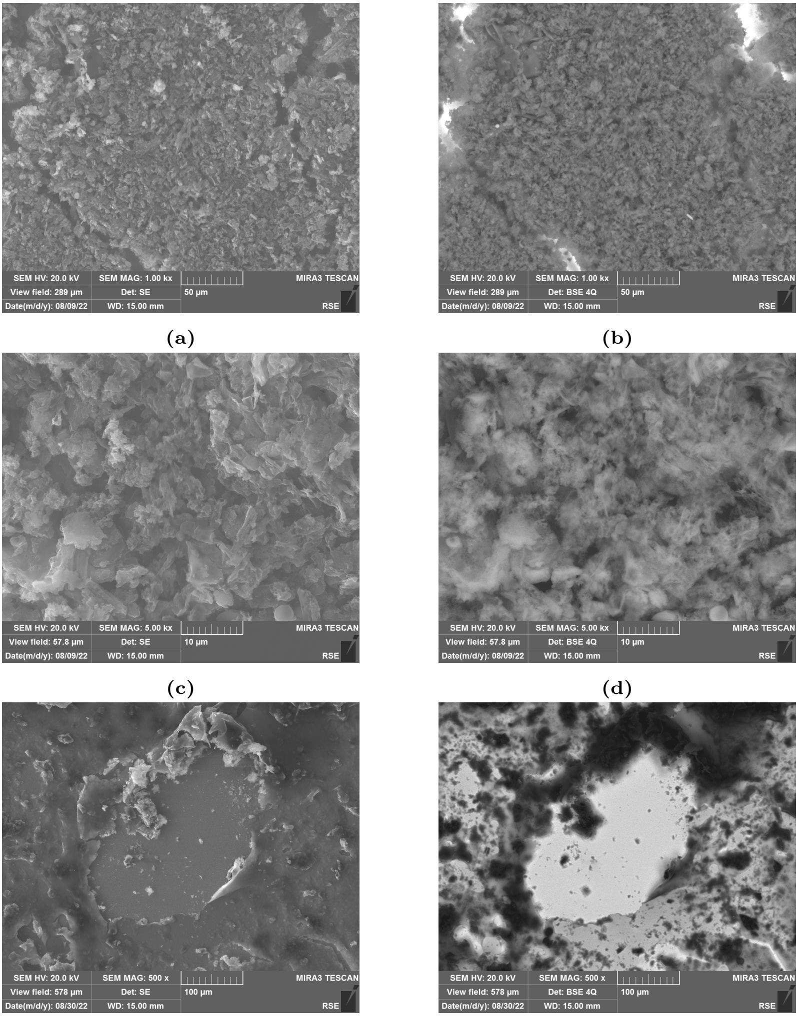

(a) **(b)**

(c) **(d)**

(e) **(f)**

Figure 3.31. a,c) Secondary Electrons- and b,d) Back Scattered Electrons- SEM images of the pristine C-4.2 sample. e) Secondary Electrons- and f) Back Scattered Electrons- SEM images of the C-4.2 sample subjected to CRA measure.

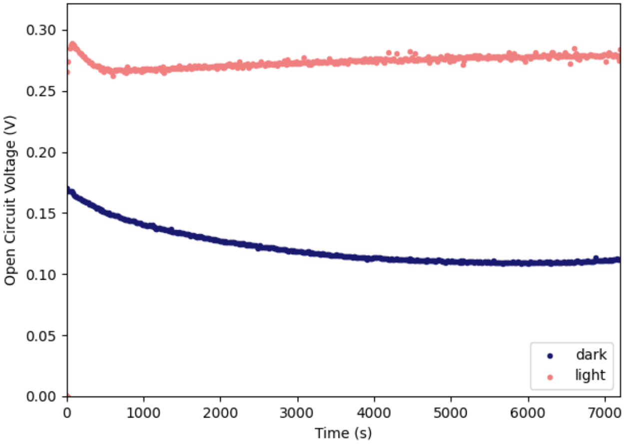

Figure 3.32. OCV readings of the C-3.1 sample.

Table 3.8. OCV values reached by each sample in the two conditions after 2 h of reading.

Label	OCV - in dark (mV)	OCV - in light (mV)
C-1.1 *	28.2	109
C-1.2 *	48.9	122
C-2.1 *	48.8	201
C-2.2 *	170	227
C-3.1	112	279
C-3.2	83	226
C-4.1	164	298
C-4.2	152	215

* illumination with halogen lamp

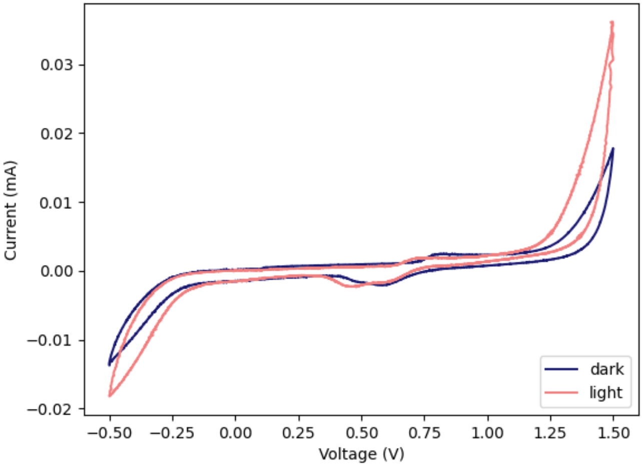

(a)

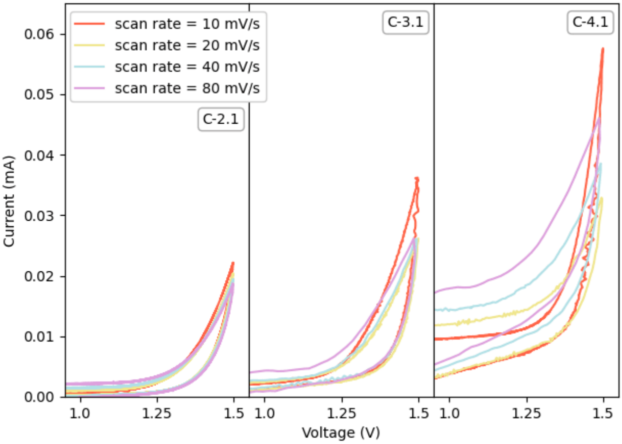

(b)

Figure 3.33. CV of the samples, comparison between the measures performed a) in the dark and under illumination, at $10\,mV\,s^{-1}$ (C-3.1), b) at different scan rates, under illumination (C-2.1, C-3.1, C-4.1).

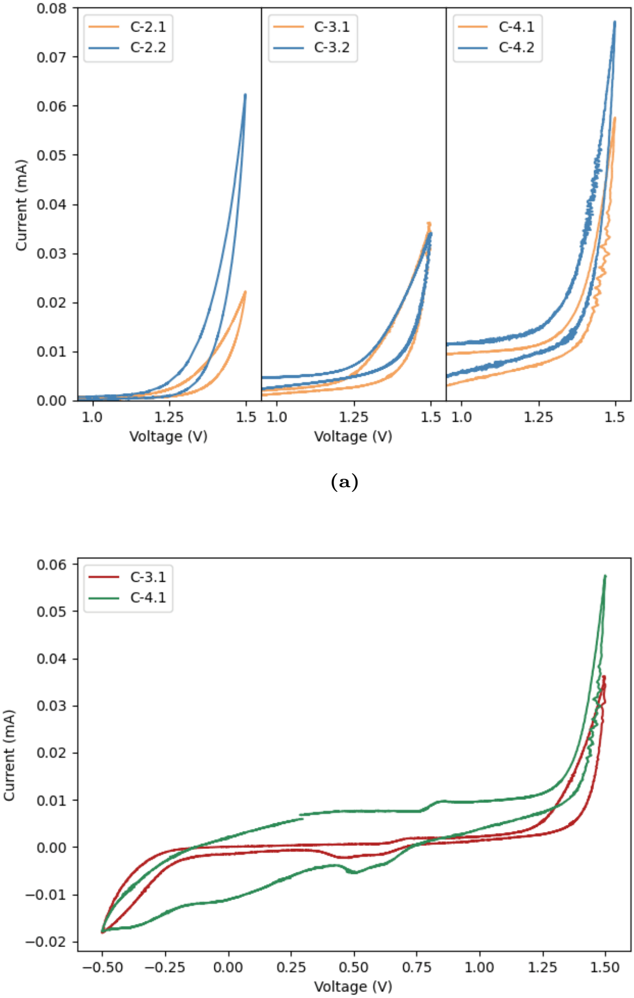

(a)

(b)

Figure 3.34. CV of the samples, comparison between the measures of the a) C-2.1 - C-2.2 , C-3.1 - C-3.2 and C-4.1 - C-4.2 samples, performed at $10\,mV\,s^{-1}$ under illumination, b) C-3.1 - C-4.1 samples, performed at $10\,mV\,s^{-1}$ under illumination.

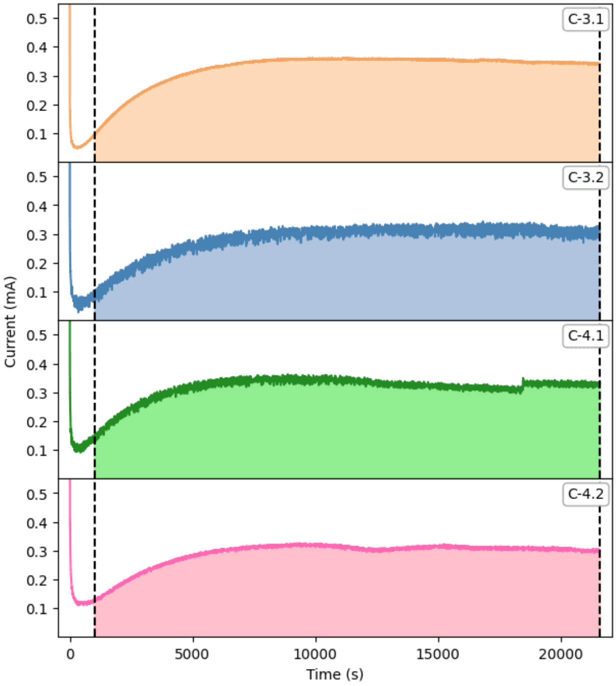

Figure 3.35. CRA measure of the C-3.1, C-3.2, C-4.1 and C-4.2 samples, the areas considered for HER calculation are highlighted.

Table 3.9. HER values of the characterized samples.

Label	**Hydrogen Evolution Rate** $(mol\,h^{-1}\,cm^{-2})$
C-3.1	$6.09 \cdot 10^{-6}$
C-3.2	$5.26 \cdot 10^{-6}$
C-4.1	$5.88 \cdot 10^{-6}$
C-4.2	$3.10 \cdot 10^{-6}$

g-C_3N_4 / $Cs_3Bi_2Br_9$ system

At the same time that C_3N_4 electrodes were developed, experimentation on C_3N_4/co-catalyst electrodes was started.

$Cs_3Bi_2Br_9$ was first selected, among the materials previously characterized, for the depositions of the electrodes due to the higher thermal stability of all-inorganic perovskites, compared with hybrid perovskites and their derivatives, that would have been required for the vapor phase deposition of C_3N_4.

Some of those samples have actually been prepared, by sputtering deposition of $Cs_3Bi_2Br_9$ followed by vapor phase deposition of C_3N_4; however, since this kind of C_3N_4 proved to be unsuitable for the application, they will not be discussed further.

Since experimentation was carried out in parallel with the one on C_3N_4 electrodes, the same kind of samples were prepared, and are listed in Table 3.10.

The characterization of the samples was performed with the same techniques previously used.

Table 3.10. List of the characterized samples.

Label	Sample	Binder	Description
C-5.1	bulk-C_3N_4/ $Cs_3Bi_2Br_9$ 2.5% *wt*	Nafion	diluted sample
C-5.2	bulk-C_3N_4/ $Cs_3Bi_2Br_9$ 2.5% *wt*	Nafion	concentrated sample
C-6.1	exfoliated-C_3N_4/ $Cs_3Bi_2Br_9$ 2.5% *wt*	Nafion	diluted sample
C-6.2	exfoliated-C_3N_4/ $Cs_3Bi_2Br_9$ 2.5% *wt*	Nafion	concentrated sample
C-7.1	exfoliated-C_3N_4/ $Cs_3Bi_2Br_9$ 2.5% *wt*	PEDOT:PSS	diluted sample
C-7.2	exfoliated-C_3N_4/ $Cs_3Bi_2Br_9$ 2.5% *wt*	PEDOT:PSS	concentrated sample
C-8.1	Ca included-C_3N_4/ $Cs_3Bi_2Br_9$ 2.5% *wt*	PEDOT:PSS	diluted sample
C-8.2	Ca included-C_3N_4/ $Cs_3Bi_2Br_9$ 2.5% *wt*	PEDOT:PSS	concentrated sample

Morphological and Optical Characteristics

The UV-Vis absorption spectra of the electrodes (Figure 3.36), as was observed for the C_3N_4 electrodes, fairly resembles that of the powdered sample, and it was concluded that the deposition process did not compromise the nature of the sample.

The morphology of the samples is also basically the same as that of the C_3N_4 electrodes, with a dispersion of the powder embedded inside the polymer matrix. The homogeneity of the dispersions is also comparable with the ones of the C_3N_4 electrodes, with the high-surface-area-C_3N_4 samples more homogeneous than the bulk- ones, as can be seen in Figures 3.38-3.41.

In addition, only for the samples with exfoliated-C_3N_4 and PEDOT:PSS as polymeric matrix, the grains of the perovskites could be directly seen with the aid of high magnification SEM images, represented in Figures 3.40c-3.40d.

Photo-Electrochemical Characterization

For the same reasons that were described in the previous paragraph, once again, the OCV readings and CV measures were performed twice on the samples with PEDOT:PSS binder, and the data reported are those of the second measures.

The CRA were always performed on new samples.

The OCV data, represented in Figure 3.42 and Table 3.11 showed the same relations evidenced for the C_3N_4:

- the samples prepared with exfoliated-C_3N_4 developed a higher voltage, compared with the analogous prepared with bulk-C_3N_4;
- the samples prepared with Ca included-C_3N_4 developed a higher voltage, compared with the analogous prepared with exfoliated-C_3N_4.

When looking at the CV curves, represented in Figures 3.43-3.44, and, in particular, at the peak of current at $1.5\,V$, a few characteristics were highlighted:

- the beneficial effect of illumination is seen when comparing the electric current evolved when the measure was conducted in the dark and under irradiation;

- the electric current seems to be slightly dependent on the scan rate, as the peaks of current decrease when the scan rate increases;
- in the same experimental conditions, the samples prepared with the higher and lower amount of material developed different electric currents, however the different kinds of samples showed different behaviour;
- in the same experimental conditions, comparing samples prepared with the same amount of material, the electrodes containing Ca included-C_3N_4 developed a lower electric current then the ones with exfoliated-C_3N_4, contrary to what was observed for the C_3N_4 electrodes.

However, the most relevant data is that the $C_3N_4/Cs_3Bi_2Br_9$ samples developed an electric current generally higher than the C_3N_4 electrodes, especially in the case of the samples containing exfoliated-C_3N_4 and PEDOT:PSS as binder.

By visual inspection, the samples presented the same problematic of the C_3N_4 electrodes; with some of the Nafion-films that tended to detach from the substrate after the CV measure, and no evident degradation of the PEDOT:PSS-films noted.

Since the behaviour of these electrodes was quite similar to the one of the C_3N_4 electrodes, the same kinds of samples were selected to undergo the CRA measure, that was performed on all the samples with PEDOT:PSS polymeric binder.

From the curves of the evolved electric current (Figure 3.45) it can be seen that there was a marked difference between the performances of the four samples, that is reflected on the HERs, that were calculated with Equation 3.2 on the curves beyond $1000\,s$ and are summarized in Table 3.12:

- as was observed for the C_3N_4 electrodes, for both types of samples, the one prepared with the least amount of active material provided a slightly higher HER;
- comparing the samples prepared with equal amounts of material, the samples containing the exfoliated-C_3N_4 granted a markedly higher HER, compared with the ones containing the Ca included-C_3N_4.

In addition to these observations, it is meaningful to note that all these samples achieved a HER substantially higher than the analogous C_3N_4 electrodes without co-catalyst, in accordance with the preliminary data obtained from the powders of the catalysts (Chapter2.2) and the data of the CV.

Morphological Characterization of the Tested Samples

On a closer inspection, it was observed that the photo-electrochemically tested samples behaved similarly to the C_3N_4 electrodes; from the SEM images in Figures 3.38-3.41 the degradation of the Nafion films is evident, while the samples with PEDOT:PSS binder did not suffer from this kind of degradation.

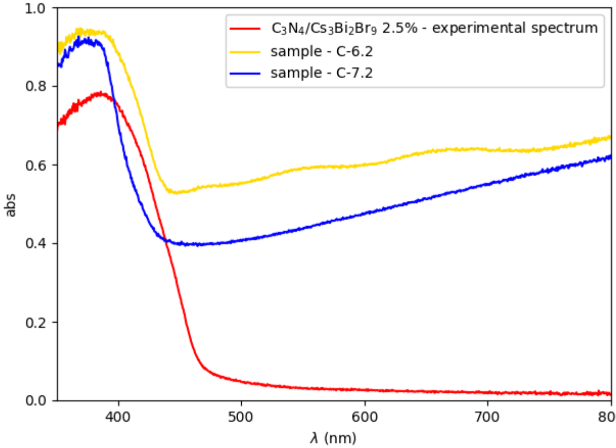

Figure 3.36. Comparison between the UV-Vis absorption spectra of the C-6.2 and C-7.2 samples and of the $C_3N_4/Cs_3Bi_2Br_9$ 2.5% powder.

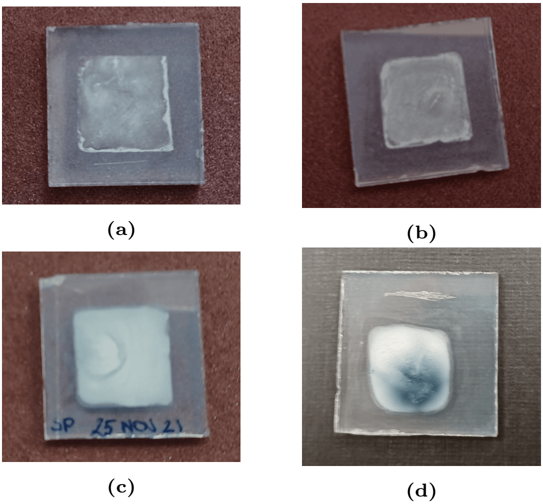

Figure 3.37. Photographs of the pristine samples a) C-5.2, b) C-6.2, c) C-7.2 and d) C-8.2.

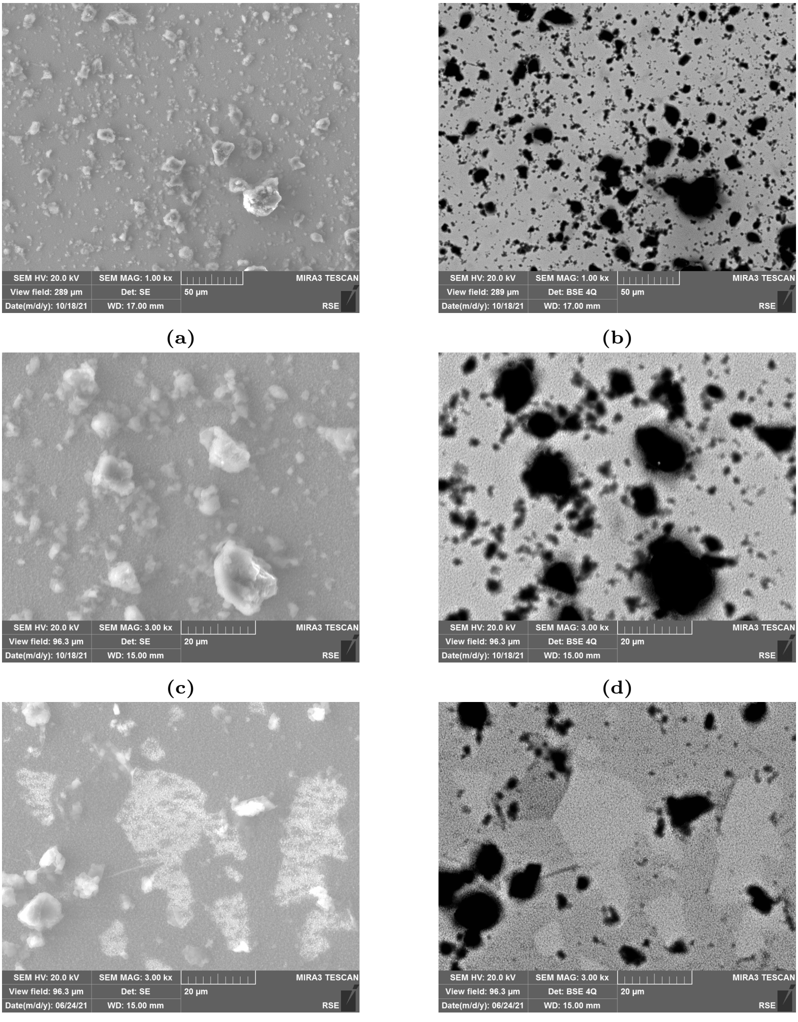

(a) **(b)**

(c) **(d)**

(e) **(f)**

Figure 3.38. a,c) Secondary Electrons- and b,d) Back Scattered Electrons- SEM images of the pristine C-5.2 sample. e) Secondary Electrons- and f) Back Scattered Electrons- SEM images of the C-5.2 sample subjected to CV measure.

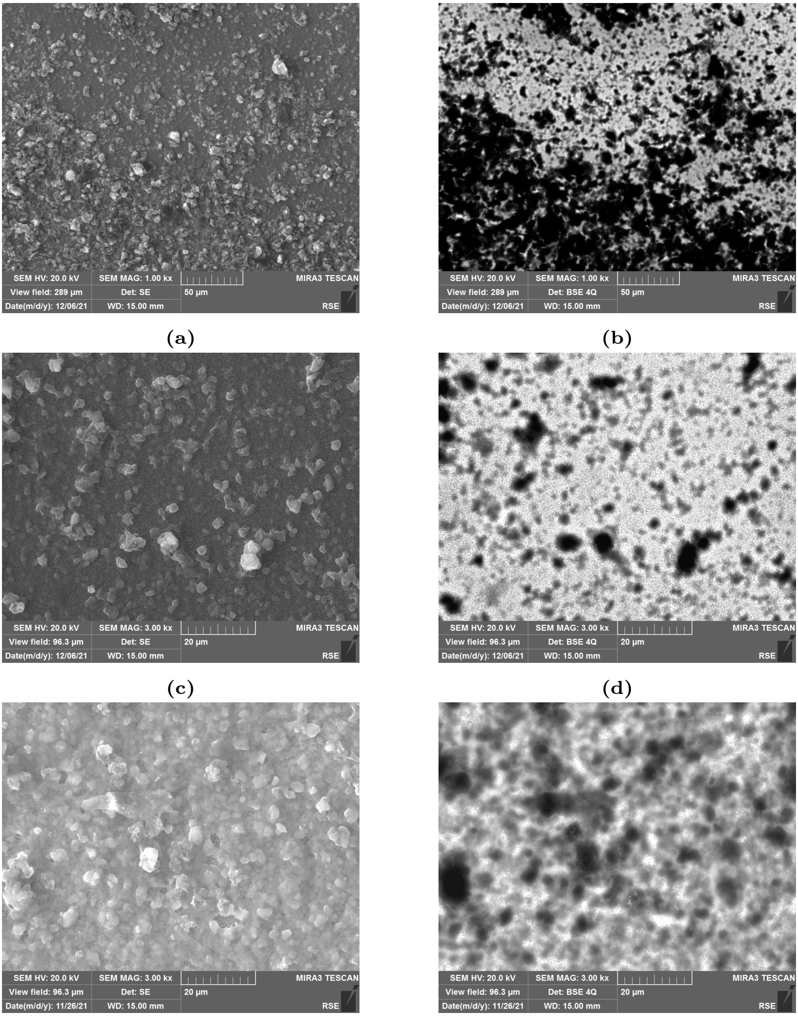

(a) **(b)**

(c) **(d)**

(e) **(f)**

Figure 3.39. a,c) Secondary Electrons- and b,d) Back Scattered Electrons- SEM images of the pristine C-6.2 sample. e) Secondary Electrons- and f) Back Scattered Electrons- SEM images of the C-6.2 sample subjected to CV measure.

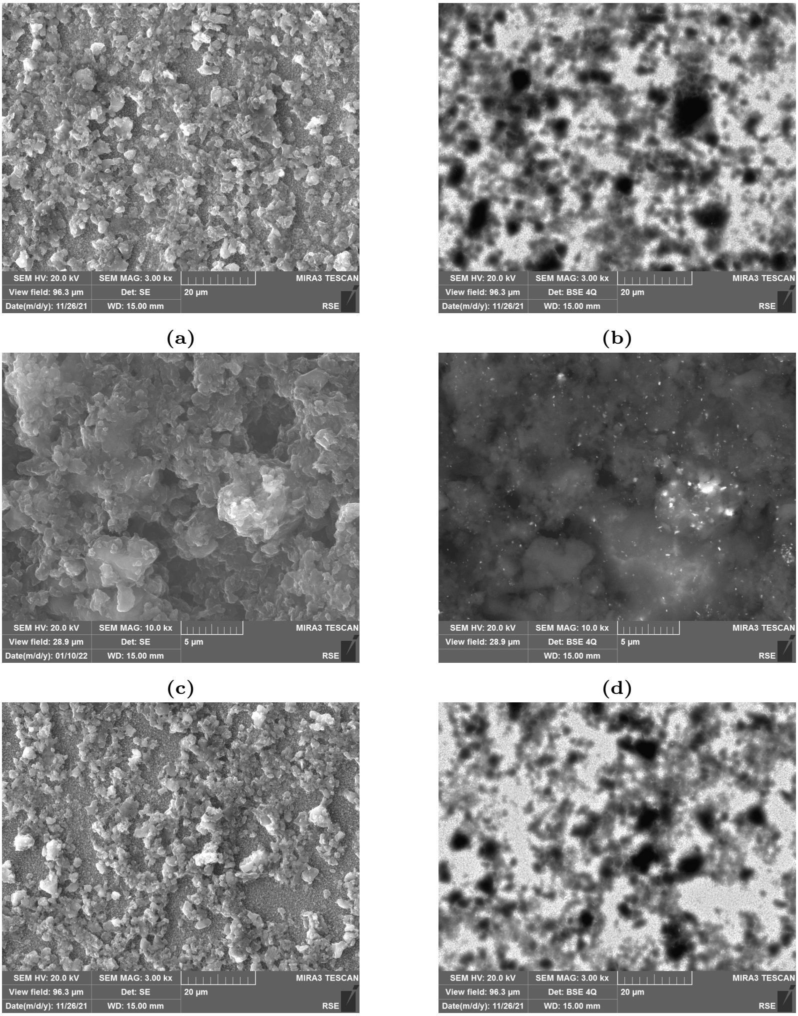

(a) **(b)**

(c) **(d)**

(e) **(f)**

Figure 3.40. a,c) Secondary Electrons- and b,d) Back Scattered Electrons- SEM images of the pristine C-7.2 sample. e) Secondary Electrons- and f) Back Scattered Electrons- SEM images of the C-7.2 sample subjected to CRA measure.

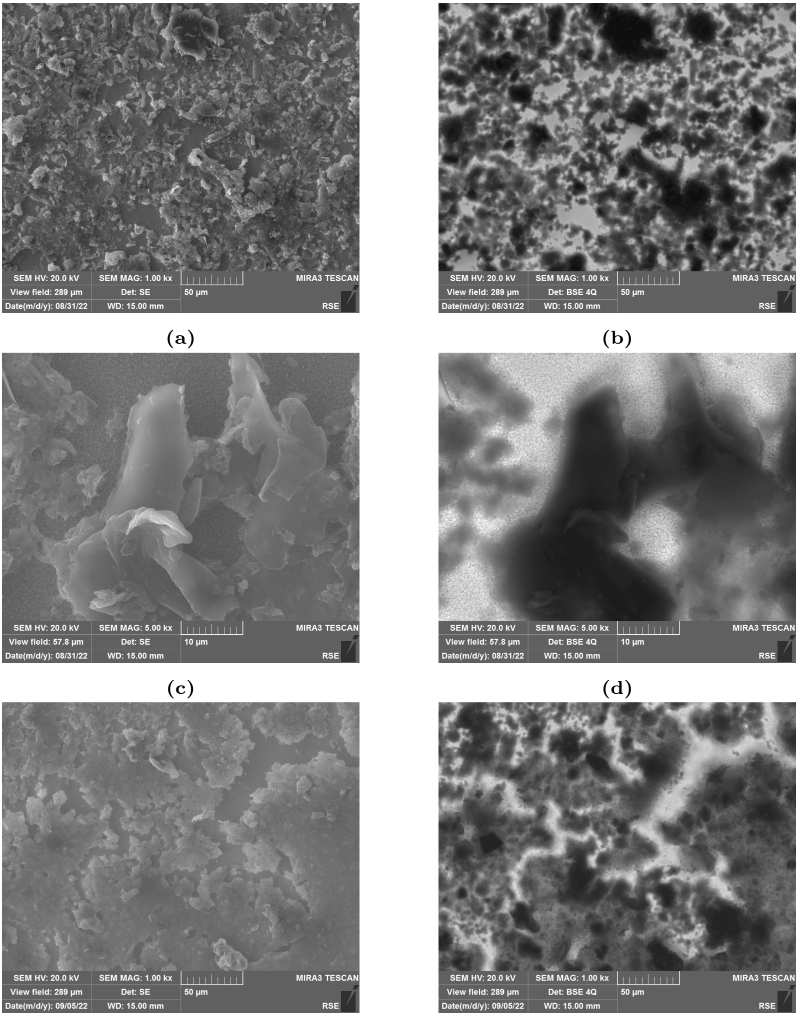

(a) **(b)**

(c) **(d)**

(e) **(f)**

Figure 3.41. a,c) Secondary Electrons- and b,d) Back Scattered Electrons- SEM images of the pristine C-8.2 sample. e) Secondary Electrons- and f) Back Scattered Electrons- SEM images of the C-8.2 sample subjected to CRA measure.

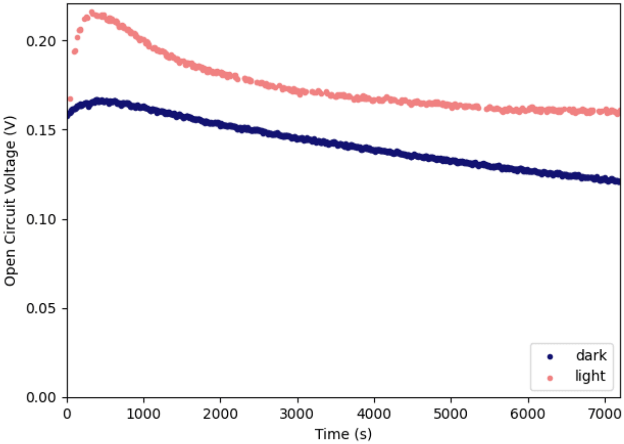

Figure 3.42. OCV reading of the C-7.1 sample.

Table 3.11. OCV values reached by each sample in the two conditions after 2 h of reading.

Label	**OCV - in dark (mV)**	**OCV - in light (mV)**
C-5.1 *	92.0	138
C-5.2 *	119	188
C-6.1 *	83	218
C-6.2 *	151	284
C-7.1	121	160
C-7.2	72	180
C-8.1	110	180
C-8.2	139	241

* illumination with halogen lamp

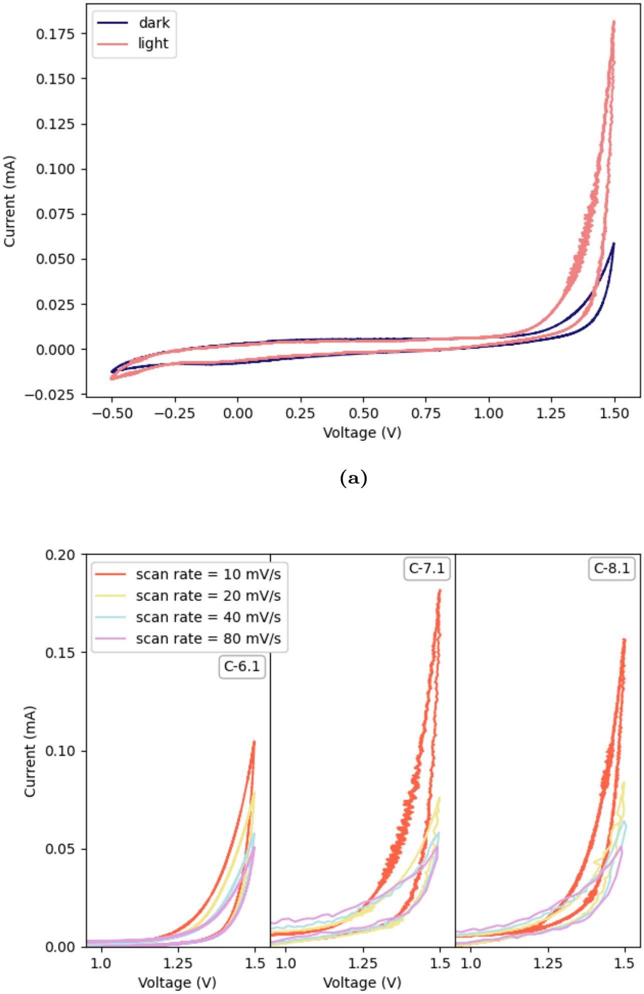

(a)

(b)

Figure 3.43. CV of the samples, comparison between the measures performed a) in the dark and under illumination, at $10\, mV\, s^{-1}$ (C-7.1), b) at different scan rates, under illumination (C-6.1, C-7.1, C-8.1).

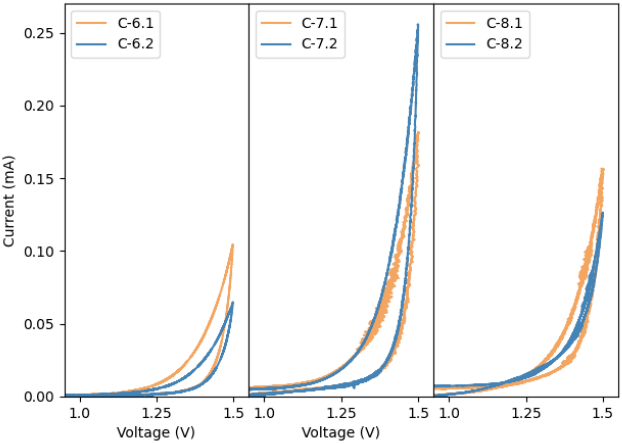

(a)

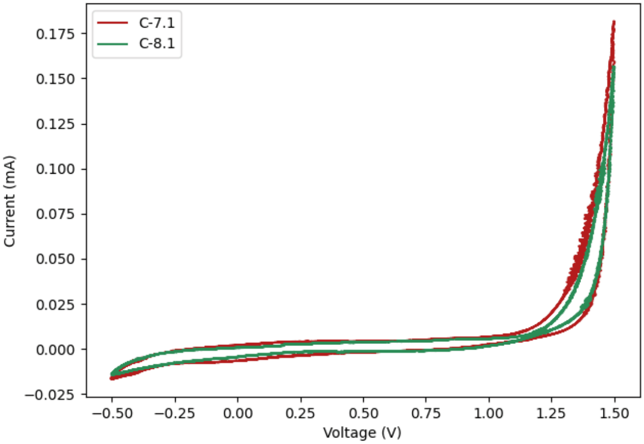

(b)

Figure 3.44. CV of the samples, comparison between the measures of the a) C-6.1 - C-6.2 , C-7.1 - C-7.2 and C-8.1 - C-8.2 samples, performed at $10\,mV\,s^{-1}$ under illumination, b) C-7.1 - C-8.1 samples, performed at $10\,mV\,s^{-1}$ under illumination.

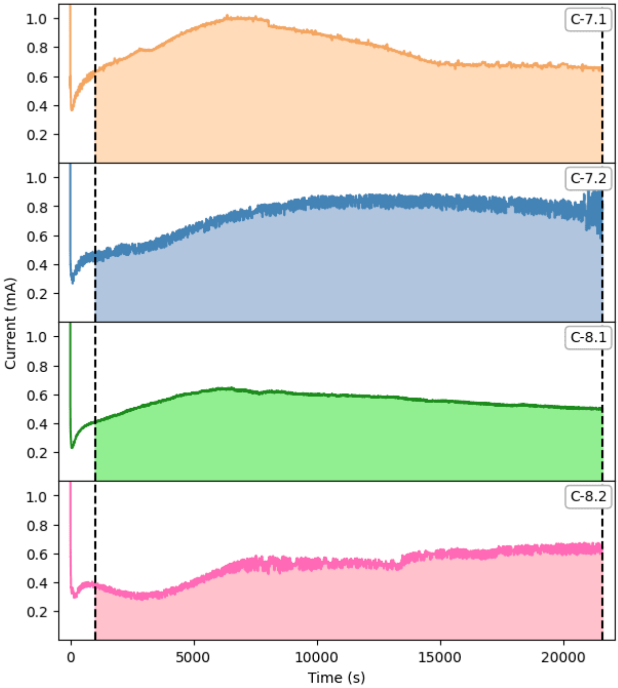

Figure 3.45. CRA measure of the C-7.1, C-7-2, C-8.1 and C-8.2 samples, the areas considered for HER calculation are highlighted.

Table 3.12. HER values of the characterized samples.

Label	**Hydrogen Evolution Rate** $(mol\,h^{-1}\,cm^{-2})$
C-7.1	$14.8 \cdot 10^{-6}$
C-7.2	$13.9 \cdot 10^{-6}$
C-8.1	$10.4 \cdot 10^{-6}$
C-8.2	$9.66 \cdot 10^{-6}$

g-C_3N_4 / PEA_2SnBr_4 system

After the experimentation on C_3N_4/$Cs_3Bi_2Br_9$, focus was also placed on the C_3N_4/PEA_2SnBr_4 system, that had been found to be the best performing one from the preliminary tests on powders (see Paragraph 2.2).

Due to the experience already gained with the previous samples, only PEDOT:PSS was employed as binder and bulk-C_3N_4 was discarded in the preparation of the samples; however, due to the poor performances of the system, that will be described in this Paragraph, the experimentation on PEA_2SnBr_4 was halted prematurely and no sample with Ca included-C_3N_4 was prepared (since this kind of C_3N_4 was only synthesised in the later stages of the experimentation).

The samples are listed in Table 3.13.

Morphological and Optical Characteristics

The UV-Vis absorption spectra of the electrodes (Figure 3.46), as was observed for the previous samples, fairly resembles that of the powdered sample, as such it was concluded that the deposition process did not compromise the nature of the sample.

Concerning the morphology of the samples (Figure 3.48), once again it is dominated by the characteristics of C_3N_4; in this case it was not possible to capture the grains of the co-catalyst, not even at high magnification with Back-Scattered-Electrons photographs, most likely due to a homogeneous dispersion of very small grains, however the presence of the phase is confirmed by the EDS analysis that revealed the presence of tin and bromine.

Table 3.13. List of the characterized samples.

Label	Sample	Binder	Description
C-9.1	exfoliated-C_3N_4/ PEA_2SnBr_4 5% *wt*	PEDOT:PSS	diluted sample
C-9.2	exfoliated-C_3N_4/ PEA_2SnBr_4 5% *wt*	PEDOT:PSS	concentrated sample

Photo-Electrochemical Characterization

The OCV data, represented in Figure 3.50 and Table 3.15 showed that all the samples develop a considerably higher voltage under illumination, with the OCV of the sample prepared with the least amount of material being higher that the other one.

When looking at the CV curves, represented in Figures 3.51-3.52, and, in particular, at the peak of current at $1.5\,V$, a few characteristics were highlighted:

- the effect of illumination on the evolved current can be observed;
- in the same experimental conditions, the sample prepared with the higher amount of material developed a higher electric current than the one with a lower amount of material.

In this case also, as was observed for the $C_3N_4/Cs_3Bi_2Br_9$ electrodes, the C_3N_4/PEA_2SnBr_4 samples developed an electric current generally higher than the C_3N_4 electrodes, however the increase in current was much smaller compared with that of the $C_3N_4/Cs_3Bi_2Br_9$ electrodes.

The CRA measure was performed on both samples, and the curves are represented in Figure 3.53.

The HERs were calculated with Equation 3.2 on the curves beyond $1000\,s$ and the values are summarized in Table 3.14:

- when the results are compared with the ones of the C_3N_4 and $C_3N_4/Cs_3Bi_2Br_9$ electrodes, contrary to the previous systems, the electrode prepared with the least amount of active material was the one to provide a lower HER;
- the other critical fact is that the sample prepared with the least amount of material gave a HER lower than the one of the corresponding C_3N_4 electrode.

Table 3.14. HER values of the characterized samples.

Label	**Hydrogen Evolution Rate** $(mol\,h^{-1}\,cm^{-2})$
C-9.1	$4.87 \cdot 10^{-6}$
C-9.2	$5.41 \cdot 10^{-6}$

These were the unexpectedly poor performances that caused the decision to cease the experimentation on PEA_2SnBr_4.

In addition to this, another unfortunate effect that emerged after the CRA measure is that the slurry of the active material was highly damaged during the catalysis process, as can be seen in the photograph in Figure 3.47b.

Morphological Characterization of the Tested Samples

Morphological characterisation was also performed on the photo-electrochemically-tested samples; from the SEM images in Figure 3.49 it can be seen how, in some places, large sections of the samples were removed from the substrate.

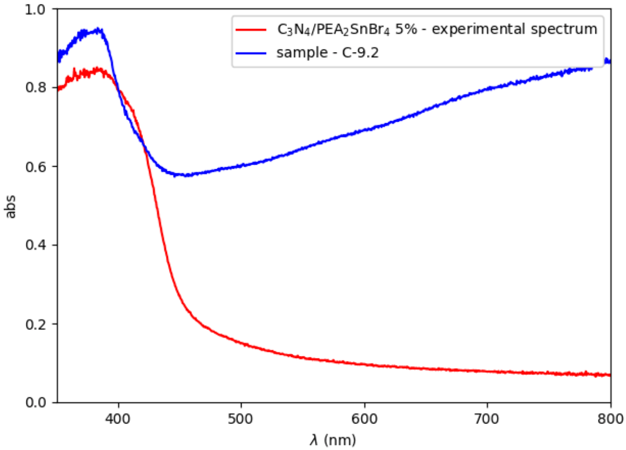

Figure 3.46. UV-Vis absorption spectra of the C_3N_4/PEA_2SnBr_4 5% powder and C-9.2 sample

(a)

(b)

Figure 3.47. Photographs of the C-9.2 sample a) pristine and b) after CRA.

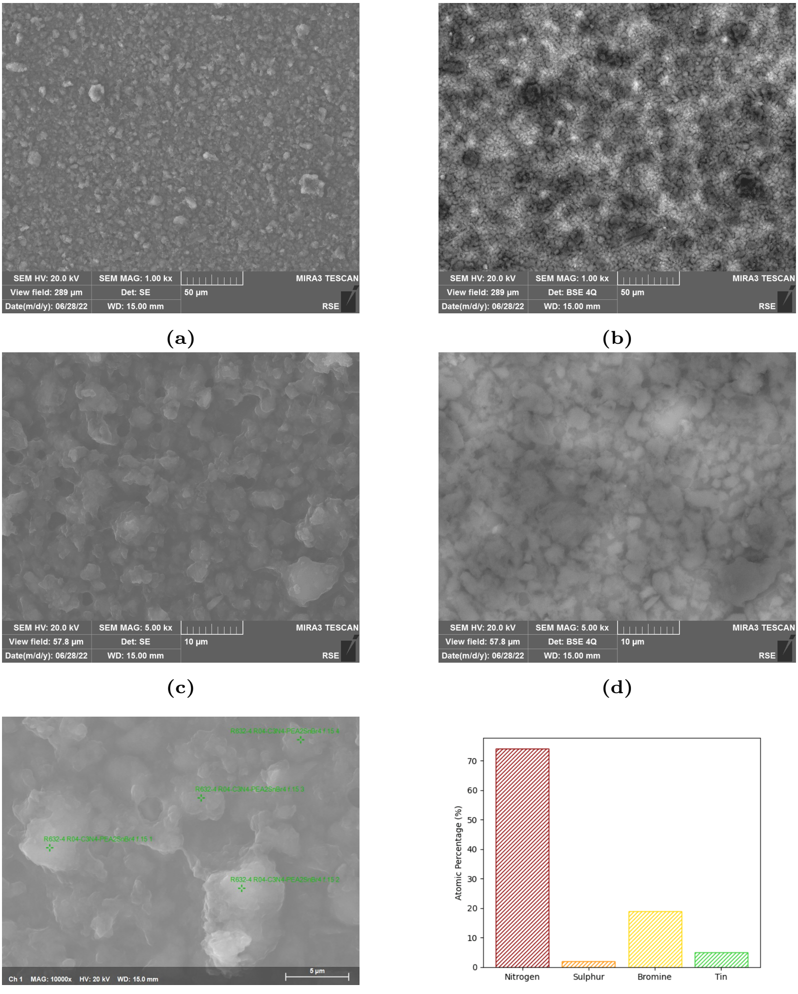

(a)

(b)

(c)

(d)

(e)

(f)

Figure 3.48. a,c) Secondary Electrons- and b,d) Back Scattered Electrons-SEM images of the C-9.2 pristine sample, at two different magnifications. e) Area subjected to EDS analysis and f) quantification in atomic percentages of the components of the electrode (since the sample was covered with graphite for the analysis, both C and the components of the substrate were omitted from the quantification).

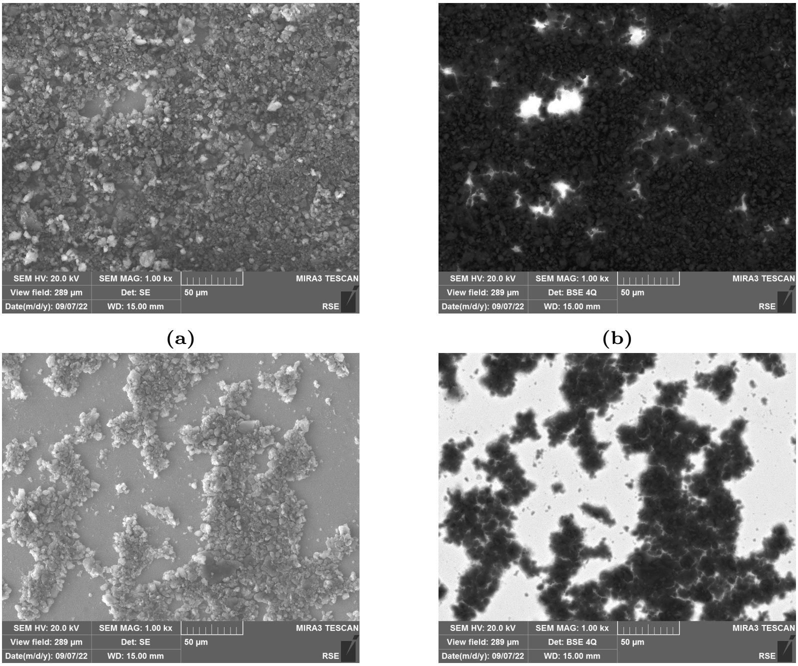

(a) **(b)**

(c) **(d)**

Figure 3.49. a,c) Secondary Electrons- and b,d) Back Scattered Electrons-SEM images of the C-9.2 sample subjected to CRA measure.

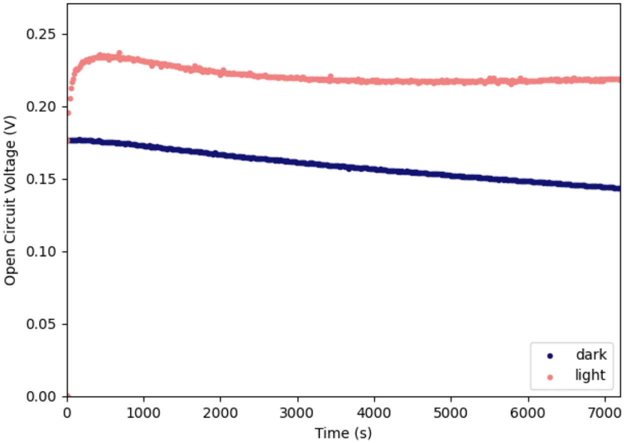

Figure 3.50. OCV reading of the C-9.1 sample.

Table 3.15. OCV values reached by each sample in the two conditions after 2 h of reading.

Label	**OCV - in dark (mV)**	**OCV - in light (mV)**
C-9.1	144	219
C-9.2	125	164

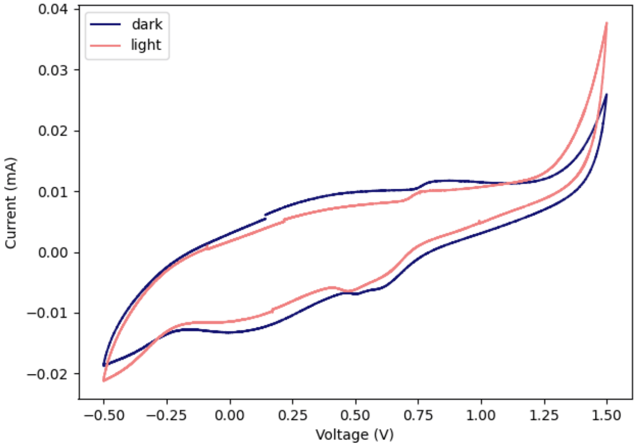

(a)

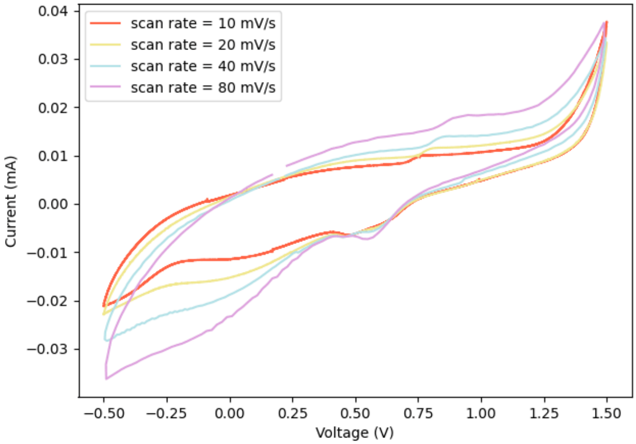

(b)

Figure 3.51. CV of the C-9.1 sample, comparison between the measures performed a) in the dark and under illumination, at $10\,mV\,s^{-1}$, b) at different scan rates, under illumination.

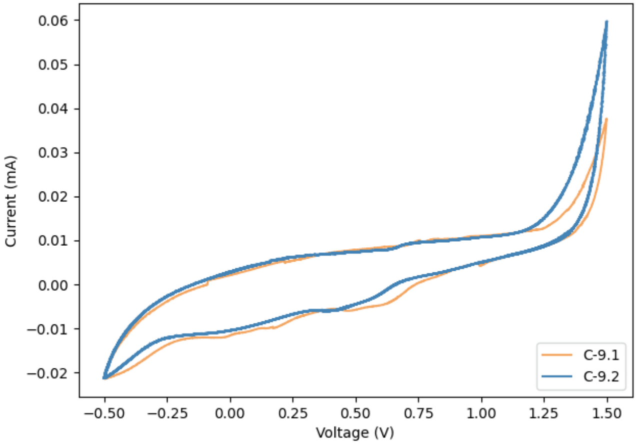

Figure 3.52. Comparison between the CV measures of the C-9.1 and C-9.2 samples, performed at $10\,mV\,s^{-1}$ under illumination.

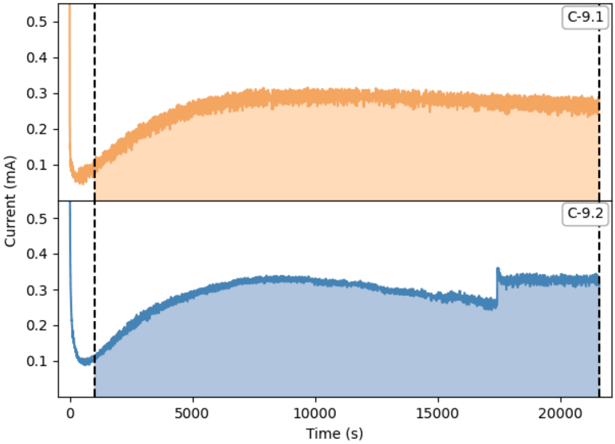

Figure 3.53. CRA measure of the C-9.1 and C-9.2 samples, the areas considered for HER calculation are highlighted.

Chapter 4

Complete Photo-electrochemical Cells

Finally, after the experimentation on the half-cells, that were needed in order to characterize the individual electrodes, one anode and one cathode (Table 4.1) were selected to build complete photo-electrochemical cells. The criteria for the selection were:

anode: since the voltage developed by the single electrode on its own was not enough to activate the photo-reaction, among the protected and more stable samples, it was chosen the sample that gave rise to the higher value of OCV.

It should be noted that the sample that generated the larger OCV is not the one that provided the highest OER, however, since the difference was not conspicuous, it was overlooked in favour of the difference in developed voltage;

cathode: since, among all the tested samples there were clear differences between the reached HER, this was used as first criterion; between the samples that reached the higher HERs, the final choice was again based on the value of OCV.

Table 4.1. List of the selected electrodes.

Label	Sample	Description
A-2.2	$BiVO_4/TiO_2$-P25/PEI	50% *mol* TiO_2, relative to $BiVO_4$
C-7.2	exfoliated-C_3N_4/ $Cs_3Bi_2Br_9$/PEDOT:PSS	concentrated sample

The photo-electrochemical characterization on the complete cells was much like the one performed on the half cells, however only the OCV readings and CRA measures were performed, and the CRAs were performed for $12\,h$ instead of $6\,h$.

For these measures a cell similar, but not identical, to the one used for the half-cells was employed (Figure 4.1); it was still a cell with a fixed-photoelectrode-area, however it was made of two half-cells separated by a H^+-conductive membrane (in all cases a membrane of Nafion-HP was used), in order to prevent the mixing of the evolved hydrogen and oxygen while maintaining the electroneutrality of the system.

Since the two electrodes alone were not able to give rise to a cell potential high enough to catalyse the reaction, it was necessary to employ a reference electrode in order to both check the potentials of anode and cathode, and force the working potential on one of the two electrodes in working conditions; the imposition was always made on the cathode since the sacrificial agents that were employed were intended to aid the oxidation semi-reaction, that would consequently occur at different potentials (of the anode) when the measures were conducted in different electrolytes.

It was verified that by doing so the other electrode reaches the working potential on its own, therefore it was only necessary to artificially provide the potential for one half-cell instead of both.

The same kinds of electrodes were employed along with three different kinds of electrolyte (Table 4.2), in order to compare their performances in different environments.

In particular, the electrolytes were chosen in order to compare the performances of the electrodes: in the absence and in presence of a

Table 4.2. List of the employed electrolytes.

Label	Electrolyte	Description
E-1	Na_2SO_4 solution	$1\,M$ aqueous solution
E-2	Na_2SO_4-glucose solution	aqueous solution, $1\,M$ Na_2SO_4, $0.4\,M$ glucose
E-3	sea water	sample collected from the Adriatic Sea (waters of Giulianova (TE)), on the 9th of august 2022

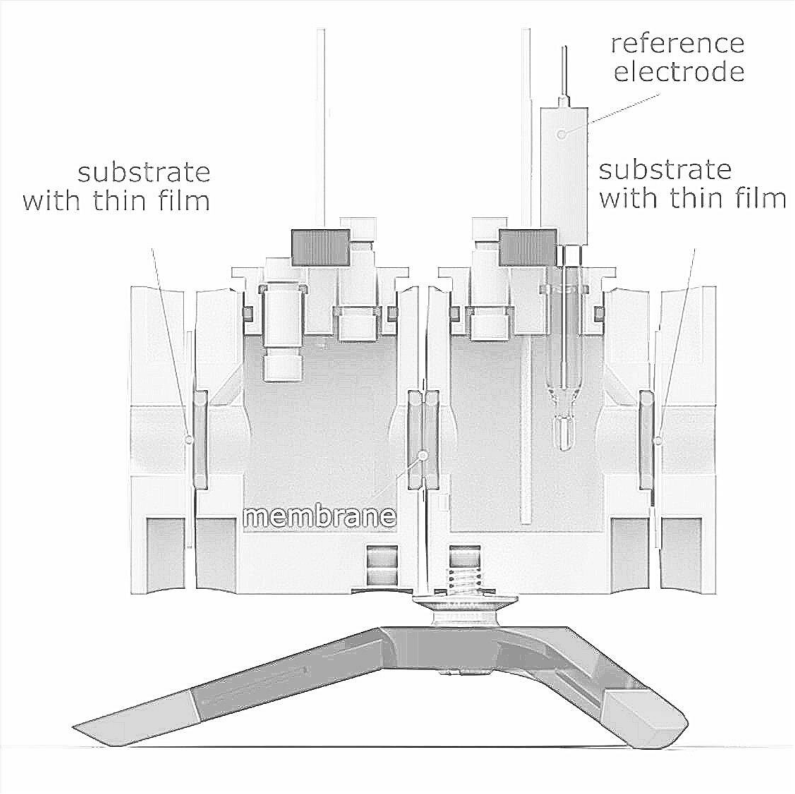

Figure 4.1. Schematic representation of the photo-electrochemical cell employed.

sacrificial agent (both the actual electrolyte and the sacrificial agent are the ones previously employed and already discussed), and in a real matrix.

The effect of the electrolyte became evident in both kinds of measures, as the same anode and cathode gave very different values in the three environments.

From the OCV readings, the values of which are summarized in Table 4.3, it can be seen how the Na_2SO_4 solution allowed the electrodes to develop the higher cell voltage, while with the addition of glucose the final cell voltage was only 2/3 of the previous value.

In this regard, the sea water proved to be no doubt the worst environment as the cell voltage that was reached when it was employed as electrolyte was only 1/3 of the value reached in the Na_2SO_4 solution.

However, the CRA measures showed very different trends. As can be seen form the curves in Figures 4.2-4.4, while the current developed in the Na_2SO_4-glucose solution and in sea water is very similar, the one reached in the Na_2SO_4 solution was $\approx 1/10$ after $6\,h$ of measure and even lower after $12\,h$.

These trends are reflected in the HER values, that were calculated with Equation 3.2, starting from $1000\,s$ up to both $6\,h$ and $12\,h$, and are summarized in Table 4.4. From these values it can be observed how:

E-1: the first cell, with Na_2SO_4 electrolytic solution, gave lower HER values, as could be expected since no sacrificial agent is present to aid the oxidation semi-reaction.

The value calculated after $12\,h$ of measure was slightly lower than the one calculated after $6h$, in accord with the gradual

Table 4.3. OCV values reached by each cell after $1\,h$ of reading in dark and $2\,h$ under illumination.

Label	OCV (mV)
E-1	344
E-2	238
E-3	112

adjustment of the cell and degradation of the electrodes;

E-2: the second cell, with Na_2SO_4-glucose electrolytic solution, gave the highest HER values, as one could suppose due to the presence of a conspicuous quantity of sacrificial agent.

For this cell too, the value calculated after $12\,h$ of measure was lower than the one calculated after $6\,h$, realistically, this decrease was mostly due to the consumption of the glucose, as the difference is much bigger than the one observed for the previous cell, the current curve shows a clear maximum after $\approx 3\,h$ and the measure was performed in a closed system;

E-3: the third cell, with sea water electrolyte, gave intermediate HERs with values much more similar to the ones of the cell containing glucose than to those of the other one.

Contrary to the previous cells, the value calculated after $12\,h$ of measure was slightly higher than the one calculated after $6\,h$, probably due to a gradual adjustment of the cell.

Comparing these results with the ones declared in the literature is not easy, as the performances of the process can be influenced by many factors and there is no standard procedure for the realisation of the measures; however, it can be said that the HERs herein obtained are not far from the ones of other studies, that are summarized in Table 4.5.

Following all these considerations on the experimental measures, the importance of the choice of the electrolyte becomes evident. As such a more complete study would have required the electrochemical characterization of the samples in various different electrolytes, however this was not possible due to the large amount of time that such study would have required.

Table 4.4. HER values of the characterized cells, after $6\,h$ and $12\,h$ of measure.

Label	**Hydrogen Evolution Rate - 6 h ($mol\,h^{-1}\,cm^{-2}$)**	**Hydrogen Evolution Rate - 12 h ($mol\,h^{-1}\,cm^{-2}$)**
E-1	$1.67 \cdot 10^{-6}$	$1.29 \cdot 10^{-6}$
E-2	$12.2 \cdot 10^{-6}$	$11.0 \cdot 10^{-6}$
E-3	$9.15 \cdot 10^{-6}$	$9.99 \cdot 10^{-6}$

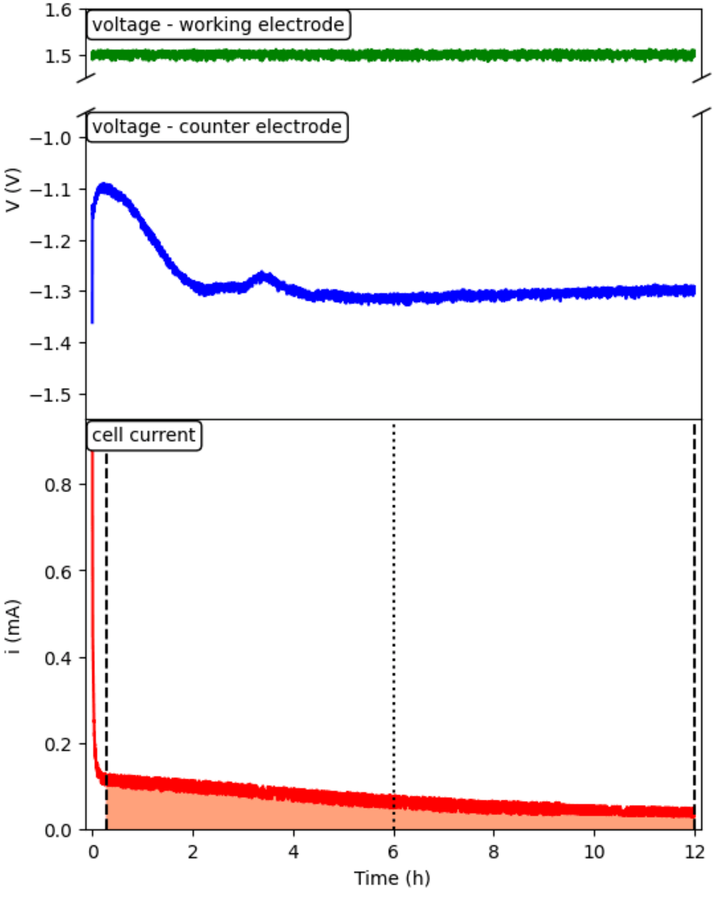

Figure 4.2. CRA measure of the E-1 cell. In the upper graphic, the voltage imposed on the cathode and the voltage assumed by the anode; in the lower graphic, the electric current developed by the cell, the area considered for HER calculation is highlighted.

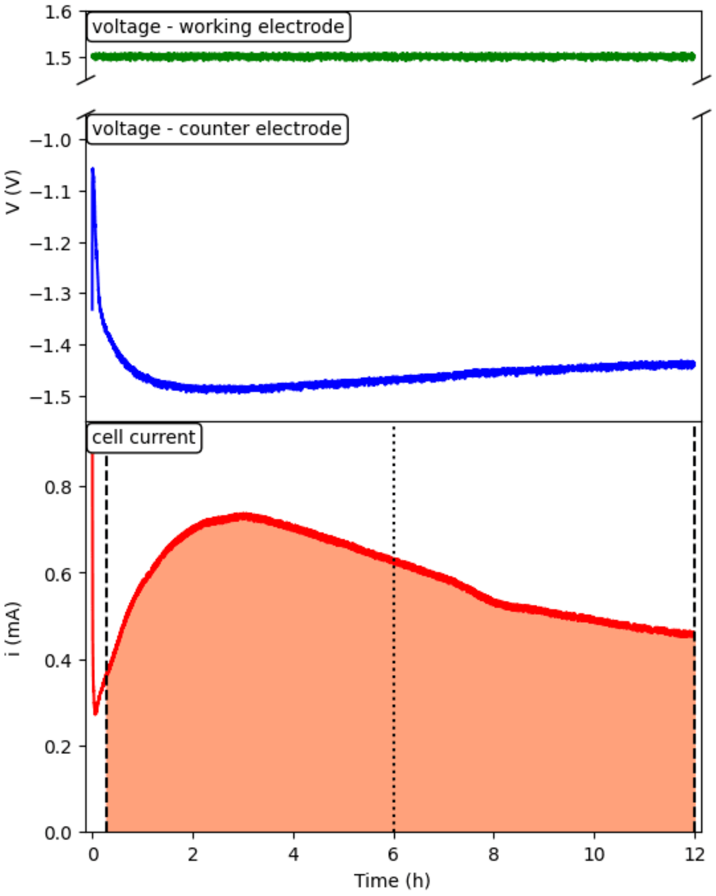

Figure 4.3. CRA measure of the E-2 cell. In the upper graphic, the voltage imposed on the cathode and the voltage assumed by the anode; in the lower graphic, the electric current developed by the cell, the area considered for HER calculation is highlighted.

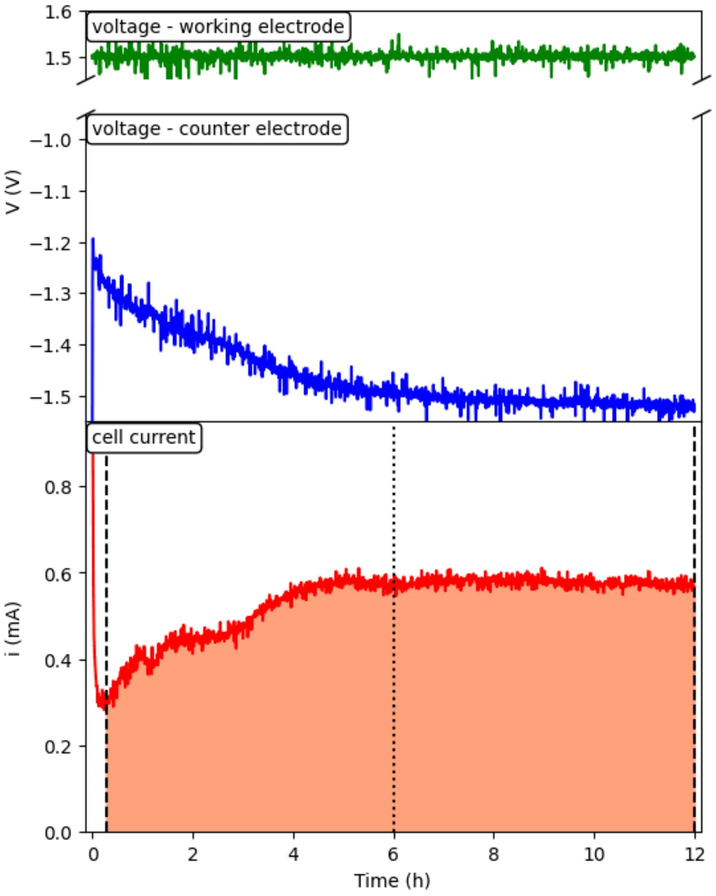

Figure 4.4. CRA measure of the E-3 cell. In the upper graphic, the voltage imposed on the cathode and the voltage assumed by the anode; in the lower graphic, the electric current developed by the cell, the area considered for HER calculation is highlighted.

Table 4.5. Examples of photo-electrochemistry-based electrodes and experimental conditions used for the H_2 production processes. Reprinted with permission from ref.[190] Copyright Chemical Engineering Journal 2021.

Anode	**Cathode**	**Irradiation Source**	**Electrolyte**	**Reactor**	**Reaction Time (h)**	**HER ($\mu mol\, h^{-1}\, cm^{-2}$)**
Pt-deposited-TiO_2 thin film	Pt plate	UV light ($330 - 388\, nm$)	$2.0\, M$ MeOH	pyrex glass reactor	4	11.40
Ag-Ce/TiO_2 NTs	pure graphite	Xe lamp and Hg lamp	10% $\frac{V}{V}$ EtOH/H_2O	quartz photoreactor	6	1.47
graphite/Co-Fe	Pt electrode	visible light ($560\, nm$, $200\, W\, m^{-2}$)	$0.1\, M$ phosphate buffer	three-compartment cell	2	70.90
TiO_2/ stainless stell mesh	Ni/stainless steel	metal-halide lamp with UV filter ($150\, W$)	syntetic oilfield wastewater	PEC filter-press reactor	2	24.72
graphite/N-TiO_2	Pt foil	Xe lamp ($100\, mW\, cm^{-2}$)	$1\, M$ NaOH with 10% wt MeOH	homemade electrolytic cell	4	34.00
NT array WO_3/FeNi	Pt sheet	Xe lamp ($100\, mW\, cm^{-2}$)	$0.5\, M$ KH_2PO_4	single compartment quartz cell	10	3.43

Chapter 5

Future Perspectives

The work that was started during this PhD is still continuing with the exploration of other metal halide perovskites and/or perovskite derivatives as photocatalysts and photo-co-catalysts, also touching the theme of the dimensionality of the co-catalyst, that has not been dealt with up till now.

With this thesis we demonstrated the possibility of exploiting metal halide perovskites and perovskite derivatives as photocatalysts for hydrogen evolution in aqueous environment, without the need of adding a remarkable quantity of halo acids in order to ensure the stability of the material. This result is quite relevant, as it introduces the possibilities given by this class of materials, in particular their versatility and tunability, to the field of aqueous photo- and photo-electro- catalysis.

However, there is still much room for the development of systems such as the ones considered in this PhD, as there are still many issues that need to be solved, such as the chemical and mechanical stability of the materials and of the electrodes, and the necessity to provide an external aid in order to reach the working voltage.

In this context, different kinds of improvement need to be made, as the study of the materials and of the electrolytes can only account for a part of the answer, that needs to be paired with the investigation of the electrodes preparation techniques and with the devising of an optimal geometry for the photo-electrochemical cell.

List of Acronyms

AQY	Apparent Quantum Yield
B.E.T.	Brunauer - Emmett - Teller, adsorption method
CB	Conduction Band
CBM	Conduction Band Minimum
CRA	Chronoamperometric, measures
CV	Cyclic Voltammetry
DFT	Density Functional Theory
DMA	Dimethylammonium
DMF	Dimethylformamide
DOE	Design of Experiments
DW	Deionized Water
EDS	Energy Dispersive X-ray Spectroscopy
FT-IR	Fourier-Transform Infrared spectroscopy
FTO	Fluorine doped Tin Oxide
GC	Gas Chromatography
GC-MS	Gas Chromatography - Mass Spectroscopy
HDA	Hetero Diels-Alder, reaction
HER	Hydrogen Evolution Rate
ICP-OES	Inductively Coupled Plasma - Optical Emission Spectroscopy
LED	Light Emitting Diode

MB	Methylene Blue
MHP	Metal Halide Perovskite
ND	Not Detected
NMR	Nuclear Magnetic Resonance
NT	Nanotube
OCV	Open Circuit Voltage
OER	Oxygen Evolution Rate
PEA	Phenylethylammonium
PEDOT:PSS	Poly(3,4-ethylenedioxythiophene) : Poly-styrenesulfonate
PEI	Poly-ethyleneimine
PL	Photoluminescence
PLQY	Photoluminescence Quantum Yield
RHE	Reversible Hydrogen Electrode
RSD	Relative Standard Deviation
SEM	Scanning Electron Microscopy
TAS	Transient Absorption Spectroscopy
TEM	Transmission Electron Microscopy
TEOA	Triethanolamine
tME	Trimethylethylene
TME	Tetramethylethylene
TON	Turn Over Number
UV-Vis	Ultraviolet - Visible, absorption spectroscopy
VB	Valence Band
VBM	Valence Band Maximum
VPD	Vapor Phase Deposited
XPS	X-ray Photoelectron Spectroscopy
XRD	X-Ray Diffraction

Acknowledgments

This work has been financed by the Research Fund for the Italian Electrical System under the Contract Agreement between RSE S.p.A. and the Ministry of Economic Development - General Directorate for the Electricity Market, Renewable Energy and Energy Efficiency, Nuclear Energy in compliance with the Decree of April 16^{th}, 2018.

I would like to express my appreciation for my supervisors L. Malavasi (from the University of Pavia) and M. Notaro (from RSE S.p.A.) for their help and advice.

I wish to thank M. Corti, A. Girella, B. Mannucci, P. Quadrelli and A. Speltini (from the University of Pavia), F. Ambrosio, F. De Angelis and E. Mosconi (from the CNR Institute of Science and Chemical Technologies "Giulio Natta"), C. N. Dibenedetto, F. Fracassi, A. Listorti and A. Milella (from the University of Bari), and M. Saba and A. Simbula (from the University of Cagliari) for their contribution to the published works that constitute part of this project.
I would also like to thank S. Capelli, V.Gazzillo, E. Malgrati, and M. Radaelli (from RSE S.p.A.), and M. Boiocchi and C. Tedesco (from the University of Pavia) for their contribution to the unpublished work that constitutes all the rest of this thesis.
Finally, I would like to express my gratitude to I. Quinzeni (from RSE S.p.A.) for her assistance in the most significant stages of this project and for her unwavering support.

Bibliography

[1] Sengeni Anantharaj, Sivasankara Rao Ede, Kuppan Sakthikumar, Kannimuthu Karthick, Soumyaranjan Mishra, and Subrata Kundu. Recent trends and perspectives in electrochemical water splitting with an emphasis on sulphide, selenide, and phosphide catalysts of Fe, Co, and Ni: A review. *ACS Catalysis*, 6(12):8069–8097, 2016.

[2] Savio J. A. Moniz, Stephen A. Shevlin, David James Martin, Zheng-Xiao Guo, and Junwang Tang. Visible-light driven heterojunction photocatalysts for water splitting – a critical review. *Energy & Environmental Science*, 8(3):731–759, 2015.

[3] Takashi Hisatomi, Jun Kubota, and Kazunari Domen. Recent advances in semiconductors for photocatalytic and photoelectrochemical water splitting. *Chemical Society Reviews*, 43(22):7520–7535, 2014.

[4] Roland Marschall. Semiconductor composites: Strategies for enhancing charge carrier separation to improve photocatalytic activity. *Advanced Functional Materials*, 24(17):2421–2440, 2014.

[5] Lorna Jeffery Minggu, Wan Ramli Wan Daud, and Mohammad B. Kassin. An overview of photocells and photoreactors for photoelectrochemical water splitting. *International Journal of Hydrogen Energy*, 35(11):5233–5244, 2010.

[6] Kevin Sivula and Roel van de Krol. Semiconducting materials for photoelectrochemical energy conversion. *Nature Reviews Materials*, 1(2):15010, 2016.

[7] Sulagna Patnaik, Satyabadi Martha, and K. M. Parida. An overview of the structural, textural and morphological modulations of g-C_3N_4 towards photocatalytic hydrogen production. *RSC Advances*, 6(52):46929–46951, 2016.

[8] Arne Thomas, Anna Fischer, Frederic Goettmann, Markus Antonietti, Jens-Oliver Müller, Robert Schlögl, and Johan M. Carlsson. Graphitic carbon nitride materials: Variation of structure and morphology and their use as metal-free catalysts. *Journal of Materials Chemistry*, 18(41):4893–4908, 2008.

[9] Jianjun Liu, Bei Cheng, and Jiaguo Yu. A new understanding of the photocatalytic mechanism of the direct z-scheme g-C_3N_4/TiO_2 heterostructure. *Physical Chemistry Chemical Physics*, 18(45):31175–31183, 2016.

[10] George Gibin, Rao Ede Sivasankara, and Luo Zhiping. *Fundamentals of Perovskite Oxides - Synthesis, Structure, Properties and Applications*, chapter Chapter 1: Introduction to Perovskites. CRC Press, Boca Raton, 2020.

[11] Quinten A. Akkerman and Liberato Manna. What defines a halide perovskite? *ACS Energy Letters*, 5(2):604–610, 2020.

[12] Lidia Romani and Lorenzo Malavasi. Solar-driven hydrogen generation by metal halide perovskites: Materials, approaches, and mechanistic view. *ACS Omega*, 5(40):25511–25519, 2020.

[13] Haowei Huang, Bapi Pradhan, Johan Hofkens, Maarten B. J. Roeffaers, and Julian A. Steele. Solar-driven metal halide perovskite photocatalysis: Design, stability, and performance. *ACS Energy Letters*, 5(4):1107–1123, 2020.

[14] Chuang Han, Xiaolin Zhu, Jovan San Martin, Yixiong Lin, Sydney Spears, and Yong Yan. Recent progress in engineering metal halide perovskites for efficient visible-light driven photocatalysis. *ChemSusChem*, 13(16):4005–4025, 2020.

[15] Kim Anh Huynh, Dang Le Tri Nguyen, Van-Huy Nguyen, Dai-Viet N Vo, Quang Thang Trinh, Thang Phan Nguyen, Soo Young Kim, and Quyet Van Le. Halide perovskite photocatalysis: Progress and perspectives. *Journal of Chemical Technology & Biotechnology*, 95(10):2579–2596, 2020.

[16] Bianca-Maria Bresolin, Yuri Park, and Detlef W. Bahnemann. Recent progresses on metal halide perovskite-based material as potential photocatalyst. *Catalysts*, 10(6):709, 2020.

[17] Sunghak Park, Woo Je Chang, Chan Woo Lee, Sangbaek Park, Hyo-Yong Ahn, and Ki Tae Nam. Photocatalytic hydrogen generation from hydriodic acid using methylammonium lead iodide in dynamic equilibrium with aqueous solution. *Nature Energy*, 2(1):16185, 2017.

[18] Yaqiang Wu, Peng Wang, Xianglin Zhu, Qianqian Zhang, Zeyan Wang, Yuanyuan Liu, Guizheng Zou, Ying Dai, Myung-Hwan Whangbo, and Baibiao Huang. Composite of $CH_3NH_3PbI_3$ with reduced graphene oxide as a highly efficient and stable visible-light photocatalyst for hydrogen evolution in aqueous HI solution. *Advanced Materials*, 30(7):1704342, 2018.

[19] Zhijie Zhao, Jiaojiao Wu, Yan-Zhen Zheng, Nan Li, Xitao Li, and Xia Tao. Ni_3C-decorated $MAPbI_3$ as visible-light photocatalyst for H_2 evolution from HI splitting. *ACS Catalysis*, 9(9):8144–8152, 2019.

[20] Dianxing Ju, Xiaopeng Zheng, Jialiang Liu, Yan Chen, Jian Zhang, Bingqiang Cao, Hang Xiao, Omar F. Mohammed, Osman M. Bakr, and Xutang Tao. Reversible band gap narrowing of Sn-based hybrid perovskite single crystal with excellent phase stability. *Angewandte Chemie International Edition*, 57(45):14868–14872, 2018.

[21] Mariia V. Pavliuk, Mohammed Abdellah, and Jacinto Sà. Hydrogen evolution with $CsPbBr_3$ perovskite nanocrystals under visible light in solution. *Materials Today Communications*, 16:90–96, 2018.

[22] Samuel D. Stranks and Henry J. Snaith. Metal-halide perovskites for photovoltaic and light-emitting devices. *Natural Nanotechnologies*, 10(5):391–402, 2015.

[23] Tae Woo Kim and Kyoung-Shin Choi. Nanoporous $BiVO_4$ photoanodes with dual-layer oxygen evolution catalysts for solar water splitting. *Science*, 343(6174):990–994, 2014.

[24] Yuriy Pihosh, Ivan Turkevych, Kazuma Mawatari, Jin Uemura, Yutaka Kazoe, Sonya Kosar, Kikuo Makita, Takeyoshi Sugaya, Takuya Matsui, Daisuke Fujita, Masahiro Tosa, Michio Kondo, and Takehiko Kitamori. Photocatalytic generation of hydrogen by core-shell $WO_3/BiVO_4$ nanorods with ultimate water splitting efficiency. *Scientific Reports*, 5(1):11141, 2015.

[25] Rie Saito, Yugo Miseki, and Kazuhiro Sayama. Highly efficient photoelectrochemical water splitting using a thin film photoanode of $BiVO_4/SnO_2/WO_3$ multi-composite in a carbonate electrolyte. *Chemical Communications*, 48(32):3833–3835, 2012.

[26] Satyananda Kishore Pilli, Thomas E. Furtak, Logan D. Brown, Todd G. Deutsch, John A. Turner, and Andrew M. Herring. Cobalt-phosphate (Co−Pi) catalyst modified Mo-doped $BiVO_4$ photoelectrodes for solar water oxidation. *Energy & Environmental Science*, 4(12):5028–5034, 2011.

[27] Bartek J. Trześniewski and Wilson A. Smith. Photocharged $BiVO_4$ photoanodes for improved solar water splitting. *Journal of Materials Chemistry A*, 4(8):2919–2926, 2016.

[28] Jaesun Song, Jaeseong Cha, Mi Gyoung Lee, Hye Won Jeong, Sehun Seo, Ji Ae Yoo, Taemin Ludvic Kim, Jongmin Lee, Heesung No, Do Hyun Kim, Sang Yun Jeong, Hyunji An, Byoung Hun Lee, Chung Wung Bark, Hyunwoong Park, Ho Won Jang, and Sanghan Lee. Template-engineered epitaxial $BiVO_4$ photoanodes for efficient solar water splitting. *Journal of Materials Chemistry A*, 5(35):18831–18838, 2017.

[29] Abdul Qayum, Mingrui Guo, Jing Wei, Shun Dong, Xiuling Jiao, Dairong Chen, and Ting Wang. An in situ combustion method for scale-up fabrication of $BiVO_4$ photoanodes with enhanced long-term photostability for unassisted solar water splitting. *Journal of Materials Chemistry A*, 8(21):10989–10997, 2020.

[30] Ambra Pisanu, Andrea Speltini, Barbara Vigani, Franca Ferrari, Matteo Mannini, Nicola Calisi, Brunetto Cortigiani, Andrea Caneschi, Paolo Quadrelli, Antonella Profumo, and Lorenzo Malavasi. Enhanced hydrogen photogeneration by bulk g-C_3N_4 through a simple and efficient oxidation route. *Dalton Transactions*, 47(19):6772–6778, 2018.

[31] Michela Sturini, Andrea Speltini, Federica Maraschi, Giulia Vinci, Antonella Profumo, Luca Pretali, Angelo Albini, and Lorenzo Malavasi. g-C_3N_4-promoted degradation of ofloxacin antibiotic in natural waters under simulated sunlight. *Environmental Science and Pollution Research*, 24(4):4153–4161, 2017.

[32] Fan Dong, Yuhan Li, Zhenyu Wang, and Wing-Kei Ho. Enhanced visible light photocatalytic activity and oxidation ability of porous graphene-like g-C_3N_4 nanosheets via thermal exfoliation. *Applied Surface Science*, 358:393–403, 2015.

[33] Ilias Papailias, Nadia Todorova, Tatiana Giannakopoulou, Nikolaos Ioannidis, Nikos Boukos, Chrysoula P. Athanasekou, Dimitra Dimotikali, and Christos Trapalis. Chemical vs thermal exfoliation of g-C_3N_4 for NOx removal under visible light irradiation. *Applied Catalysis B: Environmental*, 239:16–26, 2018.

[34] Menglu Zhang, Yu Yang, Xiaoqiang An, Jingjing Zhao, Yueping Bao, and Li-an Hou. Exfoliation method matters: The microstructure-dependent photoactivity of g-C_3N_4 nanosheets for water purification. *Journal of Hazardous Materials*, 424:127424, 2022.

[35] Lirong Yang, Xiaoyu Liu, Zhigang Liu, Chunmei Wang, Gang Liu, Qinglong Li, and Xiaoxin Feng. Enhanced photocatalytic activity of g-C_3N_4 2 D nanosheets through thermal exfoliation using dicyandiamide as precursor. *Ceramics International*, 44(17):20613–20619, 2018.

[36] Haidong Chen, Feng Zhang, Xianwen Sun, Weifeng Zhang, and Guoqiang Li. Effect of reaction atmosphere on photodeposition of Pt nanoparticles and photocatalytic hydrogen evolution from $SrTiO_3$ suspension system. *International Journal of Hydrogen Energy*, 43(10):5331–5336, 2018.

[37] Lidia Romani, Andrea Speltini, Francesco Ambrosio, Edoardo Mosconi, Antonella Profumo, Marcello Marelli, Serena Margadonna, Antonella Milella, Francesco Fracassi, Andrea Listorti, Filippo De Angelis, and Lorenzo Malavasi. Water-stable $DMASnBr_3$ lead-free perovskite for effective solar-driven photocatalysis. *Angewandte Chemie International Edition*, 60(7):3611–3618, 2021.

[38] Chao Zheng and Oleg Rubel. Unravelling the water degradation mechanism of $CH_3NH_3PbI_3$. *The Journal of Physical Chemistry C*, 123(32):19385–19394, 2019.

[39] Jeffrey A. Christians, Pierre A. Miranda Herrera, and Prashant V. Kamat. Transformation of the excited state and photovoltaic efficiency of $CH_3NH_3PbI_3$ perovskite upon controlled exposure to humidified air. *Journal of the American Chemical Society*, 137(4):1530–1538, 2015.

[40] Mengye Wang, Yunpeng Zuo, Jingli Wang, Yi Wang, Xinpeng Shen, Bocheng Qiu, Lejuan Cai, Feichi Zhou, Shu Ping Lau, and Yang Chai. Remarkably enhanced hydrogen generation of organolead halide perovskites via piezocatalysis and photocatalysis. *Advanced Energy Materials*, 9(37):1901801, 2019.

[41] Zhijie Zhao, Jiaojiao Wu, Yan-Zhen Zheng, Nan Li, Xitao Li, Zhili Ye, Siyu Lu, Xia Tao, and Chuncheng Chen. Stable hybrid perovskite $MAPb(Br_{1-x}I_x)_3$ for photocatalytic hydrogen evolution. *Applied Catalysis B: Environmental*, 253:41–48, 2019.

[42] Xiaolin Zhu, Yixiong Lin, Jovan San Martin, Yue Sun, Dian Zhu, and Yong Yan. Lead halide perovskites for photocatalytic organic synthesis. *Nature Communications*, 10(1):2843, 2019.

[43] Ambra Pisanu, Andrea Speltini, Paolo Quadrelli, Giovanni Drera, Luigi Sangaletti, and Lorenzo Malavasi. Enhanced air-stability of Sn-based hybrid perovskites induced by dimethylammonium (DMA): Synthesis, characterization, aging and hydrogen photogeneration of the $MA_{1-x}DMA_xSnBr_3$ system. *Journal of Material Chemistry C*, 7(23):7020–7026, 2019.

[44] Shaowen Cao, Jingxiang Low, Jiaguo Yu, and Mietek Jaroniec. Polymeric photocatalysts based on graphitic carbon nitride. *Advanced Materials*, 27(13):2150–2176, 2015.

[45] Sheng Ye, Rong Wang, Ming-Zai Wu, and Yu-Peng Yuan. A review on g-C_3N_4 for photocatalytic water splitting and CO_2 reduction. *Applied Surface Science*, 358(1):15–27, 2015.

[46] Zaiwang Zhao, Yanjuan Sun, and Fan Dong. Graphitic carbon nitride based nanocomposites: a review. *Nanoscale*, 7(1):15–37, 2015.

[47] Nur Fajrina and Muhammad Tahir. A critical review in strategies to improve photocatalytic water splitting towards hydrogen production. *International Journal of Hydrogen Energy*, 44(2):540–577, 2019.

[48] G. Thiele and B. R. Serr. Crystal structure of dimethylammonium tribromostannate(II), $(CH_3)_2NH_2SnBr_3$. *Zeitschrift für Kristallographie - Crystalline Materials*, 211(1):47–47, 1996.

[49] Francisco Palazon, Yousra El Ajjouri, Paz Sebastia-Luna, Simone Lauciello, Liberato Manna, and Henk J. Bolink. Mechanochemical synthesis of inorganic halide perovskites: Evolution of phase-purity, morphology, and photoluminescence. *Journal of Materials Chemistry C*, 7(37):11406–11410, 2019.

[50] Lu Hou, Yihua Zhu, Jingrun Zhu, and Chunzhong Li. Tuning optical properties of lead-free 2d tin-based perovskites with carbon chain spacers. *The Journal of Physical Chemistry C*, 123(51):31279–31285, 2019.

[51] G. Beamson and D. Briggs. *High Resolution XPS of Organic Polymers: the Scienta ESCA300 Database*. Wiley, Chichester [England]; New York, 1992.

[52] Zhi-An Lan, Guigang Zhang, and Xinchen Wang. A facile synthesis of Br-modified g-C_3N_4 semiconductors for photoredox water splitting. *Applied Catalysis B: Environmental*, 192:116–125, 2016.

[53] Jianwei Zhou, Mo Zhang, and Yongfa Zhu. Photocatalytic enhancement of hybrid C_3N_4/TiO_2 prepared via ball milling method. *Physical Chemistry Chemical Physics*, 17(5):3647–3652, 2015.

[54] Rongxian Zhang, Xiaogang Lu, Liying Huang, Zhijiang Ke, and Yeping Li. Ball-milling combined calcination synthesis of In_2O_3/C_3N_4 for high photocatalytic activity under visible light irradiation. *Journal of Materials Science: Materials in Electronics*, 28(11):8255–8265, 2017.

[55] Kaixing Zhu, Yang Lv, Jing Liu, Wenjun Wang, Chunping Wang, Songmei Li, Peng Wang, Meng Zhang, Alan Meng, and Zhenjiang Li. Facile fabrication of g-C_3N_4/SnO_2 composites and ball milling treatment for enhanced photocatalytic performance. *Journal of Alloys and Compounds*, 802:13–18, 2019.

[56] Andrea Speltini, Ambra Pisanu, Antonella Profumo, Chiara Milanese, Luigi Sangaletti, Giovanni Drera, Maddalena Patrini, Marzia Pentimalli, and Lorenzo Malavasi. Rationalization of hydrogen production by bulk g-C_3N_4: an in-depth correlation between physico-chemical parameters and solar light photocatalysis. *RSC Advances*, 8(69):39421–39431, 2018.

[57] Francesco Ambrosio, Giacomo Miceli, and Alfredo Pasquarello. Redox levels in aqueous solution: Effect of van der Waals interactions and hybrid functionals. *The Journal of Chemical Physics*, 143(24):244508, 2015.

[58] Francesco Ambrosio, Zhendong Guo, and Alfredo Pasquarello. Absolute energy levels of liquid water. *The Journal of Physical Chemistry Letters*, 9(12):3212–3216, 2018.

[59] Yi Qin Gao, Yuri Georgievskii, and R. A. Marcus. On the theory of electron transfer reactions at semiconductor electrode/liquid interfaces. *The Journal of Chemical Physics*, 112(7):3358–3369, 2000.

[60] Renato N. Sampaio, David C. Grills, Dmitry E. Polyansky, David J. Szalda, and Etsuko Fujita. Unexpected roles of triethanolamine in the photochemical reduction of CO_2 to formate by ruthenium complexes. *Journal of the American Chemical Society*, 142(5):2413–2428, 2020.

[61] Lidia Romani, Anu Bala, Vijay Kumar, Andrea Speltini, Antonella Milella, Francesco Fracassi, Andrea Listorti, Antonella Profumo, and Lorenzo Malavasi. PEA_2SnBr_4: a water-stable lead-free two-dimensional perovskite and demonstration of its use as a co-catalyst in hydrogen photogeneration and organic-dye degradation. *Journal of Materials Chemistry C*, 8(27):9189–9194, 2020.

[62] Peng Gao, Abd Rashid Bin Mohd Yusoff, and Mohammad Khaja Nazeeruddin. Dimensionality engineering of hybrid halide perovskite light absorbers. *Nature Communications*, 9:5028, 2018.

[63] Huifen Xu, Yuhai Sun, Haiying Zheng, Guozhen Liu, Xiaoxiao Xu, Shendong Xu, Liying Zhang, Xiaojing Chen, and Xu Pan. High-performance and moisture-stable perovskite solar cells with

a 2d modified layer via introducing a high dipole moment cation. *Journal of Materials Chemistry C*, 7(48):15276–15284, 2019.

[64] Johannes Schlipf, Yinghong Hu, Shambhavi Pratap, Lorenz Bießmann, Nuri Hohn, Lionel Porcar, Thomas Bein, Pablo Docampo, and Peter Müller-Buschbaum. Shedding light on the moisture stability of 3d/2d hybrid perovskite heterojunction thin films. *ACS Applied Energy Materials*, 2(2):1011–1018, 2019.

[65] Ian C. Smith, Eric T. Hoke, Diego Solis-Ibarra, Michael D. McGehee, and Hemamala I. Karunadasa. A layered hybrid perovskite solar-cell absorber with enhanced moisture stability. *Angewandte Chemie International Edition*, 53(42):11232–11235, 2014.

[66] Yanqiang Hu, Ting Qiu, Fan Bai, Wei Ruan, and Shufang Zhang. Highly efficient and stable solar cells with 2 D $MA_3Bi_2I_9$/3 D $MAPbI_3$ heterostructured perovskites. *Advanced Energy Materials*, 8(19):1703620, 2018.

[67] Alexander Z. Chen, Michelle Shiu, Jennifer H. Ma, Matthew R. Alpert, Depei Zhang, Benjamin J. Foley, Detlef-M. Smilgies, Seung-Hun Lee, and Joshua J. Choi. Origin of vertical orientation in two-dimensional metal halide perovskites and its effect on photovoltaic performance. *Nature Communications*, 9:1336, 2018.

[68] Duyen H. Cao, Constantinos C. Stoumpos, Omar K. Farha, Joseph T. Hupp, and Mercouri G. Kanatzidis. 2d homologous perovskites as light-absorbing materials for solar cell applications. *Journal of the American Chemical Society*, 137(24):7843–7850, 2015.

[69] Hsinhan Tsai, Wanyi Nie, Jean-Christophe Blancon, Constantinos C. Stoumpos, Reza Asadpour, Amanda J. Harutyunyan, Boris nad Neukirch, Rafael Verduzco, Jared J. Crochet, Sergei Tretiak, Laurent Pedesseau, Jacky Even, Muhammad A. Alam, Gautam Gupta, Jun Lou, Pulickel M. Ajayan, Michael J. Bedzyk, Mercouri G. Kanatzidis, and Aditya D. Mohite. High-efficiency two-dimensional Ruddlesden-Popper perovskite solar cells. *Nature*, 536(7616):312–316, 2016.

[70] Li Na Quan, Mingjian Yuan, Riccardo Comin, Oleksandr Voznyy, Eric M. Beauregard, Sjoerd Hoogland, Andrei Buin, Ahmad R.

Kirmani, Kui Zhao, Aram Amassian, Dong Ha Kim, and Edward H. Sargent. Ligand-stabilized reduced-dimensionality perovskites. *Journal of the American Chemical Society*, 138(8):2649–2655, 2016.

[71] Teck Ming Koh, Vignesh Shanmugam, Xintong Guo, Swee Sien Lim, Oliver Filonik, Eva M. Herzig, Peter Müller-Buschbaum, Varghese Swamy, Sum Tze Chien, Subodh G. Mhaisalkar, and Nripan Mathews. Enhancing moisture tolerance in efficient hybrid 3d/2d perovskite photovoltaics. *Journal of Materials Chemistry A*, 6(5):2122–2128, 2018.

[72] Anu Bala and Vijay Kumar. Role of ligand–ligand interactions in the stabilization of thin layers of tin bromide perovskite: An ab initio study of the atomic and electronic structure, and optical properties. *The Journal of Physical Chemistry C*, 123(41):25176–25184, 2019.

[73] Ambra Pisanu, Mauro Coduri, Marta Morana, Yasemin O. Ciftci, Aurora Rizzo, Andrea Listorti, Mattia Gaboardi, Luca Bindi, Valentine I. E. Queloz, Chiara Milanese, Giulia Grancini, and Lorenzo Malavasi. Exploring the role of halide mixing in lead-free BZA_2SnX_4 two dimensional hybrid perovskites. *Journal of Materials Chemistry A*, 8(4):1875–1886, 2020.

[74] Tze-Bin Song, Takamichi Yokoyama, Constantinos C. Stoumpos, Jenna Logsdon, Duyen H. Cao, Michael R. Wasielewski, Shinji Aramaki, and Mercouri G. Kanatzidis. Importance of reducing vapor atmosphere in the fabrication of tin-based perovskite solar cells. *Journal of the American Chemical Society*, 139(2):836–842, 2017.

[75] Guangfu Liao, Yan Gong, Li Zhang, Haiyang Gao, Guan-Jun Yang, and Baizeng Fang. Semiconductor polymeric graphitic carbon nitride photocatalysts: the “holy grail” for the photocatalytic hydrogen evolution reaction under visible light. *Energy & Environmental Science*, 12(7):2080–2147, 2019.

[76] Francis Opoku, Krishna Kuben Govender, Cornelia Gertina Catharina Elizabeth van Sittert, and Penny Poomani Govender. Insights into the photocatalytic mechanism of mediator-free direct

z-scheme g-C_3N_4/Bi_2MoO_6 (010) and g-C_3N_4/Bi_2WO_6 (010) heterostructures: A hybrid density functional theory study. *Applied Surface Science*, 427:487–498, 2018.

[77] Dalal K. Kanan and Emily A. Carter. Band gap engineering of MnO via ZnO alloying: A potential new visible-light photocatalyst. *The Journal of Physical Chemistry C*, 116(18):9876–9887, 2012.

[78] Bog G. Kim, J. Y. Jo, and Cheong S. W. Hybrid functional calculation of electronic and phonon structure of $BaSnO_3$. *Journal of Solid State Chemistry*, 197:134–138, 2013.

[79] Andrea Speltini, Lidia Romani, Daniele Dondi, Lorenzo Malavasi, and Antonella Profumo. Carbon nitride-perovskite composites: Evaluation and optimization of photocatalytic hydrogen evolution in saccharides aqueous solution. *Catalysts*, 10(11):1259, 2020.

[80] Marco Corti, Rossella Chiara, Lidia Romani, Barbara Mannucci, Lorenzo Malavasi, and Paolo Quadrelli. g-C_3N_4/metal halide perovskite composites as photocatalysts for singlet oxygen generation processes for the preparation of various oxidized synthons. *Catalysis Science & Technology*, 11(6):2292–2298, 2021.

[81] Jiuqing Wen, Jun Xie, Xiaobo Chen, and Xin Li. A review on g-C_3N_4-based photocatalysts. *Applied Surface Science*, 391:72–123, 2017.

[82] Muhammad Salman Nasir, Guorui Yang, Iqra Ayub, Silan Wang, Ling Wang, Xiaojun Wang, Wei Yan, Shengjie Peng, and Seeram Ramakarishna. Recent development in graphitic carbon nitride based photocatalysis for hydrogen generation. *Applied Catalysis B: Environmental*, 257:117855, 2019.

[83] Su Shiung Lam, Van-Huy Nguyen, Minh Tuan Nguyen Dinh, Dinh Quang Khieu, Duc Duong La, Huu Trung Nguyen, Dai Viet N. Vo, Changlei Xia, Rajender S. Varma, Mohammadreza Shokouhimehr, Chinh Chien Nguyen, Quyet Van Le, and Wanxi Peng. Mainstream avenues for boosting graphitic carbon nitride efficiency: Towards enhanced solar light-driven photocatalytic hydrogen production and environmental remediation. *Journal of Materials Chemistry A*, 8(21):10571–10603, 2020.

[84] Andrea Speltini, Andrea Scalabrini, Federica Maraschi, Michela Sturini, Ambra Pisanu, Lorenzo Malavasi, and Antonella Profumo. Improved photocatalytic H_2 production assisted by aqueous glucose biomass by oxidized g-C_3N_4. *International Journal of Hydrogen Energy*, 43(32):14925–14933, 2018.

[85] Andrea Speltini, Francesca Gualco, Federica Maraschi, Michela Sturini, Daniele Dondi, Lorenzo Malavasi, and Antonella Profumo. Photocatalytic hydrogen evolution assisted by aqueous (waste)biomass under simulated solar light: Oxidized g-C_3N_4 vs. P_{25} titanium dioxide. *International Journal of Hydrogen Energy*, 44(8):4072–4078, 2019.

[86] Lilei Zhang, Jingxiao Zhang, Yuanyu Xia, Menghan Xun, Hong Chen, Xianghui Liu, and Xia Yin. Metal-free carbon quantum dots implant graphitic carbon nitride: Enhanced photocatalytic dye wastewater purification with simultaneous hydrogen production. *International Journal of Molecular Sciences*, 21(3):1052, 2020.

[87] Ying-Chih Pu, Hsiao-Chuan Fan, Tzu-Wei Liu, and Jie-Wen Chen. Methylamine lead bromide perovskite/protonated graphitic carbon nitride nanocomposites: Interfacial charge carrier dynamics and photocatalysis. *Journal of Materials Chemistry A*, 5(48):25438–25449, 2017.

[88] Zhen Li, Shengfan Wu, Jie Zhang, Yufei Yuan, Zilong Wang, and Zonglong Zhu. Improving photovoltaic performance using perovskite/surface-modified graphitic carbon nitride heterojunction. *Solar RRL*, 4(3):1900413, 2020.

[89] Dennis Y. C. Leung, Xianliang Fu, Cuifang Wang, Meng Ni, Michael K. H. Leung, Xuxu Wang, and Xianzhi Fu. Hydrogen production over titania-based photocatalysts. *ChemSusChem*, 3(6):681–694, 2010.

[90] Cláudia G. Silva, Maria J. Sampaio, Rita R. N. Marques, Liliana A. Ferreira, Pedro B. Tavares, Adrián M. T. Silva, and Joaquim L. Faria. Photocatalytic production of hydrogen from methanol and saccharides using carbon nanotube-TiO_2 catalysts. *Applied Catalysis B: Environmental*, 178:82–90, 2015.

[91] Xianliang Fu, Jinlin Long, Xuxu Wang, Dennis Y. C. Leung, Zhengxin Ding, Ling Wu, Zizhong Zhang, Zhaohui Li, and Xianzhi Fu. Photocatalytic reforming of biomass: A systematic study of hydrogen evolution from glucose solution. *International Journal of Hydrogen Energy*, 33(22):6484–6491, 2008.

[92] Horst Kisch. On the problem of comparing rates or apparent quantum yields in heterogeneous photocatalysis. *Angewandte Chemie International Edition*, 49(50):9588–9589, 2010.

[93] Andrea Speltini, Michela Sturini, Federica Maraschi, Daniele Dondi, Andrea Serra, Antonella Profumo, Armando Buttafava, and Angelo Albini. Swine sewage as sacrificial biomass for photocatalytic hydrogen gas production: Explorative study. *International Journal of Hydrogen Energy*, 39(22):11433–11440, 2014.

[94] Andrea Speltini, Michela Sturini, Federica Maraschi, Daniele Dondi, Gabriele Fisogni, Enrico Annovazzi, Antonella Profumo, and Armando Buttafava. Evaluation of UV−A and solar light photocatalytic hydrogen gas evolution from olive mill wastewater. *International Journal of Hydrogen Energy*, 40(12):4303–4310, 2015.

[95] Michal Baranowski and Paulina Plochocka. Excitons in metal-halide perovskites. *Advanced Energy Materials*, 10(26):1903659, 2020.

[96] Michael Bowker. Photocatalytic hydrogen production and oxygenate photoreforming. *Catalysis Letters*, 142(8):923–929, 2012.

[97] Jian-Hua Zhang, Mei-Juan Wei, Zhang-Wen Wei, Mei Pan, and Cheng-Yong Su. Ultrathin graphitic carbon nitride nanosheets for photocatalytic hydrogen evolution. *ACS Applied Nano Materials*, 3(2):1010–1018, 2020.

[98] Julia Kennedy, Hasliza Bahruji, Michael Bowker, Philip R. Davies, Emir Bouleghlimat, and Sudarat Issarapanacheewin. Hydrogen generation by photocatalytic reforming of potential biofuels: Polyols, cyclic alcohols, and saccharides. *Journal of Photochemistry and Photobiology A: Chemistry*, 356:451–456, 2018.

[99] Xiongzhen Jiang, Maykel Manawan, Ting Feng, Ruifeng Qian, Ting Zhao, Guanda Zhou, Fantai Kong, Qing Wang, Songyuan Dai, and Jia Hong Pan. Anatase and rutile in Evonik Aeroxide P_{25}: Heterojunctioned or individual nanoparticles? *Catalysis Today*, 300:12–17, 2018.

[100] Li Kunlan, Xia Lixin, Li Jun, Pang Jun, Cao Guoying, and Xi Zuwei. Salt-assisted acid hydrolysis of starch to D-glucose under microwave irradiation. *Carbohydrate Research*, 331(1):9–12, 2001.

[101] Danli Wang, Furong Hou, Xiaobin Ma, Weijun Chen, Lufeng Yan, Tian Ding, Xingqian Ye, and Donghong Liu. Study on the mechanism of ultrasound-accelerated enzymatic hydrolysis of starch: Analysis of ultrasound effect on different objects. *International Journal of Biological Macromolecules*, 148:493–500, 2020.

[102] A. A. Frimer. *Singlet O_2. Volume I: Physical-Chemical Aspects.* CRC Press, Boca Raton, FL, United States, 1985.

[103] R. W. Denny and A. Nickon. *Sensitized Photooxygenation of Olefins*, chapter 2, pages 133–336. John Wiley & Sons, Ltd, 2011.

[104] Christopher S. Foote, Joan Selverstone Valentine, Arthur Greenberg, and Joel F. Liebman. *Active Oxygen in Chemistry.* Springer Dordrecht, Dordrecht, Netherlands, 1995.

[105] Peter R. Ogilby. Singlet oxygen: There is indeed something new under the sun. *Chemical Society Reviews*, 39(8):3181–3209, 2010.

[106] Waldemar Adam, Sara G. Bosio, and Nicholas J. Turro. Highly diasteroselective dioxetane formation in the photooxigenation of enacarbamates with an oxazolidinone chiral auxiliary: Steric control in the $[2 + 2]$ cycloaddition of singlet oxygen through conformational alignment. *Journal of the American Chemical Society*, 124(30):8814–8815, 2002.

[107] Edward L. Clennan and Andrea Pace. Advances in singlet oxygen chemistry. *Tetrahedron*, 61(28):6665–6691, 2005.

[108] Mariza N. Alberti and Michael Orfanopulos. Unravelling the mechanism of the singlet oxygen ene reaction: Recent computational and experimental approaches. *Chemistry – A European Journal*, 16(31):9414–9421, 2010.

[109] Juliana M. de Souza, Timothy J. Brocksom, D.Tyler McQuade, and Kleber T. de Oliveira. Continuous endoperoxidation of conjugated dienes and subsequent rearrangements leading to C−H oxidized synthons. *The Journal of Organic Chemistry*, 83(15):7574–7585, 2018.

[110] Petr Klán and Jakob Wirz. *Photochemistry of Organic Compounds: From Concepts to Practice.* John Wiley & Sons, 2009.

[111] Raymond Bonnett. Photosensitizers of the porphyrin and phthalocyanine series for photodynamic therapy. *Chemical Society Reviews*, 24(1):19–33, 1995.

[112] Víctor Martínez-Agramunt and Eduardo Peris. Photocatalytic properties of a palladium metallosquare with encapsulated fullerenes via singlet oxygen generation. *Inorganic Chemistry*, 58(17):11836–11842, 2019.

[113] Matthias Klaper and Torsten Linker. Intramolecular transfer of singlet oxygen. *Journal of the American Chemical Society*, 137(43):13744–13747, 2015.

[114] Lingqiao Wu, Zahra Abada, Darren S. Lee, Martyn Poliakoff, and Michael W. George. Combining engineering and chemistry for the selective continuous production of four different oxygenated compounds by photo-oxidation of cyclopentadiene using liquid and supercritical CO_2 as solvents. *Tetrahedron*, 74(25):3107–3112, 2018.

[115] Shekhar Putta, Annem Mallikarjun Reddy, Gurrala Sheelu, B.V. Subba Reddy, and Thenkrishnan Kumaraguru. Preparation of $(1\,R,{}_4S)$-4-hydroxycyclopent-2-en-1-yl acetate via Novozym−435 ® catalyzed desymmetrization of cis-3,5-diacetoxy-1-cyclopentene. *Tetrahedron*, 74(46):6673–6679, 2018.

[116] Irene Camussi, Barbara Mannucci, Andrea Speltini, Antonella Profumo, Chiara Milanese, Lorenzo Malavasi, and Paolo

Quadrelli. g-C_3N_4 - singlet oxygen made easy for organic synthesis: Scope and limitations. *ACS Sustainable Chemistry & Engineering*, 7(9):8176–8182, 2019.

[117] Zhuyuan Wang, Xuehua Hong, Shenfei Zong, Changquan Tang, Yiping Cui, and Qingdong Zheng. BODIPY-doped silica nanoparticles with reduced dye leakage and enhanced singlet oxygen generation. *Scientific Reports*, 5:12602, 2015.

[118] Kripal S. Lakhi, Dae-Hwan Park, Khalid Al-Bahily, Wangsoo Cha, Balasubramanian Viswanathan, Jin-Ho Choy, and Ajayan Vinu. Mesoporous carbon nitrides: Synthesis, functionalization, and applications. *Chemical Society Reviews*, 46(1):72–101, 2017.

[119] H. Koch, J. Pirsch, and Anna Benedikt. Notiz zur darstellung von cyclopenten-3,4- und-3,5-diol. *Monatshefte für Chemie und verwandte Teile anderer Wissenschaften*, 94(6):1093–1097, 1963.

[120] Chih-Cheng Chang, Jyh-Fu Lee, and Soofin" Cheng. Highly catalytically active micro/meso-porous Ti−MCM−36 prepared by a grafting method. *Journal of Materials Chemistry A*, 5(30):15676–15687, 2017.

[121] Concepción Álvarez, Rafael Peláez, and Manuel Medarde. New dicyclopentadiene-based scaffolds. *Tetrahedron*, 63(10):2132–2141, 2007.

[122] D. Schnurpfeil. Dicyclopentadienoxidation. i, unkatalysierte flüssigphasenoxidation von dicyclopentadien. *Journal für Praktische Chemie*, 325(3):481–488, 1983.

[123] Shiro Terashima, Shun-ichi Yamada, and Munehiko Nara. Novel use of meso-compound for the preparation of optically active compounds: Synthesis of optically active prostaglandin intermediates from cis-2-cyclopentene-1,4-diol. *Tetrahedron Letters*, 18(11):1001–1004, 1977.

[124] Jie Zhu, Antonius J. H. Klunder, and Binne Zwanenburg. A facile approach to norbornene-annulated cyclopentenones, a novel class of tricyclodecadienones. *Tetrahedron*, 51(17):5117–5132, 1995.

[125] Paul P. M. A. Dols, Esther G. Arnouts, Johannes Rohaan, Antonius J. H. Klunder, and Binne Zwanenburg. Nucleophilic additions to tricyclodecadienone epoxides. the Payne rearrangement of α,β-epoxycyclopentanols contained in a rigid tricyclic system. *Tetrahedron*, 50(11):3473–3490, 1994.

[126] Jean-Baptiste Wiel and Francis Rouessac. A new approach to the synthesis of the prostanoids. *Journal of the Chemical Society, Chemical Communications*, pages 446b–447, 1976.

[127] Hugo Ingelbrecht, Arun Kumar, Ramakrishnan Menon, Pradeep Nadkarni, and Rupesh Pawar. Method of making carbonyl compounds. United States Patent and Trademark Office, 2007. U.S. patent no. US 2007/0049767 A1.

[128] Muniyandi Sankaralingam, Yong-Min Lee, Wonwoo Nam, and Shunichi Fukuzumi. Selective oxygenation of cyclohexene by dioxygen via an iron(V)-oxo complex-autocatalyzed reaction. *Inorganic Chemistry*, 56(9):5096–5104, 2017.

[129] A. A. Ponaras and Omer Zaim. Synthetic elaboration of diosphenols. replacement of hydroxyl by halogen. *The Journal of Organic Chemistry*, 51(24):4741–4743, 1986.

[130] Jingxun Yu, Yu Zhou, Zhenyang Lin, and Rongbiao Tong. Regioselective and stereospecific copper-catalyzed deoxygenation of epoxides to alkenes. *Organic Letters*, 18(18):4734–4737, 2016.

[131] Srinivasa Rao Amanchi, Alexander M. Khenkin, Yael Diskin-Posner, and Ronny Neumann. Bismuth-substituted “sandwich” type polyoxometalate catalyst for activation of peroxide: Umpolung of the peroxo intermediate and change of chemoselectivity. *ACS Catalysis*, 5(6):3336–3341, 2015.

[132] Jisheng Zhang, Wen-Jie Wei, Xiaoyan Lu, Hang Yang, Zhuqi Chen, Rong-Zhen Liao, and Guochuan Yin. Nonredox metal ions promoted olefin epoxidation by iron(II) complexes with H_2O_2: DFT calculations reveal multiple channels for oxygen transfer. *Inorganic Chemistry*, 56(24):15138–15149, 2017.

[133] Haydar Göksu, Diğdem Dalmizrak, Serdar Akbayrak, Mehmet Serdar Gültekin, Saim Özkar, and Önder Metin.

One-pot synthesis of 1,2/3-triols from the allylic hydroperoxides catalyzed by zeolite-confined osmium(0) nanoclusters. *Journal of Molecular Catalysis A: Chemical*, 378:142–147, 2013.

[134] Timothy W. Collette, Susan D. Richardson, and Alfred D. Thruston. Identification of bromohydrins in ozonated waters. *Applied Spectroscopy*, 48(10):1181–1192, 1994.

[135] Bo You, Siyang Li, Narcisse T. Tsona, Jianlong Li, Li Xu, Zhaomin Yang, Shumin Cheng, Qingcai Chen, Christian George, Maofa Ge, and Lin Du. Environmental processing of short-chain fatty alcohols induced by photosensitized chemistry of brown carbons. *ACS Earth and Space Chemistry*, 4(4):631–640, 2020.

[136] Dabo Jiang, Wenwei Hu, Mengke Chen, Zaihui Fu, Anqun Su, Bo Yang, Feng Mao, Chao Zhang, Yachun Liu, and Dulin Yin. Visible-light-triggered quantitative oxidation of 9,10-dihydroanthracene to anthraquinone by o2 under mild conditions. *ChemSusChem*, 13(7):1785–1792, 2020.

[137] Keshav Raghuvanshi, Cheng Zhu, Mahdi Ramezani, Stefano Menegatti, Erik E. Santiso, Dawn Mason, Jody Rodgers, Mesfin E. Janka, and Milad Abolhasani. Highly efficient 1-octene hydroformylation at low syngas pressure: From single-droplet screening to continuous flow synthesis. *ACS Catalysis*, 10(14):7535–7542, 2020.

[138] Abudureheman Wusiman and Chong-Dao Lu. Selective oxidation of benzylic, allylic and propargylic alcohols using dirhodium(II) tetraamidinate as catalyst and aqueous tert-butyl hydroperoxide as oxidant. *Applied Organometallic Chemistry*, 29(4):254–258, 2015.

[139] Minsoo Ju, Weiyang Guan, Jennifer M. Schomaker, and Kaid C. Harper. Sequential reduction of nitroalkanes mediated by CS_2 and amidine/guanidine bases: A controllable Nef reaction. *Organic Letters*, 21(22):8893–8898, 2019.

[140] Marie-Christine Lacasse, Cyril Poulard, and André B. Charette. Iodomethylzinc phosphates: Powerful reagents for the cyclopropanation of alkenes. *Journal of the American Chemical Society*, 127(36):12440–12441, 2005.

[141] Maurício S. Baptista, Jean Cadet, Paolo Di Mascio, Ashwini A. Ghogare, Alexander Greer, Michael R. Hamblin, Carolina Lorente, Silvia Cristina Nunez, Martha Simões Ribeiro, Andrés H. Thomas, Mariana Vignoni, and Tania Mateus Yoshimura. Type I and type II photosensitized oxidation reactions: Guidelines and mechanistic pathways. *Photochemistry and Photobiology*, 93(4):912–919, 2017.

[142] Paul A. Burns and Christopher S. Foote. Chemistry of singlet oxygen. XIX. dioxetanes from indene derivatives. *Journal of the American Chemical Society*, 96(13):4339–4340, 1974.

[143] Paul A. Burns, Christopher S. Foote, and S. Mazur. Chemistry of singlet oxygen. XXIII. low temperature photooxygenation of indenes in aprotic solvent. *The Journal of Organic Chemistry*, 41(6):899–907, 1976.

[144] N. Roy Easton, F. A. L. Anet, P. A. Burns, and C. S. Foote. Carbon-13 nuclear magnetic resonance studies on polyepoxides derived from singlet oxygen addition to indenes. *Journal of the American Chemical Society*, 96(12):3945–3948, 1974.

[145] Lidia Romani, Andrea Speltini, Carlo Nazareno Dibenedetto, Andrea Listorti, Francesco Ambrosio, Edoardo Mosconi, Angelica Simbula, Michele Saba, Antonella Profumo, Paolo Quadrelli, Filippo De Angelis, and Lorenzo Malavasi. Experimental strategy and mechanistic view to boost the photocatalytic activity of $Cs_3Bi_2Br_9$ lead-free perovskite derivative by g-C_3N_4 composite engineering. *Advanced Functional Materials*, 31(46):2104428, 2021.

[146] Xingtao Wang, Taiyang Zhang, Yongbing Lou, and Yixin Zhao. All-inorganic lead-free perovskites for optoelectronic applications. *Materials Chemistry Frontiers*, 3:365–375, 2019.

[147] Yanxiu Li, Xiaoyu Zhang, He Huang, Stephen V. Kershaw, and Andrey L. Rogach. Advances in metal halide perovskite nanocrystals: Synthetic strategies, growth mechanisms, and optoelectronic applications. *Materials Today*, 32:204–221, 2020.

[148] Yongping Fu, Haiming Zhu, Jie Chen, Matthew P. Hautzinger, X.-Y. Zhu, and Song Jin. Metal halide perovskite nanostructures for

optoelectronic applications and the study of physical properties. *Nature Reviews Materials*, 4(3):169–188, 2019.

[149] Vincenza Armenise, Silvia Colella, Francesco Fracassi, and Andrea Listorti. Lead-free metal halide perovskites for hydrogen evolution from aqueous solutions. *Nanomaterials*, 11(2):433, 2021.

[150] Zhixin Jin, Zheng Zhang, Jingwei Xiu, Haisheng Song, Teresa Gatti, and Zhubing He. A critical review on bismuth and antimony halide based perovskites and their derivatives for photovoltaic applications: Recent advances and challenges. *Journal of Materials Chemistry A*, 8(32):16166–16188, 2020.

[151] Bianca-Maria Bresolin, Carsten Günnemann, Detlef W. Bahnemann, and Mika Sillanpää. Pb-free $Cs_3Bi_2I_9$ perovskite as a visible-light-active photocatalyst for organic pollutant degradation. *Nanomaterials*, 10:763, 2020.

[152] Bianca-Maria Bresolin, Paolo Sgarbossa, Detlef W. Bahnemann, and Mika Sillanpää. $Cs_3Bi_2I_9$/g-C_3N_4 as a new binary photocatalyst for efficient visible-light photocatalytic processes. *Separation and Purification Technology*, 251:117320, 2020.

[153] Bianca-Maria Bresolin, Narmina O. Balayeva, Luis I. Granone, Ralf Dillert, Detlef W. Bahnemann, and Mika Sillanpää. Anchoring lead-free halide $Cs_3Bi_2I_9$ perovskite on UV100–TiO_2 for enhanced photocatalytic performance. *Solar Energy Materials and Solar Cells*, 204:110214, 2020.

[154] Sumit S. Bhosale, Aparna K. Kharade, Efat Jokar, Amir Fathi, Sue-min Chang, and Eric Wei-Guang Diau. Mechanism of photocatalytic CO_2 reduction by bismuth-based perovskite nanocrystals at the gas–solid interface. *Journal of the American Chemical Society*, 141(51):20434–20442, 2019.

[155] Yitao Dai and Harun Tüysüz. Lead-free $Cs_3Bi_2Br_9$ perovskite as photocatalyst for ring-opening reactions of epoxides. *ChemSusChem*, 12(12):2587–2592, 2019.

[156] Yitao Dai, Corentin Poidevin, Cristina Ochoa-Hernández, Alexander A. Auer, and Harun Tüysüz. A supported bismuth halide perovskite photocatalyst for selective aliphatic and aromatic c–h

bond activation. *Angewandte Chemie International Edition*, 59(14):5788–5796, 2020.

[157] Ruolin Cheng, Handong Jin, Maarten B. J. Roeffaers, Johan Hofkens, and Elke Debroye. Incorporation of caesium lead halide perovskites into g-C_3N_4 for photocatalytic CO_2 reduction. *ACS Omega*, 5(38):24495–24503, 2020.

[158] Menglong Zhang, Weizhe Wang, Fangliang Gao, and Dongxiang Luo. g-C_3N_4-stabilised organic–inorganic halide perovskites for efficient photocatalytic selective oxidation of benzyl alcohol. *Catalysts*, 11(4):505, 2021.

[159] F. Lazarini. Caesium enneabromodibismuthate(III). *Acta Crystallographica Section B*, 33(9):2961–2964, 1977.

[160] Kelsey K. Bass, Laura Estergreen, Christopher N. Savory, John Buckeridge, David O. Scanlon, Peter I. Djurovich, Stephen E. Bradforth, Mark E. Thompson, and Brent C. Melot. Vibronic structure in room temperature photoluminescence of the halide perovskite $Cs_3Bi_2Br_9$. *Inorganic Chemistry*, 56(1):42–45, 2017.

[161] Kyle M. McCall, Constantinos C. Stoumpos, Svetlana S. Kostina, Mercouri G. Kanatzidis, and Bruce W. Wessels. Strong electron–phonon coupling and self-trapped excitons in the defect halide perovskites $A_3M_2I_9$ (A = Cs, Rb; M = Bi, Sb). *Chemistry of Materials*, 29(9):4129–4145, 2017.

[162] Kelin He, Jun Xie, Zhao-Qing Liu, Neng Li, Xiaobo Chen, Jun Hu, and Xin Li. Multi-functional Ni_3C cocatalyst/g-C_3N_4 nanoheterojunctions for robust photocatalytic H_2 evolution under visible light. *Journal of Materials Chemistry A*, 6(27):13110–13122, 2018.

[163] Aditya Sharma, Mayora Varshney, Keun Hwa Chae, and Sung Ok Won. Mechanistic investigations on emission characteristics from g-C_3N_4, g-C_3N_4@Pt and g-C_3N_4@Ag nanostructures using x-ray absorption spectroscopy. *Current Applied Physics*, 18(11):1458–1464, 2018.

[164] Yanwen Yuan, Lulu Zhang, Jun Xing, M. Iqbal Bakti Utama, Xin Lu, Kezhao Du, Yongmei Li, Xiao Hu, Shijie Wang, Aziz Genç, Rafal Dunin-Borkowski, Jordi Arbiol, and Qihua Xiong.

High-yield synthesis and optical properties of g-C_3N_4. *Nanoscale*, 7(29):12343–12350, 2015.

[165] Robert Godin, Yiou Wang, Martijn A. Zwijnenburg, Junwang Tang, and James R. Durrant. Time-resolved spectroscopic investigation of charge trapping in carbon nitrides photocatalysts for hydrogen generation. *Journal of the American Chemical Society*, 139(14):5216–5224, 2017.

[166] Hatice Kasap, Christine A. Caputo, Benjamin C. M. Martindale, Robert Godin, Vincent Wing-hei Lau, Bettina V. Lotsch, James R. Durrant, and Erwin Reisner. Solar-driven reduction of aqueous protons coupled to selective alcohol oxidation with a carbon nitride–molecular Ni catalyst system. *Journal of the American Chemical Society*, 138(29):9183–9192, 2016.

[167] Huiyu Zhang, Yaping Chen, Rong Lu, Ruiyu Li, and Anchi Yu. Charge carrier kinetics of carbon nitride colloid: a femtosecond transient absorption spectroscopy study. *Physical Chemistry Chemical Physics*, 18(22):14904–14910, 2016.

[168] Chen Ye, Jia-Xin Li, Zhi-Jun Li, Xu-Bing Li, Xiang-Bing Fan, Li-Ping Zhang, Bin Chen, Chen-Ho Tung, and Li-Zhu Wu. Enhanced driving force and charge separation efficiency of protonated g-C_3N_4 for photocatalytic O_2 evolution. *ACS Catalysis*, 5(11):6973–6979, 2015.

[169] Wenxing Yang, Robert Godin, Hatice Kasap, Benjamin Moss, Yifan Dong, Sam A. J. Hillman, Ludmilla Steier, Erwin Reisner, and James R. Durrant. Electron accumulation induces efficiency bottleneck for hydrogen production in carbon nitride photocatalysts. *Journal of the American Chemical Society*, 141(28):11219–11229, 2019.

[170] Jiajun Luo, Xiaoming Wang, Shunran Li, Jing Liu, Yueming Guo, Guangda Niu, Li Yao, Yuhao Fu, Liang Gao, Qingshun Dong, Chunyi Zhao, Meiying Leng, Fusheng Ma, Wenxi Liang, Liduo Wang, Shengye Jin, Junbo Han, Lijun Zhang, Joanne Etheridge, Jianbo Wang, Yanfa Yan, Edward H. Sargent, and Jiang Tang. Efficient and stable emission of warm-white light from lead-free halide double perovskites. *Nature*, 563(7732):541–545, 2018.

[171] Zhendong Guo, Francesco Ambrosio, Wei Chen, Patrick Gono, and Alfredo Pasquarello. Alignment of redox levels at semiconductor–water interfaces. *Chemistry of Materials*, 30(1):94–111, 2018.

[172] Julia Wiktor, Igor Reshetnyak, Francesco Ambrosio, and Alfredo Pasquarello. Comprehensive modelling of the band gap and absorption spectrum of $BiVO_4$. *Physical Reviews Materials*, 1(2):022401, 2017.

[173] Julia Wiktor, Francesco Ambrosio, and Alfredo Pasquarello. Role of polarons in water splitting: The case of $BiVO_4$. *ACS Energy Letters*, 3(7):1693–1697, 2018.

[174] David B. Mitzi, Konstantinos Chondroudis, and Cherie R. Kagan. Design, structure, and optical properties of organic-inorganic perovskites containing an oligothiophene chromophore. *Inorganic Chemistry*, 38(26):6246–6256, 1999.

[175] Ziyong Cheng and Jun Lin. Layered organic–inorganic hybrid perovskites: Structure, optical properties, film preparation, patterning and templating engineering. *CrystEngComm*, 12(10):2646–2662, 2010.

[176] Cunming Liu, Yingqi Wang, Huifang Geng, Taishan Zhu, Elif Ertekin, David Gosztola, Sizhuo Yang, Jier Huang, Bin Yang, Keli Han, Sophie E. Canton, Qingyu Kong, Kaibo Zheng, and Xiaoyi Zhang. Asynchronous photoexcited electronic and structural relaxation in lead-free perovskites. *Journal of the American Chemical Society*, 141(33):13074–13080, 2019.

[177] A.I. Popov, E.A. Kotomin, and J. Maier. Analysis of self-trapped hole mobility in alkali halides and metal halides. *Solid State Ionics*, 302:3–6, 2017.

[178] Filippo De Angelis. Direct vs. indirect injection mechanisms in perylene dye-sensitized solar cells: A DFT/TDDFT investigation. *Chemical Physics Letters*, 493(4):323–327, 2010.

[179] Friedrich W. K uster and Alfred Thiel. *Tabelle per le Analisi Chimiche e Chimico-Fisiche* - 14^a *edizione.* Hoepli, via Hoepli 5, 20121, Milano (Italy), 1999.

[180] Hansel Comas Rojas, Sebastiano Bellani, Francesco Fumagalli, Gabriele Tullii, Silvia Leonardi, Matthew T. Mayer, Marcel Schreier, Michael Gr atzel, Guglielmo Lanzani, Fabio Di Fonzo, and Maria Rosa Antognazza. Polymer-based photocathodes with a solution-processable cuprous iodide anode layer and a polyethyleneimine protective coating. *Energy & Environmental Science*, 9(12):3710–3723, 2016.

[181] Changchao Jia, Lijun Yang, Yizhu Zhang, Xia Zhang, Kai Xiao, Jingsan Xu, and Jian Liu. Graphitic carbon nitride films: Emerging paradigm for versatile applications. *ACS Applied Materials & Interfaces*, 12(48):53571–53591, 2020.

[182] Liqun Wang, Yueyu Tong, Jianmin Feng, Jungang Hou, Jing Li, Xinggang Hou, and Ji Liang. g-C_3N_4-based films: a rising star for photoelectrochemical water splitting. *Sustainable Materials and Technologies*, 19:e00089, 2019.

[183] Peipei Liu, Xiaohe Huo, Yunfei Tang, Jun Xu, Xiaoqiang Liu, and Danny K.Y. Wong. A TiO_2 nanosheet-g-C_3N_4 composite photoelectrochemical enzyme biosensor excitable by visible irradiation. *Analytica Chimica Acta*, 984:86–95, 2017.

[184] Xuefei Wang, Jingjing Cheng, Huogen Yu, and Jiaguo Yu. A facile hydrothermal synthesis of carbon dots modified g-C_3N_4 for enhanced photocatalytic H_2-evolution performance. *Dalton Transactions*, 46(19):6417–6424, 2017.

[185] Fangke Yu, Yi Wang, Hongrui Ma, and Guohui Dong. Enhancing the yield of hydrogen peroxide and phenol degradation via a synergistic effect of photoelectrocatalysis using a g-C_3N_4/ACF electrode. *International Journal of Hydrogen Energy*, 43(42):19500–19509, 2018.

[186] Jiewei Liu, Sandeep Pathak, Thomas Stergiopoulos, Tomas Leijtens, Konrad Wojciechowski, Stefan Schumann, Nina Kausch-Busies, and Henry J. Snaith. Employing PEDOT as the p-type charge collection layer in regular organic–inorganic perovskite solar cells. *The Journal of Physical Chemistry Letters*, 6(9):1666–1673, 2015.

[187] Dilpreet Singh Mann, You-Hyun Seo, Sung-Nam Kwon, and Seok-In Na. Efficient and stable planar perovskite solar cells with a PEDOT:PSS/SrGO hole interfacial layer. *Journal of Alloys and Compounds*, 812:152091, 2020.

[188] Jinzhi Niu, Dong Yang, Xiaodong Ren, Zhou Yang, Yucheng Liu, Xuejie Zhu, Wangen Zhao, and Shengzhong (Frank) Liu. Graphene-oxide doped PEDOT:PSS as a superior hole transport material for high-efficiency perovskite solar cell. *Organic Electronics*, 48:165–171, 2017.

[189] Marianna Bellardita, Elisa Isabel García-López, Giuseppe Marcì, Giorgio Nasillo, and Leonardo Palmisano. Photocatalytic solar light H_2 production by aqueous glucose reforming. *European Journal of Inorganic Chemistry*, 2018(41):4522–4532, 2018.

[190] Himadri Rajput, Eilhann E. Kwon, Sherif A. Younis, Seunghyun Weon, Tae Hwa Jeon, Wonyong Choi, and Ki-Hyun Kim. Photoelectrocatalysis as a high-efficiency platform for pulping wastewater treatment and energy production. *Chemical Engineering Journal*, 412:128612, 2021.